

Generation of Quasi-Monoenergetic Proton Beams from High Intensity Laser Plasmas

- A step towards application -



Diplomarbeit

Friedrich-Schiller-Universität Jena
Physikalisch-Astronomische Fakultät

eingereicht von Sebastian Pfoth
geboren am 03.02.1980 in Jena

Gutachter:

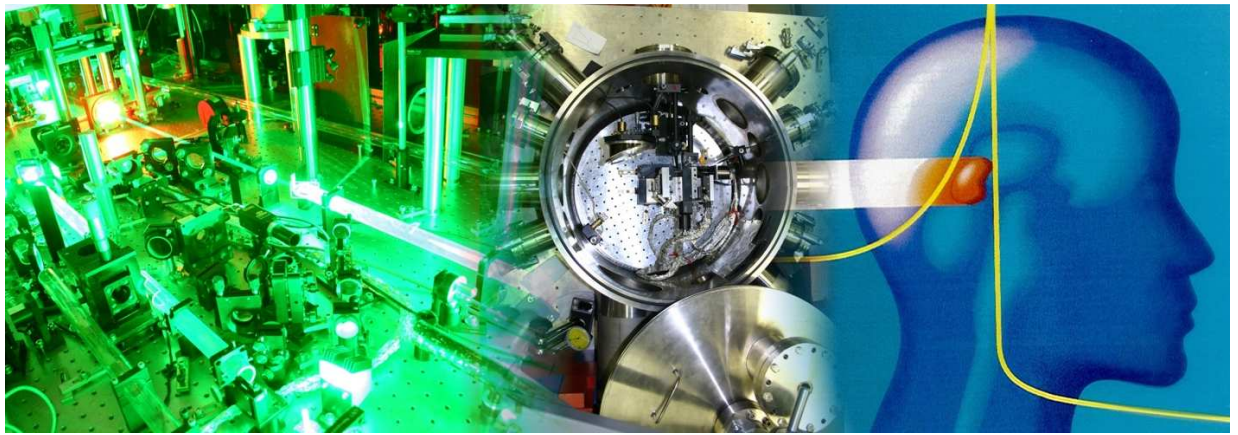
1. *Prof. Dr. Roland Sauerbrey*
Institut für Optik und Quantenelektronik
Friedrich-Schiller-Universität Jena
2. *Prof. Ken W.D. Ledingham*
Department of Physics
University of Strathclyde Glasgow

Tag der Verleihung des Diploms:

Contents

1	Introduction	6
2	Theory	8
2.1	Electron acceleration	8
2.1.1	Plasma formation, Resonance Absorption, classical electron motion & plasma waves	8
2.1.2	”Direct” acceleration mechanisms: relativistic $\vec{v} \times \vec{B}$ -heating, ponderomotive force & Brunel absorption	12
2.1.3	”Indirect” acceleration mechanisms: plasma waves & wake field	15
2.2	Ion acceleration	17
2.2.1	Front side acceleration	17
2.2.2	Rear side acceleration: Target Normal Sheath Acceleration & Debye Sheath	18
2.2.3	Features of Target Normal Sheath Acceleration	22
2.2.4	Monoenergetic proton beams from a spatially confined source	27
3	Experiment	33
3.1	Setup	33
3.1.1	Laser	33
3.1.2	Target chamber	35
3.1.3	Production of microstructured targets	37
3.1.4	Alignment of the target	39
3.1.5	Reduction of parasitic protons	45
3.1.6	Particle beam analysis I: dispersion via Thomson Parabola	46
3.1.7	Particle beam analysis II: detection	49
3.2	Analysis Techniques	53
3.2.1	Binning	53
3.2.2	Calibration of the MCP against CR39	55
3.3	Results	56

3.3.1	Overview over previous results from conventional targets & determination of the optimum experimental conditions	56
3.3.2	Monoenergetic proton beams	58
3.3.3	CR39 comparative shots	63
3.3.4	2D Particle-In-Cell simulation	64
4	Outlook	67
4.1	Petawatt scaling: prospects of the POLARIS laser class	67
4.2	A promising application	69
4.2.1	Stopping of fast ions in matter	69
4.2.2	Medical proton therapy	72
5	Conclusion	76
6	Acknowledgements	81
	Bibliography	83



1 Introduction

When moving up in light intensity, one will be naturally interested in the particular, possibly new effects of that light on matter. The development of high intensity lasers is hence very closely connected to the examination of light-matter interactions and the transfer of the additional energy onto particles. Unfortunately, a typical experimental situation does not expose singular phenomena, but instead offers a blurred overlap of various effects and timescales. By extracting the conditions of energy deposition carefully, high intensity laser physics has revealed both extreme cases of “classical” acceleration mechanisms as well as fundamentally new regimes of particle acceleration, which stimulated the idea of laser-driven particle sources.

In fact, high intensity lasers have ventured widely into the domain of particle physics throughout the last years. Current table-top laser systems readily generate X-rays, relativistic electrons and energetic ion beams by the interaction of ultrastrong, ultrashort light pulses with matter [1–3]. The rapidly evolving popularity of the field has repeatedly provoked speculations about the possible implications and applications of laser particle acceleration. Proposed schemes for the future include very ambitious plans like fast ignition via inertial confinement fusion [4], but also more pragmatic ideas like particle injectors for conventional accelerators [5] or commercial particle sources for medical purposes, e.g. radio-isotope production [6] or medical proton therapy [7, 8].

None of the above examples is more than a promising prospect yet: The proposed confinement fusion requires an intense, quasi-monoenergetic proton beam for the penetration of a pellet target. Also, the use of laser plasma sources as injectors presupposes proton beams with limited bandwidth and emittance in order to match the injected bunch with the subsequent conventional accelerator. And medical proton therapy especially - as one of the most auspicious applications - depends crucially on the availability of monenergetic spectra with variable peak energy and spread.

The criterion of monochromacy is indeed central for most applications. Hitherto laser-produced ion beams all suffered from a broad, Boltzmann-like energy spectrum. In this thesis, the first production of quasi-monoenergetic protons from laser plasmas is presented. These beams were achieved by the interaction of high intensity laser pulses with thin foil targets using a novel target geometry: structured targets allow to shape the resulting proton spectrum by manipulating the proton source, which proves to be a highly reproducible phenomenon. In experiments carried out at the Jena 15TW Titan:Sapphire laser (JETI), dozens of proton spectra were recorded with peak features around 1.3MeV and a reduced energy spread of

25 – 50%. The present thesis will give an introduction to this novel acceleration technique, its physical background as well as its possible implications.

Consequently, the thesis claim derives as follows:

Table-top laser systems can reliably produce quasi-monoenergetic proton beams, which resembles a very principle step towards application. Promising technologies like laser-based proton therapy thus become conceivable on a 10-year timescale.

The thesis will pursue this claim in three steps:

Theory: When a high intensity laser pulse hits a solid target, a hot electron plasma is formed. From this plasma, electrons will be accelerated either directly by the laser field, or indirectly with the help of so-called plasma waves. The expelled electrons induce huge electric fields, in which the target ions can then be accelerated. Thereby, Target Normal Sheath Acceleration (TNSA) has been identified as the central mechanism in charge. Although the sum of processes takes place within a few cubic microns and picoseconds only, it will be necessary to consider an entire chain of events in order to understand laser ion acceleration. With this understanding, an altered TNSA scheme shall finally be presented, which delivers the basis for the generation of monoenergetic proton beams.

Experiment and Results: This part will set out from a description of the JETI laser system, which shall be done by simply following the laser light from its origin to the target chamber. A few sections will be spent specifically on various aspects concerning the target, including the process of target fabrication and positioning within the chamber. The work will then turn to the methods of particle detection and also discuss binning and calibration issues. Finally, the first quasi-monoenergetic spectra from laser accelerated protons shall be presented. The spectra will be interpreted and compared to those from conventional targets. A 2D Particle-In-Cell (PIC) simulation supports the presented results.

Outlook: The achievements of this work will be extrapolated to the next laser generation, which allows the positioning of the results with respect to future applications. Considerations about the stopping of ions in matter will lead to an estimation about the chances for medical use of laser generated protons.

The importance of monoenergetic proton beams has been recently acknowledged by a publication in *Nature* magazine [9]. In conjunction with the lately reported monoenergetic electrons [10–12] and Carbon ions [13], this shows that laser accelerators are in fact capable of producing high-quality particle beams. The present thesis wants to contribute to such a consolidated understanding of laser plasmas as potent and competitive particle sources.

2 Theory

2.1 Electron acceleration

2.1.1 Plasma formation, Resonance Absorption, classical electron motion & plasma waves

Summary: The rising edge of an intense laser pulse suffices to create a hot electron plasma on the target, with which the main part of the pulse then interacts. The electron density determines the optical properties of the plasma. Under the influence of an external laser field, the electrons oscillate and form plasma waves. The laser can excite the plasma resonantly at the critical electron density.

When atoms are exposed to the focus of an ultraintense laser pulse, they will be immediately subject to ionization. The released electrons will form a *hot electron plasma*, whereas the term “hot” refers to a temperature that can be assigned to the electron ensemble via

$$n_{\text{el}} \sim e^{\frac{E_{\text{kin}}}{k_{\text{B}}T}}. \quad (2.1)$$

For relativistic electron ensembles with MeV energy, the temperature T exceeds 10^{11}K . Since the intensity profile of a real laser pulse is typically a Gaussian, the ionization process happens in different stages [14]. *Ionization* occurs for intensities greater than 10^{12}W/cm^2 ; first by multi-photon absorption processes, later directly via field ionization. In the second case, the strong laser field will superpose the trapping coulomb potential of the nuclei and lower it periodically in accordance with the light’s oscillation frequency. If the potential barrier is decreased sufficiently, the electrons can tunnel through the remaining wall with a certain probability (tunnel ionization). For even higher intensities, the laser field will force the potential below the atomic energy levels and thus set free the electrons immediately (over-the-barrier ionization). Once there are free electrons, the ionization process is furthermore supported by collision ionization, that is the inter-electronic transfer of momentum.

The laser intensities applied in this work are of the order of several 10^{19}W/cm^2 and hence the rising edge of the incident pulse will suffice to generate a plasma already. The main, intense part of the pulse will thus interact with a pre-ionized region - the so-called *preplasma*. Since the light electrons will follow an external electromagnetic field much faster than the inert ions, the obtained plasma can basically be treated as a free electron plasma, which can

in a first approximation be described by a mixture of two simple models: the Drude model of conductivity and the Lorentz model of the atom.¹

The *Drude model of conductivity* treats metals as a cloud of free electrons moving in front of a positively charged, immobile and uniform background of ions [15]. All interactions except for collisions are neglected, which allows for a description of the electron cloud with a kind of kinetic gas theory. If this electron gas is subject to an external electric field \vec{E} , the resulting current densities can be derived from Ohm's law:

$$\vec{j}_{\text{DC}} = \frac{n_e e^2 \tau}{m_0} \vec{E} = \sigma_0 \vec{E} \quad (2.2)$$

$$\vec{j}_{\text{AC}}(\omega) = \frac{\sigma_0}{1 - i\omega\tau} \vec{E}(\omega) = \sigma(\omega) \vec{E}(\omega) \quad (2.3)$$

for the DC and AC case, respectively [15]. Here, σ_0 and σ are the DC and AC conductivities, n_e is the free electron density, e and m_0 are the electron charge and rest mass and τ a phenomenological damping constant, which corresponds to an inverse collision frequency $\omega_{\text{col}} = 2\pi/\tau$. For an periodic external field - historically an AC-voltage, but in our case a propagating laser field - the free electrons perform collective oscillations in front of the fixed ionic background. With the above $\vec{j}_{\text{AC}}(\omega)$, one finds the wave equation for the electron motion from the Maxwell equations in matter

$$\nabla^2 \vec{E} - \frac{\varepsilon(\omega)}{c^2} \frac{\partial^2}{\partial t^2} \vec{E} = 0, \quad (2.4)$$

c being the speed of light. The dielectric function

$$\varepsilon(\omega) = 1 + \frac{i\sigma(\omega)}{\varepsilon_0\omega} \quad (2.5)$$

covers the full material response and assumes for high frequencies ($\omega \gg \omega_{\text{col}}$) the simple form

$$\varepsilon(\omega) = 1 - \frac{n_e e^2}{\varepsilon_0 m_0 \omega^2} = 1 - \frac{\omega_p^2}{\omega^2}, \quad (2.6)$$

where the convenient *plasma frequency* was introduced as

$$\omega_p^2 = \frac{n_e e^2}{\varepsilon_0 m_0}. \quad (2.7)$$

The plasma frequency is an eigen-frequency of the electron motion and depends on the electron density only. In principle, any displacement of plasma electrons by the laser field corresponds to the stimulation of a plasma oscillation according to the electron density at this point.

¹Plasmas are usually treated either as a particle ensemble or a continuous fluid, each of which bears advantages and disadvantages. For the current purpose the treatment as a free electron cloud with homogeneous background is sufficient.

However, the energy transfer will work best when $\omega_p = \omega_{\text{laser}}$, where the process is then called *Resonance Absorption* [16].

The collective displacement of the electrons from the ions creates periodic regions of charge accumulation and deprivation. This charge density modulation follows the propagation of the pulse front with a phase velocity close to the speed of light and leaves behind a *plasma wave* [16–18]. With the Drude model, one has thus obtained a picture of the collective kinematic behaviour of free electrons under the impact of an external field.

The theory of the Lorentz, on the contrary, describes the motion of a single trapped electron in the harmonic potential of a atomic nucleus [19]. Again under the influence of an external periodic field, one obtains the equation of motion

$$\vec{r}'' + 2\beta\vec{r}' + \omega_0^2\vec{r} = \frac{e}{m_0}\vec{E}_0e^{-i\omega t} \quad (2.8)$$

with the solution

$$\vec{r}(\omega, t) = \frac{\frac{e}{m_0}\vec{E}_0}{\omega^2 - \omega_0^2 + 2i\beta\omega}e^{-i\omega t}. \quad (2.9)$$

Here, β and ω_0 are the damping and the restoring constants of the oscillating system. From the integration over all dipole moments $\vec{p}(\omega, t) = e\vec{r}(\omega, t)$, one obtains the complex dielectric function $\varepsilon(\omega)$, which covers the complete material response. The real and the imaginary part of the dielectric function render two different interaction regimes between the light field and the electrons, namely dispersion and absorption, which is articulated by the two (classical) quantities of the refractive index $n_r(\omega)$ and the absorption coefficient $\alpha(\omega)$ [20],

$$n_r(\omega) \approx \sqrt{\text{Re}\{\varepsilon(\omega)\}}, \quad (2.10)$$

$$\alpha(\omega) \approx \frac{\omega}{c} \cdot \frac{\text{Im}\{\varepsilon(\omega)\}}{\sqrt{\text{Re}\{\varepsilon(\omega)\}}}. \quad (2.11)$$

For a single bound electron oscillating in the electric field, one finds the explicit expression for the refractive index

$$n_r(\omega) = \sqrt{1 - \frac{n_e e^2}{\varepsilon_0 m} \cdot \frac{\omega^2 - \omega_0^2}{(\omega^2 - \omega_0^2)^2 + \beta^2 \omega^2}}. \quad (2.12)$$

Now, if one wants to apply the Lorentz model to the free electron case, one can simply set the restoring constant ω_0 zero (i.e. the electrons are not bound to any nucleus), which was originally done for the description of the optical properties of metals [20]. The damping constant β , which can again be understood as a inverse collision frequency between the free electrons, is much smaller than the light oscillation frequency and can hence be neglected. Merging now the Lorentz with the Drude model from above, one can assign the plasma frequency to the

refractive index and obtains the simple relation

$$n_r(\omega) = \sqrt{1 - \frac{\omega_p^2}{\omega^2}}. \quad (2.13)$$

The plasma frequency hence marks a delineation between a real and an imaginary refractive index, that is a transparent and a non-transparent regime for wave propagation in a plasma. The optical properties of a free electron plasma are thus determined by a sole parameter, the plasma frequency, which in turn is an expression for the electron density. Recollecting the connection between the refractive index and the dielectric function (eq. 2.10), one can employ the wave equation (2.4) in order to obtain a dispersion relation for the plasma:

$$\omega^2 = \omega_p^2 + k^2 c^2. \quad (2.14)$$

For the concrete scenario of a laser pulse hitting a solid target, the dependency of the wave propagation on the electron density can be put in a slightly different way: The thermal expansion of the plasma from the irradiated surface results in a certain (exponential) electron density profile. As the pulse penetrates the plasma, it will eventually encounter an electron density where $\omega = \omega_p$. At this density, the pulse will be reflected (eq. 2.13). In other words, for each frequency ω one can define a *critical electron density* $n_c(\omega) = \omega^2 \epsilon_0 m_0 / e^2$, which distinguishes between transparent and non-transparent plasma regions for the respective laser frequency. These regions are commonly referred to as the *underdense* vs. the *overdense plasma* regime. The refractive index then becomes

$$n_r(\omega) = \sqrt{1 - \frac{n_e}{n_c}}. \quad (2.15)$$

For a laser wavelength of about 800 nm, the critical density amounts to $n_c = 1.75 \times 10^{21} \text{ cm}^{-3}$.

It shall be noted that if the incidence direction deviates from the density gradient direction, the maximum penetration depth is reduced to an electron density characterized by the refractive index n_{reff} , where the pulse turns smoothly (Fig. 2.1) [14, 21]. However this implies that, if the laser pulse does not pass (or even reach) the critical density at all, no resonant excitation of the plasma will occur ($\omega \neq \omega_p$). But the phenomenon can be saved: for non-normal pulse incidence, the electric field will reach into the “forbidden” area evanescently. According to the distance between n_{reff} and n_c , a fraction of the laser light will tunnel through the remaining gap and still excite the plasma wave resonantly.² The counteracting aims of keeping the tunnelling distance sufficiently small on the one hand, and enforcing a longitudinal field component on the other hand, determine the applied angle of incidence, which proves to

²This argumentation holds true for a p-polarized pulse; for s-polarization, no longitudinal field component will appear anyway.

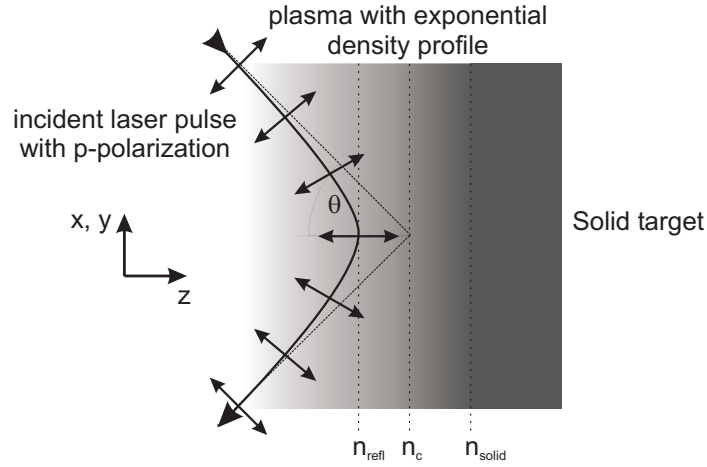


Figure 2.1: Laser pulse entering a given (pre-)plasma profile.

attain its optimum at about 45° .³

2.1.2 "Direct" acceleration mechanisms: relativistic $\vec{v} \times \vec{B}$ -heating, ponderomotive force & Brunel absorption

Summary: The magnetic part of the Lorentz force allows a relativistic electron to gain momentum in forward direction. For the intensity profile of a real laser pulse, the ponderomotive force accelerates the electrons along the E -field gradient. The JETI pulses create a ponderomotive potential of $\Phi_{\text{pond}} = 1.7 \text{ MeV}$ for $a_0 = 4.3$. Electrons accelerated into the target are screened off from the laser field immediately and retain momentum.

In the previous section, the motion of electrons under the impact of an external electromagnetic wave has been discussed. Thereby, it has been neglected that - besides the electric field - such a wave also possesses a magnetic field. This approximation is valid for low electron velocities only. The motion of a free charged particle within an electromagnetic field is generally given by the Lorentz force

$$\vec{F}_L = m_0 \ddot{\vec{r}} = q \left(\vec{E} + \vec{v} \times \vec{B} \right). \quad (2.16)$$

Since the magnitudes of the electric and the magnetic field are related as $|\vec{B}| = \frac{1}{c} |\vec{E}|$, their relative contributions amount to

$$\ddot{\vec{r}} = \frac{q}{m_0} E \left(\vec{e}_x + \frac{v}{c} (\vec{e}_v \times \vec{e}_y) \right). \quad (2.17)$$

Here, z is the propagation axis of the linearly polarized laser wave, whereas x and y denote

³Strictly speaking, the increase of the focal size due to oblique incidence has to be considered here, too.

the E - and B -field direction, respectively. Equation (2.17) shows that for an electron initially at rest ($v_0 = 0$), the motion will at the beginning determined by the E -field. As the electron gains momentum in x -direction, the B -field will in addition accelerate the electron in z -direction because of $(\vec{e}_x \times \vec{e}_y) = \vec{e}_z$. This B -field contribution is, however, only significant for $v \approx c$ - that is, if the E -field suffices to induce a relativistic electron quiver motion in the first place.

For the considered experiments, this is indeed the case. The applied intensities of several $10^{19}\text{W}/\text{cm}^2$ correspond to periodic fields of the order of $E = 10^{13}\text{V}/\text{m}$, which leads to electron velocities close to the speed of light and demands a strictly relativistic treatment. The magnetic part must thus not be neglected! In a fully relativistic treatment, the equations of motion

$$\vec{F}_L = \frac{d}{dt} (\gamma m_0 \dot{\vec{r}}) = q (\vec{E} + \vec{v} \times \vec{B}), \quad (2.18)$$

become coupled and can be solved with [22]

$$x = a_0 \frac{c}{\omega} (\cos\phi - 1) \sim a_0 \quad (2.19)$$

$$z = \frac{1}{4} a_0^2 \frac{c}{\omega} \left(\phi - \frac{1}{2} \sin 2\phi \right) \sim a_0^2, \quad (2.20)$$

where $\phi = (\omega t - kz)$. The factor a_0 is called the *relativistic parameter* and given by [23]

$$a_0 = \frac{Ee}{\omega m_0 c} \approx \sqrt{\frac{I \lambda^2}{1.4 \times 10^{18} \frac{\text{W}}{\text{cm}^2} \cdot \mu\text{m}^2}}. \quad (2.21)$$

The experimental conditions of this thesis, $I = 4 \times 10^{19}\text{W}/\text{cm}^2$ and $\lambda = 800\text{nm}$, are hence described by $a_0 = 4.3$.⁴

The z -term of the electron motion shows two distinct contributions: the first one gives a net drift in laser direction; the second one describes an oscillation with twice the laser frequency, $\omega_z = 2\omega$. That is, during a full E -field oscillation (x -direction), the electron simultaneously performs two oscillations along the laser axis (z -direction), which is basically due to the alternating constellation of the \vec{E} -, \vec{v} - and \vec{B} -vector triplet. The overlapping oscillations constitute a so-called *figure-8 motion*. Because of the net drift in z -direction, however, this figure-8 motion is only observable in a frame co-moving with the average electron velocity.

The drift term in the z -motion represents a first possibility for the electron to gain net momentum in forward direction - a first "real" acceleration mechanism. The oscillations alone would leave the electron at its very initial position after a full cycle. The forward push becomes

⁴Acknowledging that $\frac{Ee}{\omega m_0} = v_{\text{osc}}^{\text{class}}$, the classical oscillation velocity in the E -field, one can equally write $a_0 = v_{\text{osc}}^{\text{class}}/c$. The relativistic parameter gives a measure for the "relativisticness" of the situation, where the threshold for relativistic interaction is commonly defined as $a_0 = 1$, i.e. when the classical oscillation velocity approaches the speed of light.

dominant for high velocities, which can be seen from a calculation of the ultra-relativistic limit [22], where $v_x(a_0 \rightarrow \infty) = 0$ and $v_z(a_0 \rightarrow \infty) = c$.

The relativistic impact of the magnetic field is commonly named (*relativistic*) $\vec{v} \times \vec{B}$ -heating [16] and shows that for high intensities the electron behaviour is completely different from the classical case. When now considering the shape of a real laser pulse, the analysis becomes somewhat more complicated. Since the electromagnetic wave can no longer be assumed infinite, the electron will come to rest at the end of the pulse again. That is, although the electron shows a net forward displacement, it does not gain any net energy from the z -drift [24]. Moreover, when recalling the transverse Gaussian profile of the pulse, any displacement of the electron along the E -field axis equals a displacement into a region of lower intensity. There, it will experience a reduced restoring force, which prevents it from returning to the laser axis. The electron will thus receive a net transverse momentum.

This effect has been named *ponderomotive scattering* [24, 25]. In many cases, the electron will indeed leave the scope of the laser pulse before its end or even within the first cycle, whereupon it remains with a fraction of the hitherto obtained forward momentum. A single relativistic electron initially at rest can at most gain the kinetic energy

$$E_{\text{kin}}^{\text{max}} = \frac{1}{2} m_0 c^2 a_0^2, \quad (2.22)$$

directly from the laser field [23, 26], which follows from $E_{\text{kin}} = (\gamma - 1)m_0 c^2$ and the relation between energy and momentum, $E^2 = (\gamma m_0 c^2)^2 = E_0^2 + p^2 c^2$, where p can be taken to be p_z ($p_z \gg p_x$ for $a_0 \gg 1$) and attains $p \approx p_z = -\frac{1}{2} a_0^2 \sin^2 \Phi$ [22]. For $a_0 = 4.3$, the maximum kinetic energy is hence limited to 4.7 MeV. In a later section, however, the reader will encounter acceleration mechanisms that exceed the direct laser acceleration by far.

The employment of the relativistic equations of motion is a rather laborious undertaking and can be handled satisfactory by computer simulations only. If one is, however, not interested in the specific trajectories of the electrons but in their maximum energy gain only, one can choose a more macroscopic formalism. The equations of motion 2.18 can be solved by first order perturbation theory, that is, by expanding the laser field into a static term plus a linear term, $E(\vec{r}) \approx E(\vec{r}_0) + \nabla E(\vec{r}_0) \circ (\vec{r} - \vec{r}_0)$. After averaging over the fast oscillations, one then obtains the so-called *ponderomotive force* [16, 27]

$$\vec{F}_{\text{pond}} = -\frac{e^2}{4 \langle \gamma \rangle_\tau m_0 \omega^2} \nabla E^2 \quad (2.23)$$

as the driving force for a single electron, where $\langle \gamma \rangle_\tau$ is the cycle-averaged relativistic correction. In a first approximation, the impact of the laser pulse on an electron can hence be described by the gradient of the electric field squared. The resulting ‘‘pushing-away’’ of the electrons at the steep pulse front has occasionally evoked the picture of a snow plough and is comparable to a radiation pressure. In correspondence to the ponderomotive force, a *ponderomotive potential*

can be derived [16, 24, 28],

$$\Phi_{\text{pond}} = \frac{e^2}{4 \langle \gamma \rangle_{\tau} m_0 \omega^2} E^2 \quad (2.24)$$

$$\approx m_0 c^2 (\gamma - 1) = m_0 c^2 \left(\sqrt{1 + a_0^2} - 1 \right) \quad (2.25)$$

which amounts to $\Phi_{\text{pond}} = 1.7 \text{ MeV}$ for a a_0 of 4.3 as given above.

Another direct acceleration effect shall be described briefly. The *Brunel absorption*, or “not-so-resonant absorption” [29], becomes significant for very short pulses, that is, a very steep intensity gradient. In such a case, almost no plasma will have formed until the arrival of the pulse maximum and the interaction takes place very close to the solid target surface. If a p-polarized laser pulse hits a target under an angle $< 90^\circ$, the electric field has component in target-normal direction. Assuming that the electrons are accelerated from the target into the vacuum by the first quarter cycle of this normal field, they will be re-accelerated in target direction by the second quarter cycle and pass their original position with $v_{\text{norm}} \approx v_{\text{osc}}^{\text{class}} = \frac{Ee}{\omega m_0}$. Once they entered the solid target, the accompanying electric field will be screened off evanescently - the laser can not enter the overdense region (Fig. 2.1). The inert electrons will then spread their kinetic energy in the target via collisions or leave the target on the back side.

In the following, the attention will be shifted to another type of acceleration mechanisms, which is based on collective excitations of the plasma. It will turn out that these mechanisms are even more powerful than the single-electron phenomena discussed in this section.

2.1.3 “Indirect” acceleration mechanisms: plasma waves & wake field

Summary: The collective oscillations at the plasma frequency constitute a spatial plasma wave. Electrons can co-propagate with this wave and gain energy by “surfing down” the charge density gradients.

In section 2.1.1 it has been described how the displacement of the electrons due to the pulse front creates periodic charge density modulations, which can be understood as a spatial plasma wave. An electron entering the domain of the wave will be accelerated along the charge density gradient, that is along the slope between the maximum and the minimum of the plasma wave. However, such an electron has to be injected into the wave with sufficient speed already in order to gain energy from it - electrons at rest will be simply passed due to the high phase velocity of the plasma wave [?].

In fact, a large number of very fast electrons is available, accelerated by the mechanisms presented in the previous sections. Once injected, they can remain on the leading edge of the first wave cycle, the *laser wake*, and co-propagate with the wave front for a certain time. In analogy to a surfer on an ocean wave, the electrons are thereby continuously accelerated

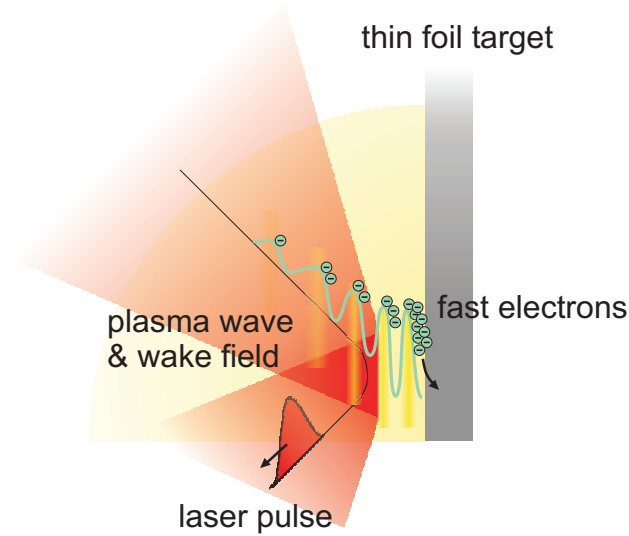


Figure 2.2: Wake field acceleration. The pulse front initiates a plasma wave due to charge oscillations. The plasma wave propagates with a phase velocity close to the speed of light. Electrons trapped in this wave are continuously accelerated along the charge density gradient and gain enormous amounts of energy.

“down the plasma wave” and can thus gain enormous amounts of energy, until the trapped electrons destabilize the wave and it breaks [?]. For a solid target - in contrast to underdense gaseous targets - the region of plasma wave formation must be assumed very confined. Due to the steep density gradient, the wave will thereby decrease in wavelength rapidly.

The process described here is known as *laser wake-field acceleration*. It occurs in different versions and proves to be a highly efficient target-normal acceleration scheme [30? , 31]. One can estimate the field strength along the wave slope by assuming all electrons displaced by half the plasma wavelength. The resulting field calculates as $E \approx \frac{n_e c e}{\epsilon_0 \omega_p}$ [14] and yields the huge value of $E \approx 3 \text{ GV/cm}$ for a typical electron density of $n_e = 10^{19} \text{ cm}^{-3}$, which exceeds conventional accelerators by a factor of 10^3 . Current research efforts are trying to extend the this co-propagation length of wave and electrons with the help of relativistic channels. At the JETI, distances up to $300 \mu\text{m}$ have been observed [32, 33]. Considering an acceleration with 3 GV/cm over this very distance, one finds a maximum energy of 90 MeV , which corresponds to the detected values. Wake field acceleration can thus exceed the direct laser acceleration (eq. 2.22) by more than one order of magnitude.

Up to this point, all presented acceleration mechanisms referred to electrons only. They have been classified as direct or indirect with respect to their either laser driven or laser (plasma) induced origin. When now aiming at ion acceleration, the situation is completely different.⁵ Ions possess a much bigger rest mass $m_i \approx A \cdot 1836 m_e$, A being the atomic mass

⁵It would be rather curious if this were not the case, since we derived some of the electron motions by

number, which raises the threshold for relativistic interactions accordingly. Presently available laser intensities do not pass this threshold as can be seen by calculating a_0 (eq. 2.21) for the ion rest mass, which rules out direct acceleration for MeV-proton production [24]. It was argued that in order to be injectable into a wake-field, particles have to possess a relativistic velocity already and hence plasma wave acceleration can be discarded for ions, too. All of this hints, that processes suitable for the creation of high energy proton beams will have to work on a much slower timescale. Possible acceleration schemes will be discussed in the following sections.

2.2 Ion acceleration

2.2.1 Front side acceleration

Summary: Different possible origins have been proposed for laser produced ions beams. Acceleration from the target front side does not explain the properties of the observed beams sufficiently.

When a high intensity laser pulse ($I > 10^{18}$ W/cm²) is focussed on a thin metal foil (1–20 μm), highly charged ion beams (10^{-10} C) of considerable energy (1 – 50 MeV) are observed. The ion beams consist predominantly of protons, the origin of which has been widely discussed in the literature. Although all authors in principle agree on that the protons stem from contamination layers on the target surfaces, the opinions differ about the question, whether the source layer of the observed protons is located on the front [5, 34, 35] or on the back surface [36–39]. Consequently, the controversy has also been expanded onto the origin of heavy ions [40, 41].

In the opinion of the author, the argument is decided at least for the laser intensities of the present experiments. The experiments of this thesis rest fully upon rear side acceleration, that is the TNSA principle (cf. below), and all results verify its existence without doubt. However it has been pointed out by d’Humieres et al. [42], that especially for higher laser intensities the two sources in question will produce protons of the same order of energy and thus overlap in their effective domains. Thus, a brief description of the front side mechanisms shall be given first.

Different schemes have been proposed for a acceleration from the target front. A popular one was introduced by Clark et al. [43] and Krushelnik et al. [5], which explains the observed collimation of the proton beam in forward direction with *ultrastrong magnetic fields* appearing in the target due to the electron current. Protons from the rear side, they argue further, would require inconceivably large magnetic fields for the same collimation. The detected protons are thus being carried along with the electron current, resulting in energies 18 MeV for the Vulcan Petawatt laser.

assuming the ions as fixed.

A second scheme explains the proton energy by the electric field arising from the ponderomotively pushed electrons [35]. The electrons are expelled until the restoring coulomb force balances the ponderomotive force. Under this assumption ($\Phi_{\text{coul}} = \Phi_{\text{pond}}$), Kaluza [24] finds an expression for the maximum energy gain from the front

$$E_{\text{p}}^{\text{front}} = 1.25 k_{\text{B}} T, \quad (2.26)$$

in agreement with Sentoku et al. [35], which yields for $k_{\text{B}}T \approx \Phi_{\text{pond}}$ and $a_0 = 4.3$ maximum proton energies of $E_{\text{cutoff}} = 2.2 \text{ MeV}$. This agrees with typical observed values. Since the laser pulse has a three-dimensional profile and the electrons are scattered in all gradient directions, this front side approach could also explain the weaker proton beams in backward direction, which were observed in various experiments also at the JETI. However, one can pose the question why the most intense proton beams are then observed in target normal direction and not in straight-through, i.e. laser direction, as the theory of the ponderomotive force would suggest. Moreover, the lifetime for such ponderomotively induced fields remains a mere guess and the backscattered protons might thus be explained better by the delayed *Coulomb explosion* of the ions left-behind in the plasma region.

In a third scheme, the ponderomotively induced electric field is assumed to accelerate the whole positive front surface forward, which was named “hole-boring” [44–46]. This deformation launches an ion wave into the target, which can accelerate further ions on its way via *collisionless shocks* [47, 48].

In conclusion, the presented front side mechanisms certainly do play a role for laser plasma acceleration, and in practice their effects can hardly be disentangled from the rear side ones. However, strong evidence from both theoretical and experimental work indicates that rear side acceleration dominates the situation in most cases, in particular for the ultrashort pulse regime of high repetition rate table-top lasers. In the following, a detailed description these back side events will be given.

2.2.2 Rear side acceleration: Target Normal Sheath Acceleration & Debye Sheath

Summary: The expelled electrons at the back side are trapped in the Coulomb potential of the ionized target and form a quasi-electrostatic sheath for about the laser pulse duration. The resulting electric field is of the order of $\text{MV}/\mu\text{m}$ and acts in target-normal direction. Protons abundant on the back surface are accelerated in this field

The rear side acceleration can be explained very graphically: As the strongly forward-accelerated electrons (cf. sections 2.1.2 & 2.1.3) penetrate the foil, they will ionize further atoms on their way and, when emitted at the back side into the vacuum, leave behind a strongly ionized target. Consequently, an electric field will form between the negative electron bunch and the

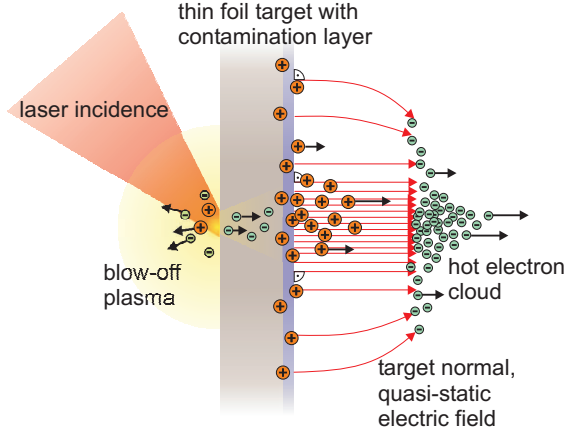


Figure 2.3: Target Normal Sheath Acceleration (TNSA). Fast electrons from the laser plasma penetrate a thin solid target and are emitted at the back side. A strong quasi-static electric field builds up between the electron bunch and the ionized target, which acts normally to the metallic surface. Subsequently, protons abundant on the surface in the form of contamination layers will be accelerated along field gradient the in a well-defined way.

positively charged target, which suffices to literally tear out protons from the back surface. The resulting field has a significantly longer lifetime than those responsible for the electron acceleration [37] and can therefore - from an electron perspective - be considered quasi-static.

This explanation for the observed proton beams was presented first in 2000 by Hatchett et al. [37] and given the name *Target Normal Sheath Acceleration (TNSA)* [38] in agreement with the original use [49]. From the integration of the Maxwell equations

$$\begin{aligned}
 \int d\vec{A} (\nabla \times \vec{E}) &= \oint ds \vec{E} & (2.27) \\
 &= l \vec{t} \cdot (\vec{E}_2 - \vec{E}_1) \\
 &= -\frac{1}{c} \int d\vec{A} \cdot \frac{\partial \vec{B}}{\partial t} \\
 &= 0
 \end{aligned}$$

it follows that \vec{E} acts indeed normally to the surface (Fig. 2.3), where \vec{t} is the tangential unit vector parallel to the target surface and l an infinitesimal path element. The protons will thus be accelerated perpendicularly to the target into the back side hemisphere until they compensate the electron charge.

Similar to the conditions for the plasma waves, a restoring Coulomb force will counteract the charge separation. Therefore, only the fastest electrons will escape the target vicinity,

shielded from the ion attraction by their slower successors, whereas the main part of the hot electron population will be trapped in the Coulomb potential and constitute an exponential sheath behind the target according to the Boltzmann distribution [37]

$$n_e(r) = n_e(0) \cdot \exp\left\{-\frac{e\Phi_{\text{ion}}(r)}{k_B T}\right\}. \quad (2.28)$$

Here, Φ_{ion} is the Coulomb potential of the ionized target that counterbalances the recession of the electrons, and T is again the hot electron temperature. This sheath will be retained as long as the laser pulse drives hot electrons through the target, that is, for about the laser pulse duration $\tau_{\text{pulse}} = 80$ fs. The reaction time of the electrons is characterized by the plasma period $\tau_p = 2\pi/\omega_p \approx 3 \times 10^{-15}$ s and hence shorter than τ_{pulse} , which justifies the assumption that such a sheath will form quickly and set the conditions for the slower proton acceleration.

The extent of the sheath corresponds to scale length of a screened Coulomb potential in a free electron plasma, the *Debye length*

$$l_D = \left(\frac{\varepsilon_0 k_B T}{e^2 n_e}\right)^{\frac{1}{2}} \quad (2.29)$$

$$= 0.24 \mu\text{m} \times \sqrt{\frac{k_B T / \text{MeV}}{n_e / 10^{21} \text{cm}^{-3}}}, \quad (2.30)$$

which has coined the term *Debye Sheath* for the quasi-static part of the TNSA field (Fig.2.4). Assuming that the electron density directly behind the target resembles the plasma conditions from the front ($n_e \approx n_c = 1.75 \times 10^{21} \text{1/cm}^3$), and assuming furthermore the electron energy $k_B T$ to be roughly 3 MeV [50], one obtains a Debye length of $l_D = 0.31 \mu\text{m}$.⁶

The electric field at the surface can be estimated by assuming that the whole charge contained in the Debye sheath, $Q = \int d^3r \rho(\vec{r})$, is located on a capacitor surface at $z = l_D$. For an exponential density profile

$$n_e(\vec{r}) \equiv n_e(z) = n_e(0) \exp\left\{-\frac{z}{l_D}\right\} \quad (2.31)$$

the total charge amounts to

$$\begin{aligned} Q &= -e \int d^3r n_e(z) \\ &= -e n_e(0) A_{\text{em}} l_D \end{aligned}$$

where n_e has been assumed constant in radial direction over the electron emission cross section

⁶Hatchett et al. assume an electron density of $n_e \sim 10^{19} \text{1/cm}^3$ behind the target and conclude a Debye length of $2.4 \mu\text{m}$ for a 1 MeV electron population [37]. This assumption is reasonable for the 1 kJ > 0.5 ps pulses they use, but not applicable to the ultrashort pulse regime of our experiments.

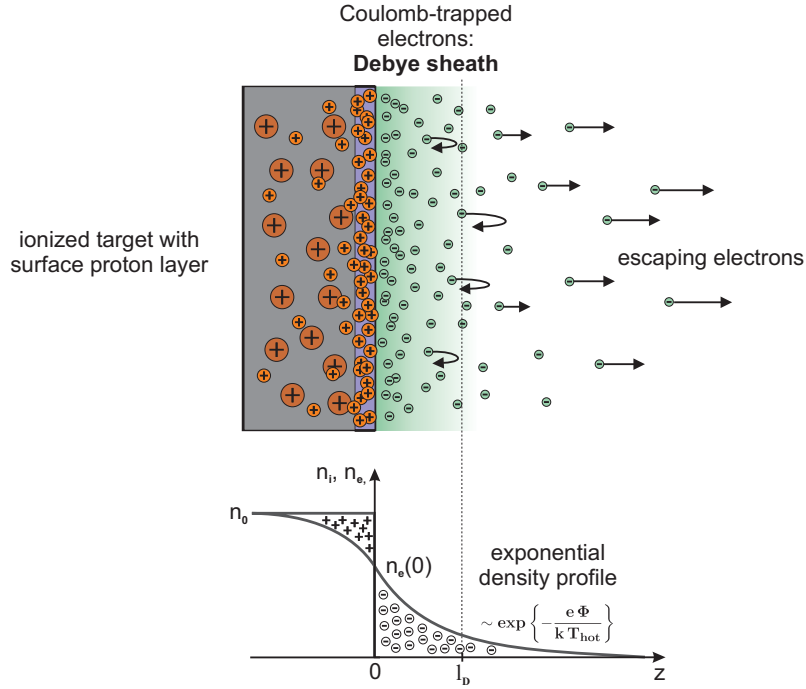


Figure 2.4: Formation of the Debye Sheath. A large part of the hot electron population is being coulomb-trapped within the Debye length at the back side of the target and constitutes a dense, quasi-static sheath. Light protons from the top surface layer can be accelerated by the resulting electric field.

A_{em} . For the homogeneous field of a capacitor, one obtains

$$\left| \overrightarrow{E_{\text{TNSA}}} \right| = \frac{|Q|}{\varepsilon_0 A_{\text{em}}} \quad (2.32)$$

$$= \frac{1}{\varepsilon_0} e n_e(0) l_D$$

$$= \sqrt{\frac{k_B T n_e(0)}{\varepsilon_0}}. \quad (2.33)$$

For the above values of $n_e = 1.75 \times 10^{21} \text{ cm}^{-3}$ and $k_B T = 3 \text{ MeV}$, this corresponds to a field strength of 10^{13} V/m (10 Megavolts per microns!), which exceeds the field strength in conventional accelerators by a factor of 10^5 .

The resulting field lies well above the threshold for the field ionization of Hydrogen ($E_{\text{H}}^{\text{ion}} \approx 3 \times 10^{10} \text{ V/m}$), which explains why protons are so readily accelerated from the Hydrogen rich contamination layer (cf. section 2.2.3) on the target back side. The conversion efficiency from laser energy into proton energy can reach 10 – 12% [51, 52], but does typically not exceed 2% [4, 53].

The *maximum energy* of a proton obtained from the TNSA field is given by

$$E_{\text{cutoff}} \approx eE_{\text{TNSA}} l_{\text{D}} \quad (2.34)$$

and yields 3.1 MeV for the above values, which agrees well with the observed proton spectra (cf. section 3.3.1).

The time that a proton needs to travel the Debye length is given by

$$t = \sqrt{\frac{2l_{\text{D}} m_{\text{p}}}{eE}}, \quad (2.35)$$

which amounts to 30 fs for the above values. Since the quasi-static field exists at least for the duration of the laser pulse, the top layer protons will indeed acquire this maximum kinetic energy. The accelerated proton front will start to deplete the electric field. However, since the energy deposited in the electron ensemble is much larger than the one transferred to the proton ensemble⁷, the depletion should be negligible. The acceleration of deeper sited protons can thus be assumed limited rather by screening effects.

The rear side acceleration of protons with the the help of fast plasma electrons proves to be a very reliable mechanism. Experimental evidence for TNSA was reported by many groups [8, 36–39, 54–56] and confirmed in numerous simulations [42, 51, 57–59]. In the following, a number of beam properties shall be derived from the physically telling picture of TNSA.

2.2.3 Features of Target Normal Sheath Acceleration

Summary: Laser accelerated proton outmatch conventional accelerators in terms of emittance and pulse duration. The protons stem from contamination layers on the surface, which can be reduced (ablation) or enhanced (double layer targets). The source size of the protons comprises several 10 μm and the emission happens within energy cones. For optimum yield, different target and laser properties have to be considered, like target material & thickness or prepulse duration. In the present case, the prepulse contrast is better than 10^{-9} .

Transverse & longitudinal emittance; symmetry & inhomogeneity of the field

In the previous section it was shown that electric field acts normally to the target surface, which agrees with collimated forward-acceleration of the protons observed in all experiments. A related property known from particle physics is the *transverse emittance* $\varepsilon_{\text{trans}} = \frac{1}{\pi} \int n_{\text{p}}(x, p_x) dx \frac{1}{p_z} dp_x$ [60] as measure for the laminarity of the beam, where x and $\frac{1}{p_z} dp_x$ are the transverse position and divergence, respectively, and n_{p} is the proton density distribution.⁸

⁷The conversion efficiency from laser energy into hot electrons typically exceeds 10%. In comparison to the conversion efficiency for protons, this means that only about 10 – 20% of the electronic energy is deprived by the protons.

⁸In the most simple case, the transverse emittance equals the product of spot size and beam divergence.

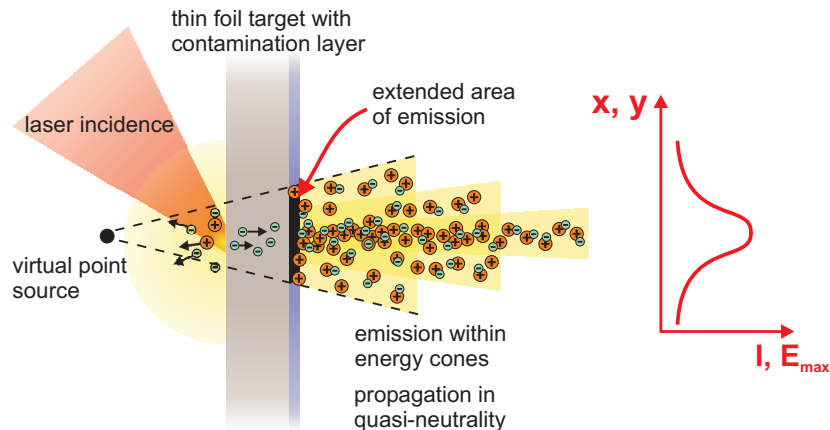


Figure 2.5: Proton emission within energy cones; real and virtual source size. The TNSA mechanism features an extended region of emission on the target. The collimation properties of the proton beam can be equally interpreted as resulting from a virtual point source located in front of the target. The emission of the protons happens within energy cones; that is, the fastest protons show the smallest divergence.

For laser plasma accelerators, values of $\varepsilon_{\text{trans}}^{\text{las}} < 0.004 \text{ mm mrad}$ are attained [60], which out-matches conventional accelerators by a factor of 10^3 (e.g. $\varepsilon_{\text{trans}}^{\text{conv}} \approx 3.5 \text{ mm mrad}$ for the CERN SPS). The excellent beam quality can be ascribed to a very small source size (cf. below) with the protons initially at rest and is supported by the quasi-neutrality of the beam⁹.

The remaining transverse momentum can be explained by the coulomb repulsion among the particles at an early stage of propagation [60, 61]. Since slow protons take longer until they arrive at the detection plane, they have more time for transverse propagation and hence display a larger opening angle. This leads to a proton emission within energy cones - the fastest protons show the smallest divergence and vice versa (Fig. 2.5) [60, 62].

The emission within symmetrical cones indicates that the accelerating field possesses a bell-shaped radial symmetry. This agrees with earlier reasoning about the longitudinal electron acceleration processes and the symmetry between incident and reflected laser pulse (cf. section 2.1.2 & 2.1.3). The transversal inhomogeneity of the accelerating field explains, together with screening effects for the deeper-sited protons, the exponential energy distribution of the observed proton spectra: protons located at the boundary of the field or behind faster protons will gain less energy until the field is depleted. Thus, the resulting spectrum has a strong correlation to the initial position of the protons on the target, which will be important when talking about the generation of monoenergetic protons.

Since the TNSA field persists for the pulse duration only, the proton beam is pulsed as

⁹The accelerated proton bunch is accompanied by a number of co-moving, “colder” hot electrons, which compensate the proton charge.

well. This property is covered by the *longitudinal emittance*, $\varepsilon_{\text{long}} = \Delta\tau_{\text{envelope}} \cdot \Delta E_{\text{kin}}$, which as the product of initial pulse duration and energy spread gives a measure for the "bunching" of the proton ensemble. Once again, the results achieved for laser plasma accelerators ($\varepsilon_{\text{long}}^{\text{las}} \approx 10^{-4}$ eV s) exceed the values of conventional accelerators by orders of magnitude ($\varepsilon_{\text{long}}^{\text{conv}} \approx 0.5$ eV s for CERN SPS) [60]. Nonetheless, since the ensemble contains a whole spectrum of different energies, the the proton pulse will broaden during the propagation despite the excellent initial confinement.

Proton source size & contamination layer

As mentioned above, the excellent transverse emittance hints a small source size. One can investigate the region of proton emission on the target with the help of mesh magnification experiments. The values given in the literature range from $30 \mu\text{m}$ [60] to $250 \mu\text{m}$ [63, 64] for the source diameter, which furthermore varies with the observed kinetic energy. For fast protons ($E_{\text{kin}} > 0.8 \text{ MeV}$), the source size was determined to be $< 80 \mu\text{m}$ [64]. This means that the extent of the accelerating field on the surface exceeds the size of the laser focal spot by far - an important feature for the production of monoenergetic proton beams discussed below. From the expansion of the beam, Borghesi et al. [55] deduced that the protons can equally be ascribed to a much smaller, *virtual source* ($< 10 \mu\text{m}$) located several hundred microns in front of the target (Fig. 2.5), which explains the small emittance.

The TNSA mechanism rests upon the fact that protons are located on the back surface of the target. These protons stem from the adsorption of water and oil vapours abundant in the evacuated chamber, which form a thin *contamination layer* on all solid components. For a $15 \mu\text{m}$ thin gold foil in a vacuum of 2.6×10^{-5} mbar, the contamination layer was determined to be 12 \AA thick (i.e. a quasi-monolayer) and consist of 27% gold, 60.5% Hydrocarbons and 12.2% water vapour [39]. This amounts to a layer density of $5.94 \frac{\text{g}}{\text{cm}^3}$ and a particle density for Hydrogen of $2.24 \times 10^{23} \frac{1}{\text{cm}^3}$ [39]. For a source size of $V_{\text{source}} = \pi(50 \mu\text{m})^2 \cdot 12 \text{ \AA} = 9.4 \mu\text{m}^3$, a total of 2×10^{12} protons will be available for acceleration.

Manipulation of the proton source

For experimental purposes it is desirable not only to know about the source, but to acquire control over the source parameters. With this respect, two scenarios are conceivable: first, one could try to enlarge the layer and thus increase the number of available protons; secondly, one could reduce the layer (or get rid of it altogether) and examine the consequences. Both variants have been investigated thoroughly.

The *reduction of the proton layer* was first carried out as a proof of TNSA. Manipulations of the layer on the target rear side showed an immediate impact on the proton yield, which delivered a strong argument against the front side theory. A disposal of the contamination mono-layers can be achieved with various methods, including resistive heating [54, 65, 66], ion sputtering [39, 65] and laser ablation (Fig. 2.6) [9, 62, 65, 67]. All of these manipulations can reduce the beam intensity to almost zero. As the proton yield decreases, a simultaneous

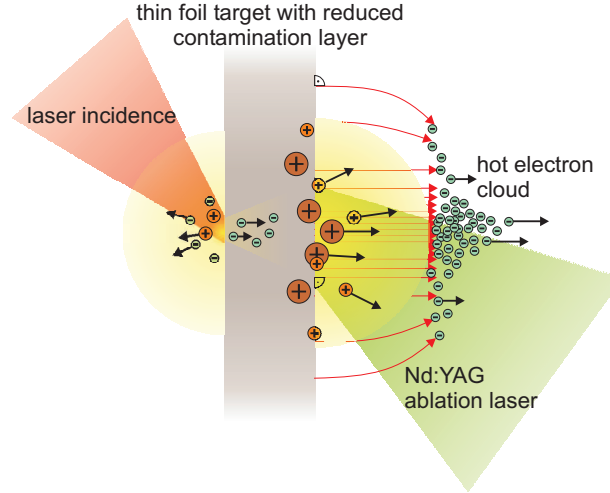


Figure 2.6: Reduction of contamination layer via laser ablation. The suppression of the protons allows to accelerate heavy ions, which were screened before from the field.

increase in heavy ion yield is detected. This experimental observation is plausible since the light protons are accelerated by the field more rapidly than the heavier ions and thus screen them from the field. If the protons are suppressed, most of the field energy will be deposited onto the ion species with the next lower q/m ratio, probably Carbon with a high degree of ionization. If all contaminants are ablated completely, one can also observe the acceleration of heavy ions originating from the target material itself (e.g. Titanium or Gold) [54, 65, 66].

On the contrary, one can try to install an additional, Hydrogen rich layer on the back surface and thus enforce the proton acceleration [51, 65, 68]. With this *double layer targets*, an increase in proton flux of a factor of 80 was reported in [56].¹⁰ Double layer targets ideally consist of a high- Z "carrier foil", which provides a sufficient number of electrons, and a thinner low- Z "source foil", that can be attached to the former in a controlled manner (Fig. 2.7). The proposed *high- Z / low- Z ratio* ensures a good contrast for the acceleration of the light ions against the heavy ion background. Because of their large reservoir of Hydrocarbons, organic materials like polymers represent a good choice for the source layer (c.f. section 3.1.3).

Target conditions

The proton yield crucially depends on the selected target material. In principle, a high- Z material can provide more electrons for the sheath acceleration. However, at the same time such a high- Z material will slow down the fast electrons more strongly on their way through the target due to the higher cross section for coulomb interaction. These counteracting tendencies result in the existence of an *optimum target thickness* for every material [28, 42, 62, 68, 69]. When exceeding this thickness, the electron current will be transmitted less efficiently; for a

¹⁰This large factor could, however, not be verified for our experimental conditions (cf. section 3.3.1 and [62]).

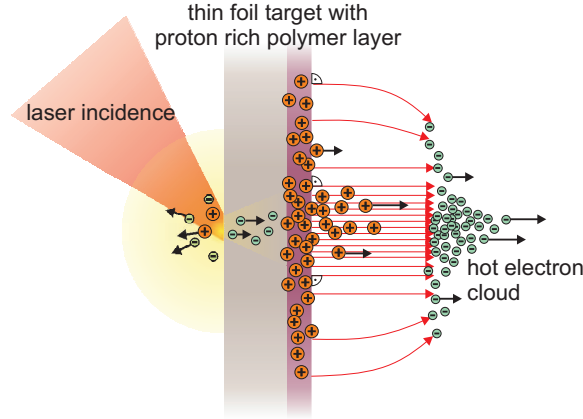


Figure 2.7: Double layer target. The attachment of an additional Hydrogen-rich layer on the back surface of the foil target increases the proton yield.

thinner target, the expanding preplasma can already destroy the structural integrity of the foil before the arrival of the main pulse. For double layer targets, one must determine the optimum combination of two different layer thicknesses and materials. It will turn out that the quality of the monoenergetic proton beams as discussed below in fact strongly depends on the thickness of the proton rich layer.

ASE & prepulse dependence

In section 2.1.1 it has been argued that the target is sensitive to intensities well below the peak intensity already. For high intensity lasers, two characteristic "signals" are known to precede the main pulse, which have to be considered when trying to establish TNSA: the *prepulse* and the *Amplified Spontaneous Emission (ASE)*. The prepulse consists of light from the previous roundtrip cycle in the regenerative amplifier, which was ejected due to the limited bandwidth of the pockels cell and ran through the subsequent amplification steps. ASE (which is sometimes also referred to as prepulse) is the amplified noise due to spontaneous emission, which leads to a rising pedestal from the time when the pockels cell "opens" until the arrival of the main pulse front. Both effects are able to provoke a plasma on the target already and thus alter the conditions for electron and proton acceleration substantially. A strong prepulse can even destroy the target. Studies about the ASE influence on proton acceleration yielded that for every target thickness there is an optimum ASE duration and intensity [28, 69].

In the presented experiments, the ASE length could be varied from 0.3 – 3 ns with the help of an additional, fast-switching pockels cell. The pockels cell also suppressed the prepulse completely. With these additional measures, a contrast of the laser system of $I_{ASE}/I_{main} < 10^{-9}$ was achieved [70].

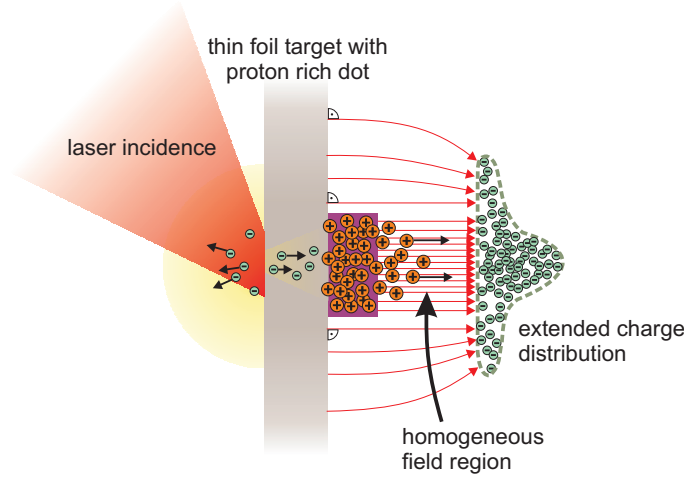


Figure 2.8: Confined acceleration within the homogeneous central field region. The extended electron bunch acts like a capacitor on the positively charged target. If screening mechanisms are small, protons located close to the symmetry axis will be accelerated monoenergetically.

2.2.4 Monoenergetic proton beams from a spatially confined source

Summary: The spectrum of the accelerated protons has a strong correlation to the initial proton distribution on the target. The accelerating TNSA field features a homogeneous central field region. Thus, if the proton source is confined to this homogeneous region and sufficiently thin, the protons will be detached as a whole and accelerated in a monoenergetic manner.

In the precedent sections, all the components necessary for the pursuit of monoenergetic proton production have been introduced and shall now be assembled. Since the electrons stem from an extended target region ($\approx A_{\text{foc}}$), the expelled electron bunch will appear to a single proton located on the surface as a macroscopical charge distribution. From this macroscopical extent and the radial symmetry of the beam it can be deduced that the resulting field will have a homogeneous region close to the symmetry axis, somewhat comparable to a capacitor.

Now consider a scenario where all available protons are localized in this central region: If there is no proton to be accelerated from outside the homogeneous field, all protons will experience the same accelerating potential. If furthermore the proton layer is sufficiently thin, screening effects are negligible; the proton bunch will be detached as a whole and accelerated in a monoenergetic manner. Hence, the proton beam will not broaden temporally during the course of propagation, either. One has therewith found a method to create *monoenergetic proton beams by confining the proton source* to the region of the homogeneous electric field.

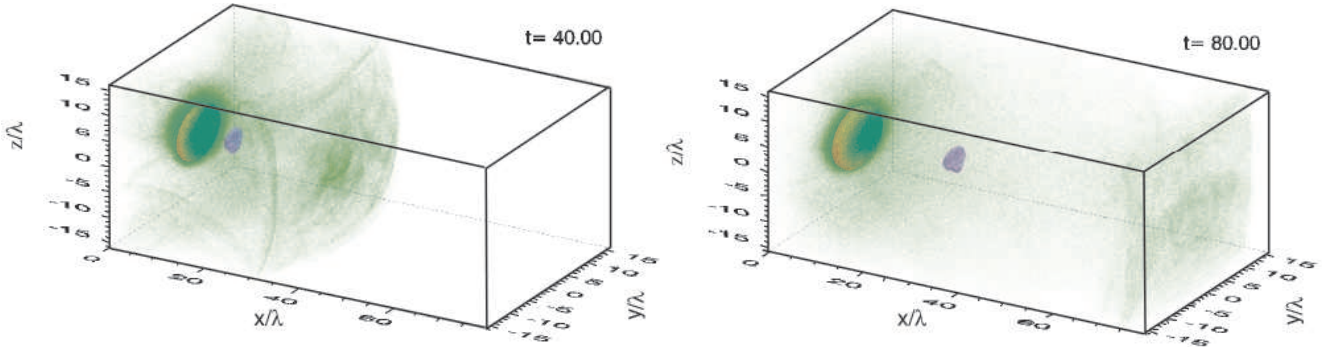


Figure 2.9: Simulation of the homogeneously accelerated proton bunch as presented in ref. [58]. The two pictures show simulation boxes at different stages of temporal evolution (t given in laser cycles $2\pi/\omega$). The electron distribution is given as a “green gas”. One can clearly see the detached proton bunch (blue) departing from the heavy ion background (red). The axis distances are given in laser wavelengths λ .

The discussed scheme for the production of monoenergetic protons rests upon the strong dependency of the energy spectrum on the spatial distribution of the protons on the surface (cf. section 2.2.3). It is clear that a suitable proton source cannot be provided by the widespread contamination. Therefore, Bulanov, Esirkepov et al. [51, 58] proposed the use of a micro-structured double layer target. The selective positioning of the protons on the surface allows to exploit the favoured parts of the field. In the following, the derivation of this spatial dependency as given by Bulanov and Esirkepov et al. [51, 58] shall be recapitulated.

For a particle ensemble - in this case the proton bunch - the number of particles per unit of phase space volume, dn , is given by the distribution function $f(\tilde{x}(t), \tilde{v}(t), t)$ of the ensemble:

$$dn = f d\tilde{x} d\tilde{v}. \quad (2.36)$$

The distribution function must obey the Boltzmann equation $\frac{df}{dt} = \left(\frac{\partial f}{\partial t}\right)_{\text{source}}$, which here assumes the form

$$\frac{\partial}{\partial t} f + \tilde{v} \frac{\partial}{\partial \tilde{x}} f + \frac{e}{m_p} E_0(\tilde{x}) \frac{\partial}{\partial \tilde{v}} f = 0. \quad (2.37)$$

The equation features two continuity terms (first two terms) plus an external field term (last term). The source term has been set zero, which corresponds to a neglect of collisions among the protons and is supported by the excellent transverse emittance (cf. section 2.2.3). Both \tilde{x} and \tilde{v} are here generalized Langrangian coordinates. Equation (2.37) can be solved with an initial distribution function $f_0(\tilde{x}_0, \tilde{v}_0) = f(\tilde{x}(0), \tilde{v}(0), 0)$, which attains

$$f_0(\tilde{x}_0, \tilde{v}_0) = n_0(\tilde{x}_0) \delta(\tilde{v}_0), \quad (2.38)$$

where $n_0(\tilde{x}_0)$ is the original proton distribution and all particles are at rest before the acceleration, fixed by the Dirac delta function. If one now wants to derive the energy spectrum, the particle density can be rewritten as

$$dn(\tilde{x}, \tilde{v}) = f d\tilde{x} d\tilde{v} = f \tilde{v} dt d\tilde{v} = f \frac{1}{m_p} \tilde{p} d\tilde{v} dt = f \frac{1}{m_p} dE dt, \quad (2.39)$$

which yields the number of particles per energy interval, i.e. the spectrum, by integrating over time:

$$\begin{aligned} N(E) dE &= \int dt f \frac{1}{m_p} dE \\ &= \frac{1}{m_p} \int dt n_0(\tilde{x}_0) \delta(\tilde{v}_0) dE \\ &= \frac{1}{m_p} \left. \frac{dt}{d\tilde{v}} \right|_{\tilde{v}=\tilde{v}_0} n_0(\tilde{x}_0) dE \end{aligned} \quad (2.40)$$

In the last step, the delta function has been eliminated by transcribing the time integration into a velocity integration using the Jacobian $\left. \frac{dt}{d\tilde{v}} \right|_{\tilde{v}=\tilde{v}_0}$. If one finally applies the identity

$$\left. \frac{d\tilde{v}}{dt} \right| = \frac{1}{m_p} \left. \frac{d\tilde{p}}{dt} \right| \equiv \frac{1}{m_p} |\tilde{F}| = \frac{1}{m_p} \left. \frac{d\Phi}{d\tilde{x}} \right|, \quad (2.41)$$

Φ being the potential of the field and hence equal to the proton energy E , one obtains the relation:

$$N(E) dE = \frac{n_0(\tilde{x}_0)}{\left. \frac{dE}{d\tilde{x}_0} \right|} dE. \quad (2.42)$$

Equation (2.42) is a general expression for the dependency of the spectrum on the initial spatial particle distribution $n_0(\tilde{x}_0)$ and not bound to any approximation about the configuration of the field yet. The term $\left. \frac{dE}{d\tilde{x}_0} \right|$ can be understood as a deposition of field energy onto a certain coordinate at $t = 0$. If \tilde{x}_0 is occupied by a proton, which is determined by $n_0(\tilde{x}_0)$, then $\left. \frac{dE}{d\tilde{x}_0} \right|$ represents the accelerating potential at the initial proton position.

Now transfer the results to the physical situation: The field acts only in target-normal direction (z -direction) and is constant within the central region A_{hom} . Assuming that the layer thickness Δz is constant, the Jacobian reduces to $\frac{dE}{dz_0}$ and equation 2.42 becomes

$$N(E) dE \approx A_{\text{hom}} \cdot n_0 [\Theta(0) - \Theta(\Delta z)] dz_0. \quad (2.43)$$

Leaving aside screening effects, the width of the energy spectrum dE becomes hence directly

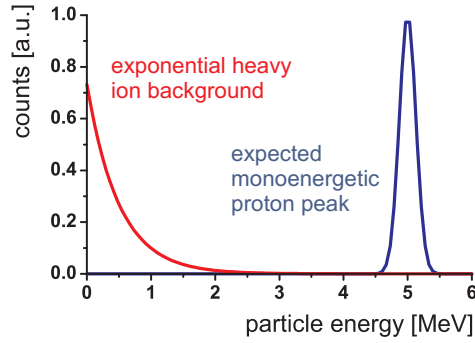


Figure 2.10: Expected spectrum for the confined acceleration from a dot. The homogeneously accelerated protons yield a monoenergetic peak. Heavier ions from the target material or abundant in the dot will be accelerated much slower and form an exponential background due to screening and the transversely inhomogeneous field.

proportional to the layer thickness. Here, n_0 is the constant layer density and the Θ -function delimits the layer extent. This follows exactly the intuitive behaviour predicted at the beginning of the section: *By confining the proton source to the central region of the field and also in thickness, one has found a method for the production of monoenergetic proton beams.*

Now, what kind of field configuration can be chosen for the description of the electron ensemble in front of the target? Bulanov, Esirkepov et al. identify the field of the ionized target with the one of a charged oblate ellipsoid of revolution, with the protons located on the surface [51, 58]. This appears somewhat curious since the real target is plain. However for a flat ellipsoid, the approximation is good; for the most part the field vectors will point in z -direction and the oblique contributions are "in agreement" with the divergent electron beam. The major semiaxis of the ellipsoid corresponds to R_{foc} , the minor one is given the name l_{min} .¹¹ The solution of this problem can be found in [71]

$$E_z = \frac{2}{3} E_0 R_{\text{foc}}^2 \frac{1}{R_\xi} \frac{\partial \xi}{\partial z} \quad (2.44)$$

$$E_\rho = \frac{2}{3} E_0 R_{\text{foc}}^2 \frac{1}{R_\xi} \frac{\partial \xi}{\partial \rho}, \quad (2.45)$$

with the abbreviations

$$\rho = \sqrt{x^2 + y^2} \quad (2.46)$$

$$\xi = \frac{1}{4} \left[\sqrt{\left(\rho - \sqrt{R_{\text{foc}}^2 - l_{\text{min}}^2} \right)^2 + z^2} + \sqrt{\left(\rho + \sqrt{R_{\text{foc}}^2 - l_{\text{min}}^2} \right)^2 + z^2} \right] - R_{\text{foc}}^2 \quad (2.47)$$

$$R_\xi = (\xi + R_{\text{foc}}^2) (\xi + l_{\text{min}}^2)^{\frac{1}{2}}. \quad (2.48)$$

¹¹In the limit $l_{\text{min}} \rightarrow 0$, one would arrive at a charged disk.

E_0 determines the magnitude of the field and requires further specification. Close to the axis, the field points in target normal direction only and the radial component E_ρ vanishes. For $\rho \approx 0$, the target-normal component E_z yields [51]

$$E_z \approx \frac{2}{3} E_0 R_{\text{foc}}^2 \cdot \frac{1}{R_{\text{foc}}^2 - l_{\text{min}}^2 + z^2}. \quad (2.49)$$

Close to the surface ($z \approx l_{\text{min}}$), the axis-near field therefore proves to be locally uniform:

$$E_z^{\text{hom}} \approx \frac{2}{3} E_0. \quad (2.50)$$

The magnitude of the field can be derived from the charge density ρ_{el} of the ionized target:

$$\nabla \vec{E}_0 = \frac{\rho_{\text{el}}}{\varepsilon_0} = \frac{1}{\varepsilon_0} e n_i \bar{Z}_i. \quad (2.51)$$

Here, n_i is the atomic density and $\bar{Z}_i e$ the average degree of ionization. One obtains the field strength by integration of both sides

$$\begin{aligned} \int d^3 r \nabla \vec{E}_0 &= \oint d\vec{A} \cdot \vec{E}_0 \\ &= \pi R_{\text{foc}}^2 E_0 \\ &= \int d^3 r \frac{1}{\varepsilon_0} e n_i \bar{Z}_i \\ &= \pi R_{\text{foc}}^2 d_{\text{target}} \frac{1}{\varepsilon_0} e n_i \bar{Z}_i \\ \Rightarrow E_0 &= \frac{1}{\varepsilon_0} e n_i \bar{Z}_i d_{\text{target}}, \end{aligned} \quad (2.52)$$

where the assumption was made that the ionized region is a cylinder with the focal spot as base area and a height given by the target thickness d_{target} . Returning now to the target-normal field (eq. 2.50), one finally obtains for the homogeneous region:

$$E_z^{\text{hom}} \approx \frac{2}{3 \varepsilon_0} e n_i \bar{Z}_i d_{\text{target}}. \quad (2.53)$$

The accelerating field depends primarily on the amount of expelled charge, which is covered by the phenomenological quantities \bar{Z}_i and d_{target} , that is the average ionization and the thickness of the target. One can derive an actual value for the field (which was, however, not done by Bulanov et al.) by noting that $e n_i \bar{Z}_i d_{\text{target}} \cdot \pi R_{\text{foc}}^2$ equals the total charge Q of the target, so that equation (2.53) can be written as

$$E_z^{\text{hom}} \approx \frac{2Q}{3 \varepsilon_0 \pi R_{\text{foc}}^2}. \quad (2.54)$$

Recalling that the proton source size (i.e. the region of emission A_{em}) was demanded to be about the focal spot size, equation (2.54) agrees with the earlier approximation about the TNSA field (eq. 2.32) except for a factor of $2/3$, which suggests that the homogeneous part of the field covers about this fraction of the total field.

In conclusion, a concept was presented that proves the feasibility of TNSA for the production of monoenergetic proton beams from laser plasmas. This concept makes use of the homogeneous character of the field close to the z -axis and imposes two requirements on the target: first, the proton source has to be confined to the central region of the accelerating field; secondly, the applied layer has to be sufficiently thin in order to prevent screening. In the following sections, the reader will be presented the experimental realization of these requirements.

3 Experiment

3.1 Setup

3.1.1 Laser

Summary: The JETI is a femtosecond Ti:Sa laser system with three amplification stages operating at 10 Hz. The system delivers 0.8 J within 80 fs and 70 mm beam diameter, which was focussed to an intensity of $\mathcal{I} = 4 \times 10^{19}$ W/cm² on target.

The Jena laser system JETI (Fig. 3.1) is based on a Titanium:Sapphire (Ti:Sa) *Oscillator*, which delivers 10 nJ - pulses of $\tau = 45$ fs duration at a rate of 80 MHz. The ultrashort pulses are generated via Kerr-lens mode locking and have a spectral width of $\Delta\lambda \sim 16$ nm around a central emission wavelength of $\lambda_L = 795$ nm. The oscillator is pumped by a diode pumped cw-Neodym:YVO₄ laser. Since it is not possible to amplify each of the 80 million pulses per second to the desired intensities, a *pulse picker* consisting of a fast pockels cell and a subsequent polarizing beam splitter is used to reduce the repetition rate to 10 Hz.

The intensity I of a laser pulse is given by the pulse energy E per beam cross section A and pulse duration τ ,

$$I = \frac{E}{A\tau}. \quad (3.1)$$

For the JETI, the final pulse energy is achieved by a chain of three amplification stages, a regenerative amplifier and two Ti:Sa multipass schemes, all of which are pumped by SHG Nd:YAG lasers. The smallest value for A is in principle determined by the laser wavelength and the aperture of the focal elements, but in practice by the quality of the final parabolic mirror and its adjustment ($A_{\text{real}} = 5 \mu\text{m}^2$). The pulse duration is given by the initial oscillator conditions and not reduced afterwards.

The key technique for amplification in high intensity laser systems is *chirping* [72]. In Chirped Pulse Amplification (CPA), a dispersion is imposed on the spectrally broad laser pulses with the help of either gratings or prisms. The temporally stretched pulse (here $\tau_{\text{stretch}} = 150 \text{ ps} \sim 3 \cdot 10^3 \tau$) can then be amplified without causing damage on the optical components. After the pulse has acquired its final energy, the dispersion is compensated by a compressor. In addition, *telescope optics* are inserted between all amplification stages in order to not damage the compressor grating.

The first, *regenerative amplifier* is a resonator that can be gated for injection and ejection mode by a Pockels cell and a polarizing beam splitter. During the round trips, the pulses

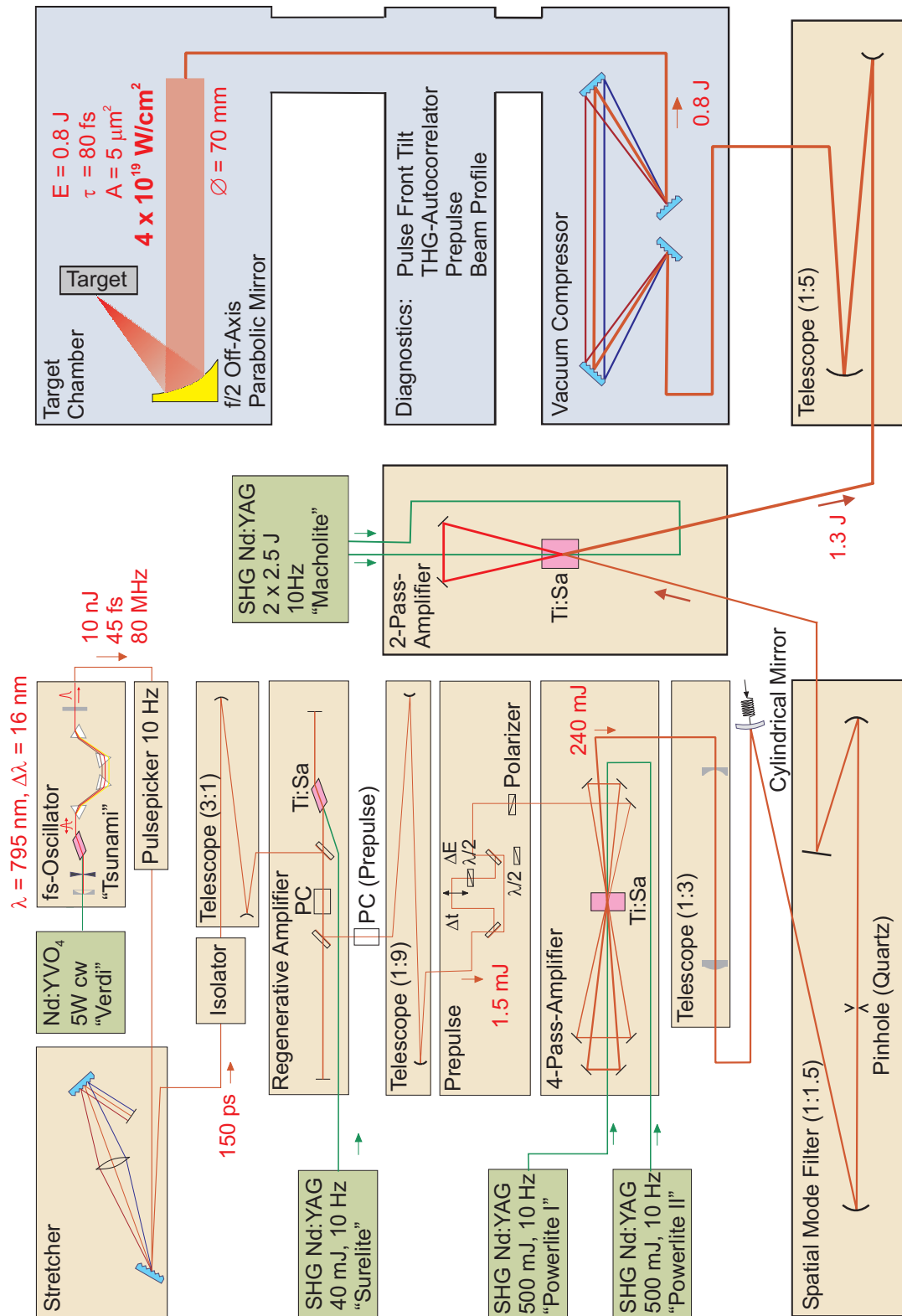


Figure 3.1: The Jena 15 TW Ti:Sa Laser System (JETI) with 10 Hz repetition rate.

are successively amplified to a saturation value of about 2.5 mJ. The regenerative amplifier is followed by a second pockels cell with short gating times, which is used for the *suppression of the prepulse and ASE* [70] (cf. section 2.2.3).

The next amplification stage is given by a *4-pass “butterfly”*, which raises the pulse energy to about 240 mJ.¹ In order to suppress the diffraction collected up to this point, the light is focussed through a spatial mode filter (pinhole). The pulse then reaches the third amplification stage, a *2-pass butterfly*, where it acquires its final energy of about 1.3 J.

After the light has passed the next component, the *compressor*, its intensity will suffice to ionize air. Therefore, all remaining components are kept under vacuum. With a beam diameter of 7 cm, the beam enters the compressor and retrieves nearly its initial length, that is $\tau = 80$ fs. The transmission efficiency of the compressor is limited to 60%. The final laser pulse is characterized with several *diagnostic tools*: a third order auto-correlator for the determination of the pulse length, a prepulse analyzer and a pulse front tilt measurement. A detailed description is given in refs. [50, 70].

After this characterization, the pulse enters the target chamber, where it is focussed onto the target by a *gold coated, off-axis parabola* with 12 cm focal length. The parabola can be adjusted roughly with the focus of a Helium Neon (HeNe) laser, which is aligned collinearly to the Ti:Sa beam. The fine adjustment is achieved with a microscope objective that images the weakened Ti:Sa focus onto a CCD camera. According to the observed aberration, the parabola’s tilt is then corrected in horizontal and vertical direction. The *CCD observation of the focus* also serves for the determination of the focal spot size A , which typically reaches values as low as $5 \mu\text{m}^2$. A full description of the algorithm is presented in ref. [50].

If one now wants to determine the final laser intensity on target, further deductions have to be considered: First, the target is (contrarily to the microscope objective) irradiated under 45° , which gives an additional factor of $1/\sqrt{2}$. Secondly, the detected focus area considers only the FWHM intensity and the ratio between these intensities yields a factor of 0.33. Thirdly, the parabola is shielded from ablation with a Debris filter, which further reduces the intensity to about 90%. Together with these three additional losses, the initially stated $E = 0.8$ J, $\tau = 80$ fs and $A = 5 \mu\text{m}^2$ amount to a final maximum *intensity on target* of $I = (4.1 \pm 0.3) \times 10^{19}$ W/cm². After this detailed description of the components, the laser system shall henceforth be treated as a unit, that is, simply as a source of strong laser pulses.

3.1.2 Target chamber

Summary: The target is located at the center of a round steel chamber. The chamber is kept under a vacuum of 10^{-5} mbar.

The target chamber is the nexus between laser and particle physics and thus the heart of the setup. It is made of stainless steel and has a round shape with a diameter of 50 cm. It possess

¹The prepulse shaping unit displayed in Fig. 3.1 is inactive for the current experiment.

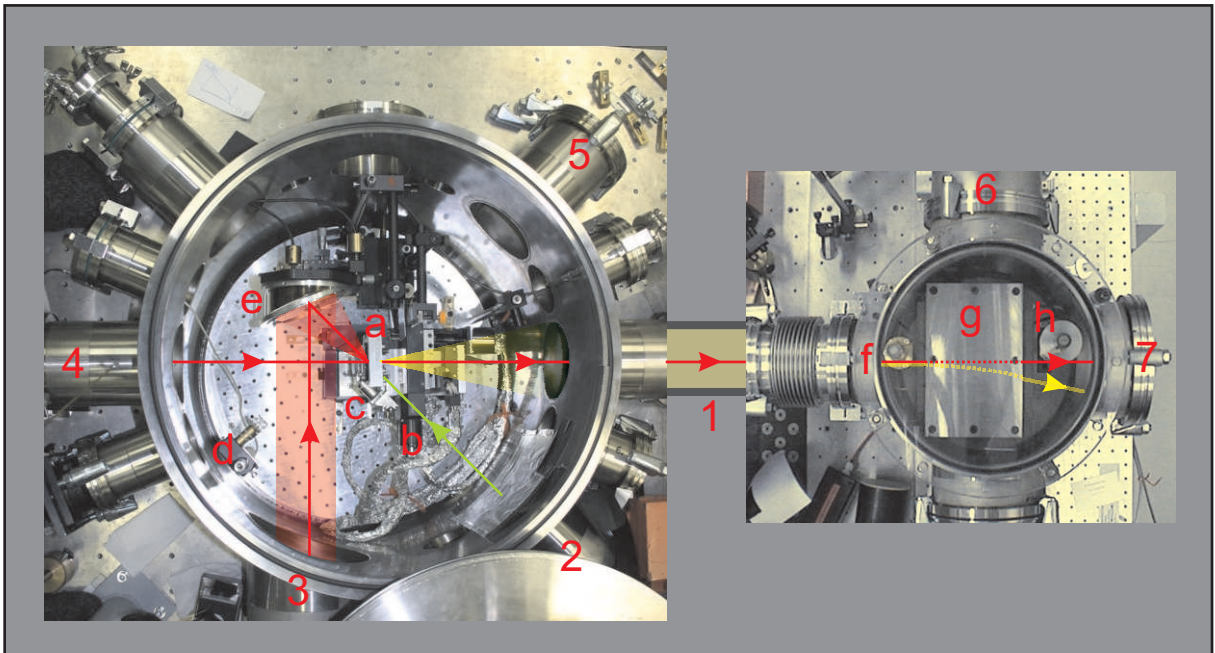


Figure 3.2: Target and detection chamber from above. The yellow line represents the proton beam propagation, the red lines show the optical paths of two alignment HeNe lasers and the green line marks the Nd:YAG incidence from the dot observation (cf. below). *Chamber components and ports:* a) target, b) $xyz\Theta$ -translation and -rotation stages, c) microscope objective for focus observation, d) LED, e) off-axis parabola, f) variable lead apertures, g) Thomson parabola, h) CR39 mount. 1) connection tube between target and detection chamber, 2) dot observation (cf. section 3.1.6), 3) beamline, 4) front side detection chamber (inactive), 5) focus observation, 6) turbomolecular pump and power supply, 7) MCP observation.

several ports, which are located around the whole circumference in intervals of 22.5° mostly (Fig. 3.2). The laser system is connected to the target chamber with an evacuated beamline, whereas the target chamber can be detached from the beamline with a mechanical shutter so that a partial airing becomes possible. For that reason, the chamber is also pumped by a separate set of vacuum pumps, which generate a pre-vacuum of 10^{-2} mbar (rotary vane pump) and a final vacuum of 10^{-5} mbar (turbomolecular pump). A second, smaller chamber hosting the beam imaging system is attached to target chamber at a sideport and shall be described in a later section.

The chamber is interspersed with the beam paths of several alignment HeNe-lasers (red lines in Fig. 3.2). A ring of LED's sufficiently resistant to vacuum serves as chamber illumination. Furthermore, the target chamber hosts the off-axis gold parabola already mentioned in the previous section. In the centre of the chamber, the target frame is mounted on *three translation stages and a rotation stage*, which enables an accurate 3d-positioning of the target within the laser focus (cf. section 3.1.4). The translation axes shall henceforth be defined as follows: The target plane represents the *xy*-plane, where x designates the horizontal and y the vertical direction. The *z*-axis is (different from the theory chapter) given by the target-normal direction. In the following section, the targets applied for the generation of monoenergetic protons shall now be characterized.

3.1.3 Production of microstructured targets

Summary: Microstructured double layer targets were fabricated with the help of spin coating and laser ablation. The targets consist of a $5\ \mu\text{m}$ Titanium foil carrying polymer dots of $20 \times 20 \times 0.5\ \mu\text{m}^3$ dimension with $50\ \mu\text{m}$ separation. The separation between consecutive laser shots is about 1 mm.

As demonstrated in section 2.2.4, the generation of monoenergetic protons strongly depends on the confinement of the proton source to a region of about the laser focal size. The targets for the experiments under discussion were manufactured in two steps. First, a commercial thin metal foil (Goodfellow) was coated with a polymer layer (Polymethyl methacrylate, short "PMMA") via *spin coating*. This is the conventional procedure for the production of double layer targets at the JETI group. Organic materials like polymers contain large amounts of Hydrogen and therefore represent an appropriate proton source. For spin coating, the target is rotated so fast that a well-defined drop of PMMA will spread evenly from the centre due to the centripetal force. The process was carried out by the lithography group of the Institute of Applied Physics, Jena.

In the second step of the fabrication procedure, the actual dots are being "carved out" from the even PMMA surface. This *microstructuring* was done via laser ablation at the high intensity kHz-laser system of the Institute of Optics and Quantum Electronics, Jena,

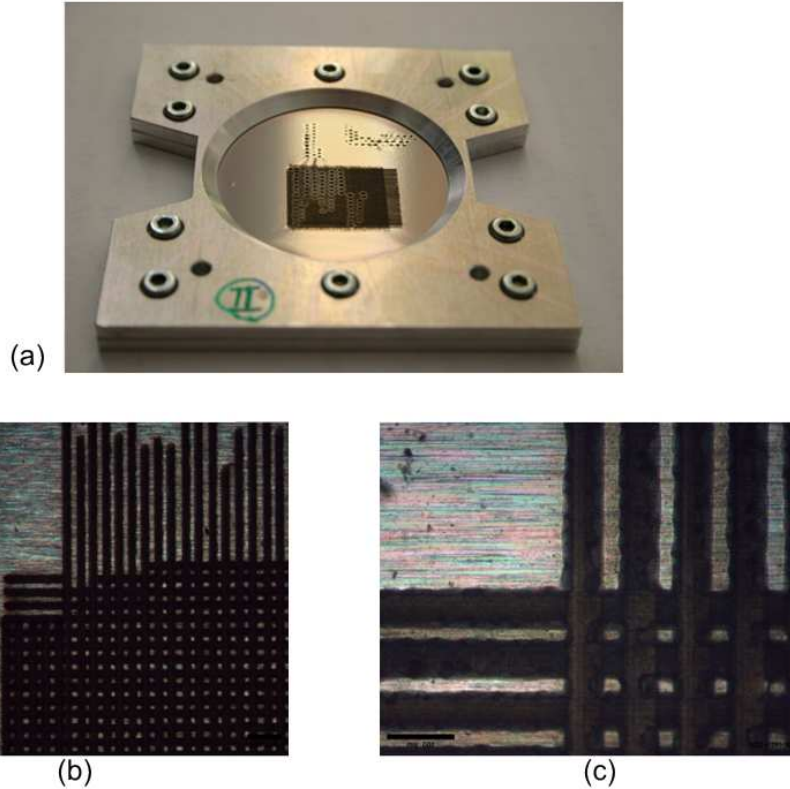


Figure 3.3: a) Microstructured thin foil target in Aluminium frame. The even surface shows a squared microstructured area and several holes from laser exposure. The frame is designed such that stretching, coating, structuring and experimental implementation of the target can be done without re-opening it again. The bottom pictures show magnifications of the microstructured area with 200x (b) and 500x (c) magnification. The polymer layer shows a red glance resulting from the Rhodamine component added to the solution (cf. section 3.1.4).

and represented a major engineering challenge.² From the variety of available targets, the structuring of $5\ \mu\text{m}$ Titanium foil coated with $0.5\ \mu\text{m}$ of PMMA yielded the best results (Fig. 3.3).

In this first experimental campaign, a dot size of $20 \times 20\ \mu\text{m}^2$ was achieved (Fig. 3.4), which is larger than the demanded focal spot size ($\sim 5\ \mu\text{m}^2$). However, it has been discussed in section 2.2.3 that the region of proton emission is typically as large as $80\ \mu\text{m}$ in diameter and one can therefore justifiably expect the dots to experience an almost homogeneous field. The separation between two dots is $50\ \mu\text{m}$. The fabrication process is currently being improved and will provide smaller dots for future experiments (cf. Fig. 5.1).

As can be seen from Fig. (3.4), the resulting holes in the target foils are much bigger than the microstructure, which can be ascribed to thermal effects. The holes typically attain

²For such thin targets, a most careful ablation is required; otherwise, the target will suffer from heat deposition and obtain unacceptable deformations or even damage.

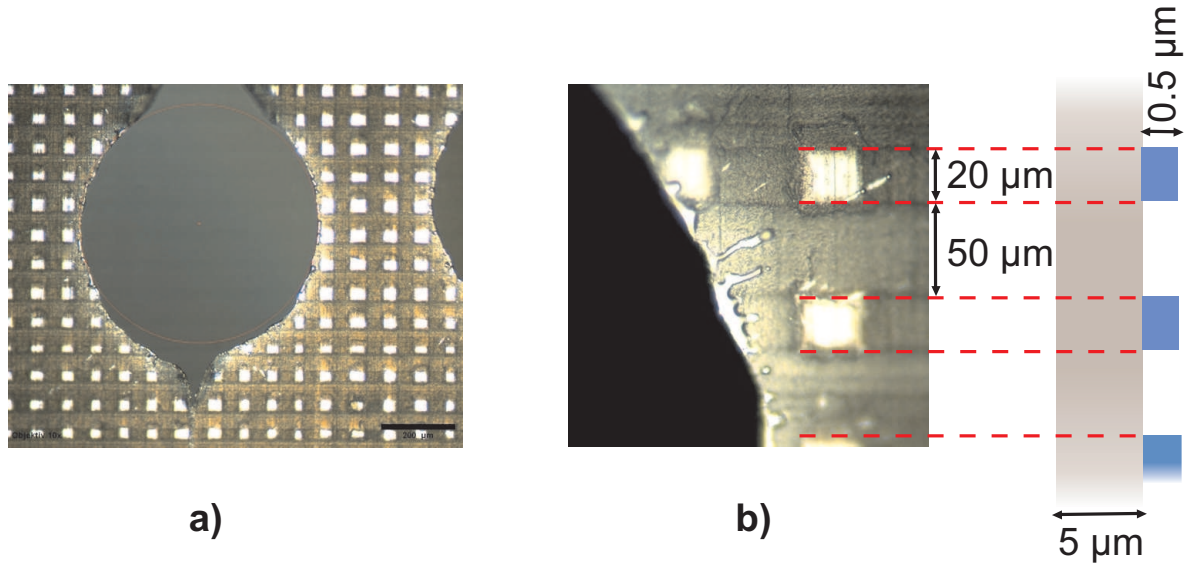


Figure 3.4: Microstructured target surface. A $5\ \mu\text{m}$ Titanium foil carries polymer dots of $0.5\ \mu\text{m}$ thickness, $20 \times 20\ \mu\text{m}^2$ extent and $50\ \mu\text{m}$ separation. The pictures show the foil after laser irradiation under 100x (a) and 500x (b) magnification. Although the laser focus is comparable to the dot size, much bigger holes are created due to thermal interaction. The displayed hole attains a diameter of about $640\ \mu\text{m}$. The surrounding dots remain unaffected.

0.3 – 0.8 mm in diameter. With distance of 1 mm between consecutive laser shots, a target with roughly $15\ \text{cm}^2$ will thus provide space for more than 1000 shots.

3.1.4 Alignment of the target

Summary: The target can be placed exactly in focus by observing the accompanying bremsstrahlung dose. The Ti:Sa focus position is projected on the target back side with an overlapped Nd:YAG laser. The polymer dots contain a dye component (Rhodamine 6G) and can be positioned in the Nd:YAG focus by observing their fluorescence emission.

z-positioning

For laser-matter experiments at ultrahigh intensities it is crucial to determine the focus position very accurately.³ A first crude positioning of the target within the focus can be achieved by minimizing the visible beamline HeNe focus with the help of a camera. The beamline HeNe has been co-aligned with Ti:Sa path utilizing several far-field monitors. For a fine adjustment one has to employ the Ti:Sa laser itself, which can be done with the following procedure: When moving the target in z -direction through the focus, a *corresponding peak-shaped dose behaviour* is observable (Fig. 3.5). This peak can be explained by the higher number of elec-

³“Accurately” means here within the Rayleigh length of $24\ \mu\text{m}$.

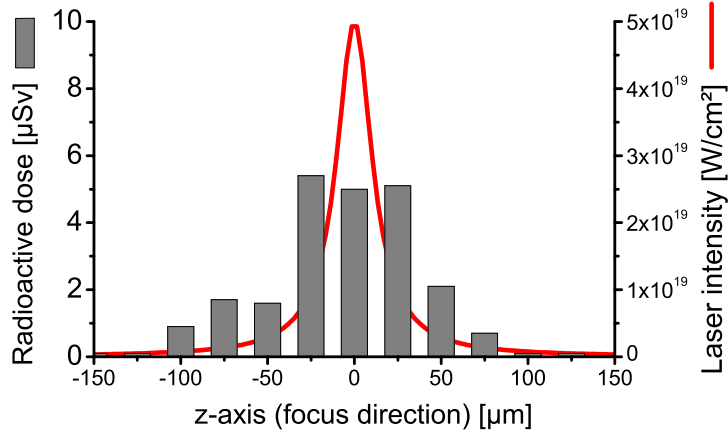


Figure 3.5: Correlation between the z -position of the target, the laser intensity and the detected radioactive dose. The amount of bremsstrahlung created by hot electrons in the target chamber drops significantly outside the Rayleigh length ($\approx 24 \mu\text{m}$).

trons created at the focus intensity, which results in an increased production of bremsstrahlung in the vicinity. Thus, a dose meter facing the target rear side from outside the chamber can serve as a measure for the target’s z -position.

This peak behaviour is reproduced consistently, and hence the centre of the peak is defined as $z = 0$ (focus position). All experimental results support this convention. The plateau in the middle of the curve (Fig. 3.5) is due to saturation effects of the integrating dose meter.

Fluorescence observation and alignment of the dots

The success of the experiment strongly depends on the exact positioning of the dot exactly *opposite the laser focus*. In practice, this means to correlate something located on the front side of the target, i.e. the Ti:Sa focus, with something only visible from the back side, i.e. the dots. For this problem, the following solution has been developed: First, a tiny hole ($\approx 50 \mu\text{m}$) is created in the target with a single weakened Ti:Sa shot ($I_{\text{weak}} \approx 0.1 I_{\text{max}}$). The generated hole can be assumed to be centred around the Ti:Sa focus. A fixed camera observation setup located outside the chamber serves as a reference coordinate system and the focus position can hence be simply marked on the monitor. Now, if the dots were visible with the camera only, they could have been simply brought into this marked position on the screen.

However, even a strong illumination proves unsatisfactory for a clear distinction of the dots from their vicinity (Fig. 3.9). Therefore, a second laser beam has been focussed onto the target exactly opposite to the Ti:Sa incidence, that is from the “straight-through” direction (Fig. 3.6). The foci of the two lasers are brought in *spatial coincidence* by adjusting the second

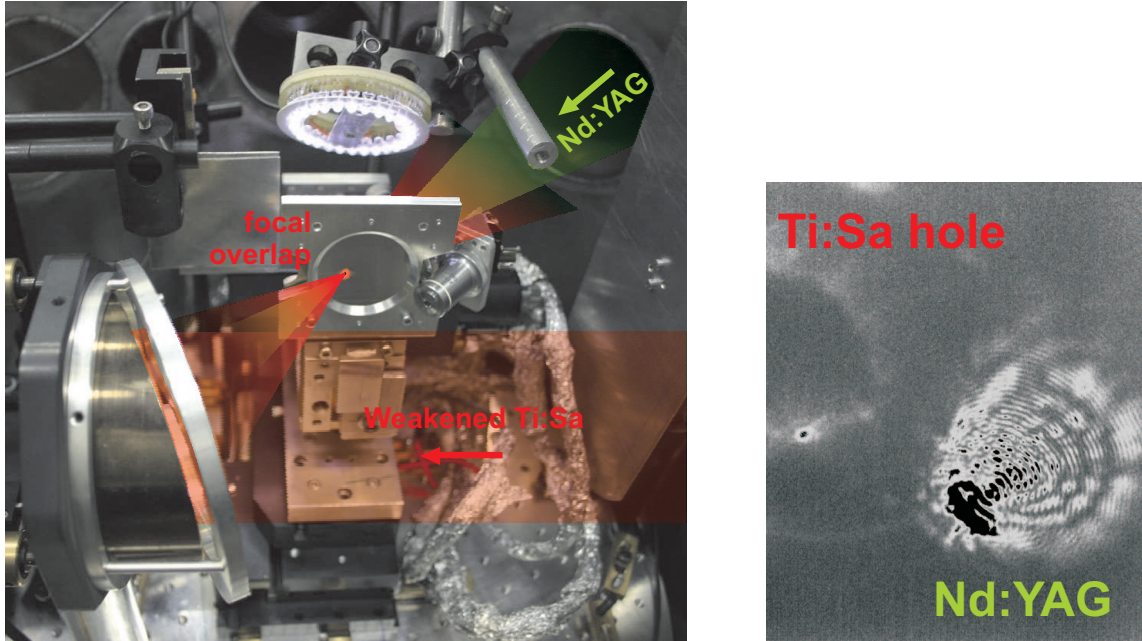


Figure 3.6: a) Focal overlap of Ti:Sa beam with Nd:YAG alignment laser. A small hole ($\approx 50 \mu\text{m}$) is generated with an attenuated JETI shot, which is centered around the focus position. The focus of a SHG Nd:YAG laser is guided through the hole exactly with its focal waist and may thus serve as a reference mark on the target back side. b) Screenshot. The overlap has not been established yet. The right half of the created hole is visible at the left hand side of the picture. The surface reflections of the still displaced Nd:YAG focus (accompanied by aberration rings) are shown on the right hand side.

laser through the little hole in the target exactly at its focal waist. With such an alignment, one has established a pointer that serves as reference for the Ti:Sa focus position on the back side.

Consequently, the dots need to be brought into the centre of the alignment laser focus. For this purpose, a few drops of the fluorescence dye Rhodamine 6G were added to the liquid polymer solution. The alignment laser, a weakened SHG Nd:YAG emitting at 532 nm, excites fluorescence transitions in the dye, which in turn emits at around $\approx 600 \text{ nm}$ (Fig. 3.7 & 3.8). The Nd:YAG was focussed to about $\approx 100 \mu\text{m}$ in diameter. With this size, the dots can be clearly observed moving in and out of the focal spot when translating the target in x - or y -direction (Fig. 3.9). A exact positioning of the dots can thus be achieved easily.

This method covers the trickiest part of the experiment and shall therefore emphasized in its importance. With the little detour of applying of an additional reference laser that connects the microstructured target back side to incidence of the main pulse on the front side and simultaneously serves as a fluorescence light source, one has established a convenient and reliable method for a precise dot alignment.

The fluorescence illumination and observation were carried with one chamber port only

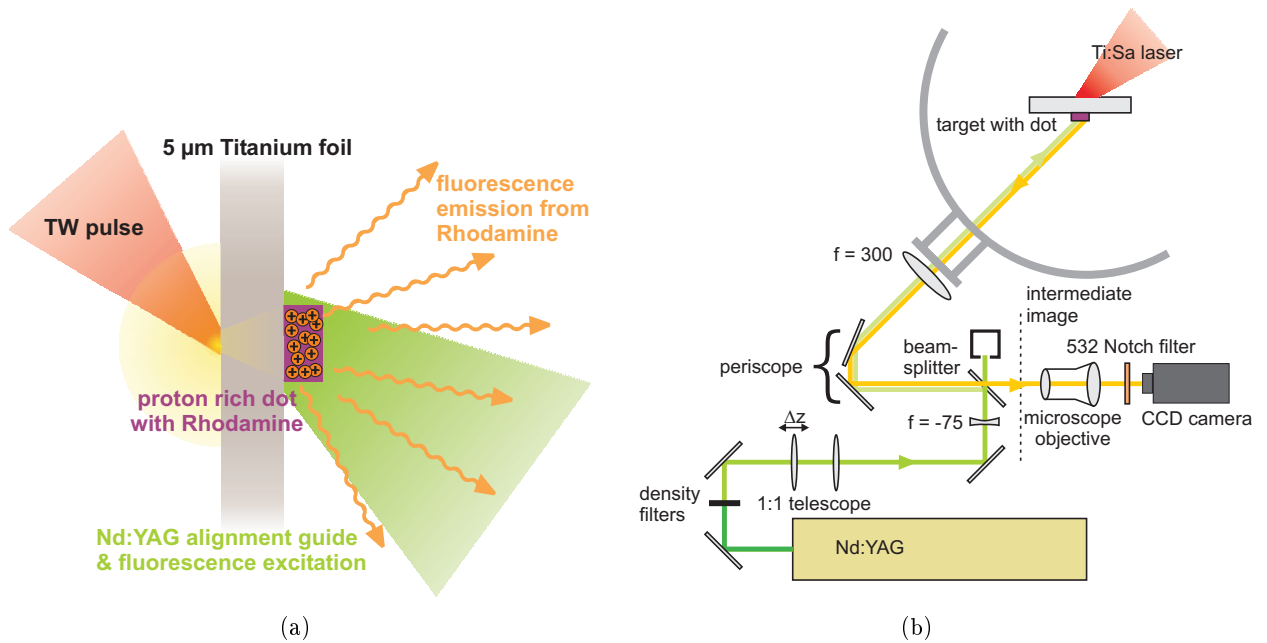


Figure 3.7: a) Principle of the fluorescence observation of the polymer dots. A proton rich dot of the dimension $20 \times 20 \times 0.5 \mu\text{m}^3$ is interspersed with Rhodamine 6G. When illuminated with the green light of a frequency doubled YAG (532 nm), the dye starts to emit fluorescence light around 600 nm and the dot can be observed with CCD detection setup. b) Scheme of the dot observation setup. The microstructured target is illuminated and observed with the same optical path. A microscope objective images the fluorescing dots onto a CCD chip with a magnification of about 33x.

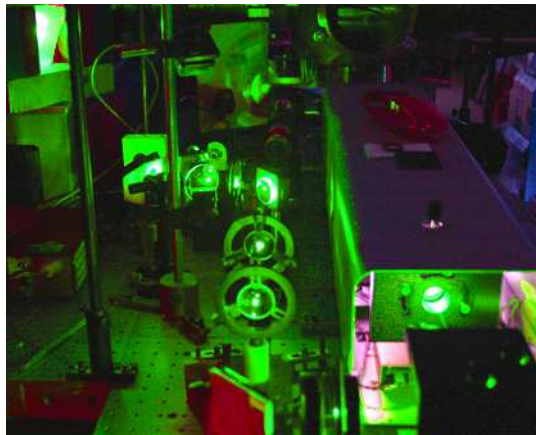


Figure 3.8: Picture of the setup from Fig. (3.7b), view from the left. The green laser beam can be observed leaving the SURELITE case (right bottom), passing the 1:1 telescope, the beamsplitter and the periscope (center) and finally entering the chamber through a lead wall (left top). Behind the beamsplitter, the microscope objective and the CCD camera are visible.

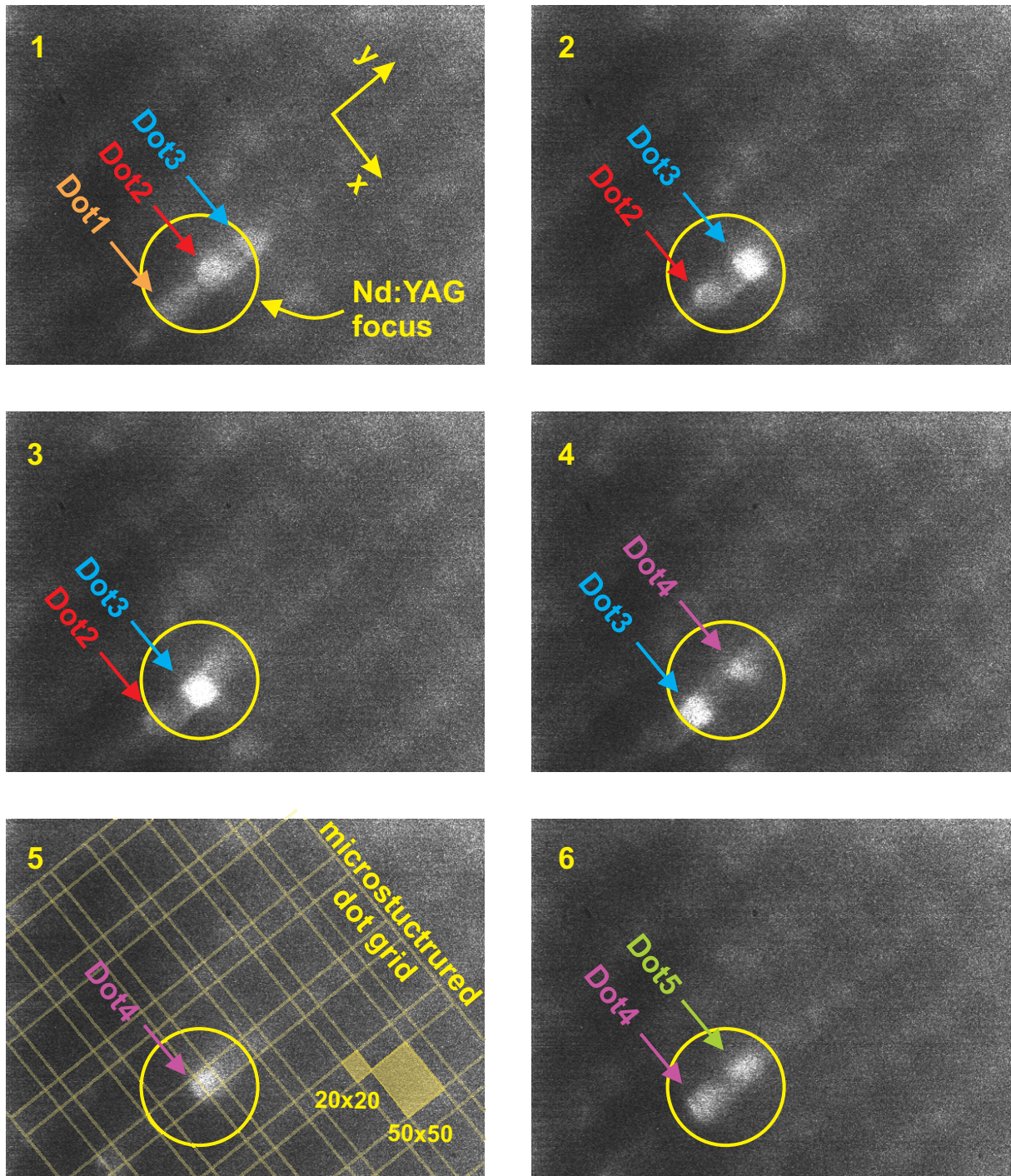


Figure 3.9: Screenshot series of several consecutive dots moving through the YAG focus. The target is being translated in y -direction. The fluorescing dots can be clearly observed moving in and out the illuminated region. A grid has been inserted in subfigure #5 according to the extent and separation of the dots: one can guess the existence of the pattern from the alternating texture brightness.

(Fig. 3.7 b). This principle is known from the field of fluorescence microscopy and micro-medical laser tools (i.e. laser scissors and tweezers), where the same optical path is used for target observation, fluorescence excitation and emission within the target, as well as the implementation of the medically invasive laser beam(s). Such multiple schemes can be realized with the help of polarizing or frequency selective beamsplitter optics.

On its way, the laser light passes a 1:1 telescope that allows the focussing of the YAG on the target: if the focal overlap of the two lenses is slightly deadjusted, the beam will continue to propagate with a slight con- or divergence, which will shift any subsequent focus on the optical path accordingly. This is especially important when trying to fit the YAG focus through the Ti:Sa-generated hole. The corresponding xy -steering on the target plane can be done with any mirror on the way.

The main collimation is done with a combination of two lenses, a concave one ($f = -75$ mm) behind the telescope and a large convex one ($f = 300$ mm) directly in front of the sideport before entering the vacuum. The lenses are placed at a distance of about 85 cm from each other. The second lens determines the numerical aperture of the whole setup, which is important when considering the inverse path for dot observation.

When arriving at the target, the pulse has been attenuated to about 0.36% of its original intensity by a beamsplitter ($T = 0.04$, T being the transmission), a density filter ($T = 0.1$) and additional losses from mirrors and reflections ($T \approx 0.9$). This attenuation is necessary in order to avoid damage on the target. From the NdYAG specifications ($E_{\text{pulse}} \approx 200$ mJ within $\tau_{\text{pulse}} \approx 5$ ns), one can estimate the intensity on the target available for fluorescence excitation:

$$I_{\text{excite}} \approx \frac{0.0036 \cdot 0.2 \text{ J}}{\pi \cdot (50 \times 10^{-6} \text{ m})^2 \cdot 5 \times 10^{-9} \text{ s}} \quad (3.2)$$

$$\approx 2 \times 10^9 \frac{\text{W}}{\text{cm}^2} . \quad (3.3)$$

The orange fluorescence light is emitted isotropically and collected in a solid angle of $\Omega_{\text{lens}} = 17$ mSr (numerical aperture of $NA = 0.075$) with the same optical path. The the aperture lens creates an intermediate image closely behind the beam splitter, which is being imaged onto a CCD chip with a microscope objective. The final magnification amounts to 33x. In order to screen the camera from YAG reflections, a 532 nm Notch filter has been attached to the camera tube.

3.1.5 Reduction of parasitic protons

Summary: The impact of parasitic protons from the contamination layer is minimized via laser ablation.

The described observation setup also fulfills another purpose. It was observed that the intensity of the weakened Nd:YAG beam still suffices to ablate material from the target back side. After a few minutes of permanent exposure, the fluorescence emission of the dots vanishes, which indicates that they have fully disintegrated. Considering the applied laser parameters (fluence $\Phi = 10^3 \text{ mJ/cm}^2$ at $\lambda = 532 \text{ nm}$), this agrees with measurements on laser ablation rates [73, 74]. However, since for the aiming procedure the dots never need to be illuminated for more than half a minute, one can benefit from this side-effect.

It has been explained earlier that the whole target is subject to a contamination layer (cf. section 2.2.3). Thus, even though the dot source should exceed the layer in proton yield, the impact of such *parasitic protons* will weaken the confined acceleration and add an exponential background to the monoenergetic feature. The described ablation avoids of this problem: The Nd:YAG fluence easily suffices to remove the contamination layer from the focal region. For the applied vacuum (10^{-5} mbar), the recovery time of adhesive quasi-monolayers can be estimated by the particle impact rate on a surface [75]

$$R = \frac{p}{(3m k_B T)^{\frac{1}{2}}}, \quad (3.4)$$

which follows directly from kinetic gas theory. Here, p is the chamber pressure, m the mass of the adsorbed molecule and T the temperature. For $p = 10^{-5} \text{ mbar}$ and $T = 300 \text{ K}$, the impact rate for Hydrocabons ($m \approx 14 \times 1.7 \times 10^{-27} \text{ kg}$) attains $R = 6 \times 10^{15} \text{ cm}^{-2} \text{ s}^{-1}$. An ablated area of $A_{\text{Nd:YAG}} \approx \pi(50 \mu\text{m})^2$ will hence need about 6 seconds in order to recover a 12 \AA contamination layer (cf. section 2.2.3 and ref. [39]), which is well above the time between two consecutive ablation shots (100 ms). The observed ablation due to the Nd:YAG irradiation can thus be expected to limit the influence of parasitic protons considerably. A quantification of this effect will be part of future experiments.

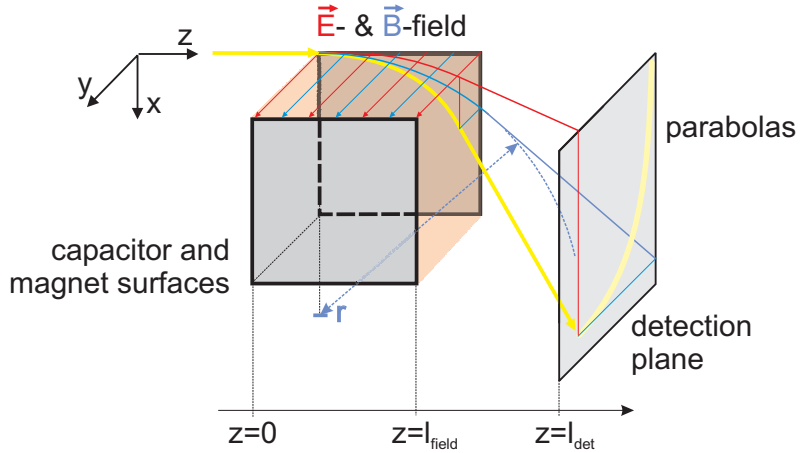


Figure 3.10: Deflection scheme of the Thomson parabola (top view). The ion track is given by the yellow line. Magnetic deflection (blue) and electric deflection (red) are displayed as projections separately.

3.1.6 Particle beam analysis I: dispersion via Thomson Parabola

Summary: A Thomson spectrometer is used to disperse the incident particles according to their kinetic energy and q/m -ratio. The deflection function $\Delta x(E_{\text{kin}})$ has been inverted numerically to $E_{\text{kin}}(\Delta x)$ so that the initial energy can be derived from the impact position.

A Thomson parabola is based upon the superposition of an electric and a magnetic field (Fig. 3.10). Here, the magnetic field is given by two permanent magnets of $B_{\Delta x} = 525 \pm 10$ mT. The magnets are hosted in a yoke, which suppresses the fringing fields.⁴ The electric field is generated by a 10×10 cm² capacitor with a field strength of $E = 2.7$ kV/cm. For a Thomson spectrometer, the E - and the B -field are parallel. Therefore, the capacitor plates were attached to the magnet surfaces (Fig 3.11).

The beam has to enter the parabola in a strongly collimated way. For the present setup this has been achieved by a lead aperture of 5 mm diameter, which could be reduced further by a subsequent set of pinholes to either 3 mm, 1 mm or 0.3 mm (Fig 3.11). The aperture defines the energy resolution of the recorded spectra (cf. 3.3.2) and should generally be as chosen as small as possible.

In the following, a relation between the deflection and the particle parameters shall be derived. It shall be noted that all calculations here are presented for the non-relativistic case. This agrees well with the achieved proton energies of $E_{\text{kin}} < 5$ MeV, as can be seen from the estimation of the relativistic correction factor

$$E_{\text{kin}} = \frac{E_{\text{kin}}}{m_p c^2} + 1 \approx 1.005, \quad (3.5)$$

⁴Both the confinement and the magnitude of the B -field was characterized with a Hall detector [62].

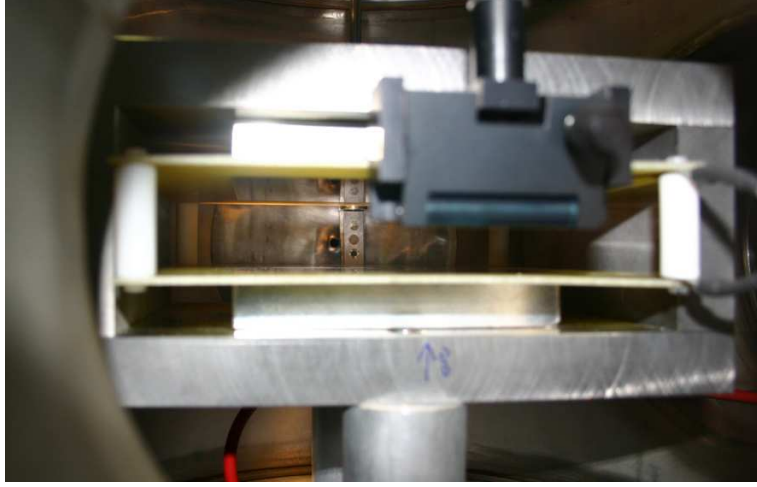


Figure 3.11: Inside view of the detection chamber from the detection plane. The chamber hosts a solid metal yoke, which carries the two magnets (smaller silver blocks) and the capacitor (yellow plastic plates). In the background, the lead aperture and a selection of three variable pinholes are visible. The aperture represents the connection to the target chamber. The foreground shows a CR39 mount.

where m_p is the proton rest mass of $1 \text{ GeV}/c^2$.

Under the impact of a magnetic field a charged particle is forced onto an orbit (Fig. 3.10), the radius of which can be determined from the equilibrium between the Lorentz force and the centripetal force

$$\vec{F}_{\text{centr}} = \frac{m \vec{v}^2}{r} \cdot \vec{e}_r \equiv q(\vec{v} \times \vec{B}) = \vec{F}_L \quad (3.6)$$

$$\Rightarrow r = \frac{mv}{qB}, \quad (3.7)$$

m being the unknown ion mass. Consequently, the B -field deflection x can be obtained from the circular ion motion, acknowledging that the centre of the circle is located at $x = +r$ and the ion enters the field at $x = 0$. If the particle is fast enough to exit the parabola at the back, i.e. $r > l_{\text{field}}$, the deflection at the exit point $z = l_{\text{field}}$ yields

$$x(l_{\text{field}}) = r - \sqrt{r^2 - l_{\text{field}}^2} \quad (3.8)$$

with r as given above.

For the deflection by the E -field, one can refer to the equation:

$$m\ddot{y} = F_{\text{el}} = qE, \quad (3.9)$$

whereas the time derivative can be transformed into a spatial one under the assumption that

v_z remains constant ($v_z \equiv v$):

$$\frac{d^2y(t)}{dt^2} \approx \frac{d^2y(t)}{dz(t)^2} \cdot \frac{dz(t)}{dt} = v_z^2 \frac{d^2y}{dz^2}. \quad (3.10)$$

After a double z -integration of equation (3.9), one obtains for the exit point l_{field}

$$y(l_{\text{field}}) = \frac{qE}{2mv^2} l_{\text{field}}^2. \quad (3.11)$$

v_z can not be taken as *ad hoc* constant, because it has to obey the circular motion with respect to v_x . However, if the B -field deflections are sufficiently small, the effect on v_y can be neglected. For a 3 MeV proton the orbit radius can be roughly 50 cm; in comparison to the field dimensions of 10 cm, this means an interruption of the circular motion at a point when $v_z(0) - v_z(l_{\text{field}}) \approx 0.9 |\vec{v}|$.⁵

After the particles left the spectrometer, they continue to propagate with constant velocity until they arrive at the detection screen (Fig. 3.10). This leads to an additional linear term in the deflection, so that for a given distance $d = l_{\text{det}} - l_{\text{field}}$ between the spectrometer and the screen one finally obtains

$$\begin{aligned} \Delta x(v, l_{\text{det}}) &= x(l_{\text{field}}) + v_x(l_{\text{field}}) \cdot t_{\text{prop}} \\ &= r - \sqrt{r^2 - l_{\text{field}}^2} \left(1 - \frac{l_{\text{field}}(l_{\text{det}} - l_{\text{field}})}{r^2 - l_{\text{field}}^2} \right) \end{aligned} \quad (3.12)$$

$$\begin{aligned} \Delta y(v, l_{\text{det}}) &= y(l_{\text{field}}) + v_y(l_{\text{field}}) \cdot t_{\text{prop}} \\ &= \frac{qEl_{\text{field}}}{mv^2} \left(\frac{1}{2}l_{\text{field}} + 4\pi r \frac{l_{\text{det}} - l_{\text{field}}}{\sqrt{r^2 - l_{\text{field}}^2}} \right), \end{aligned} \quad (3.13)$$

where v can be replaced by $\frac{2E_{\text{kin}}}{m}$. A full derivation of equations (3.12) and (3.13) was given by Jäckel [62].

One has now two relations at hand connecting the particle velocity, i.e. its kinetic energy, to a spatial deflection. Since only one of them is required to determine the particle energy from impact position, the second one can be used for the determination of the q/m -ratio. For the given E - and B -field values, the B -field deflection $x(l_{\text{field}})$ is the larger one and thus has been preferred for the energy analysis.

The deflection functions can not be inverted analytically with respect to $E_{\text{kin}} = \frac{1}{2}mv^2 = f(\Delta x, \Delta y)$. If one wants to derive the initial kinetic energy of a particle from its deflection,

⁵It shall be noted that although the B -field solution does not consider the $|\vec{v}|$ -increase from the E -acceleration, it still pays respect to the entanglement of v_x and v_z due to the circular motion, which improves the energy accuracy. If this dependence is also dropped and $|\vec{v}|$ is treated strictly as v_z , one arrives at $x(z) = \frac{qE}{mv_z} z^2$ and finds the actual Thomson “parabolas” with $x \sim y^2$.

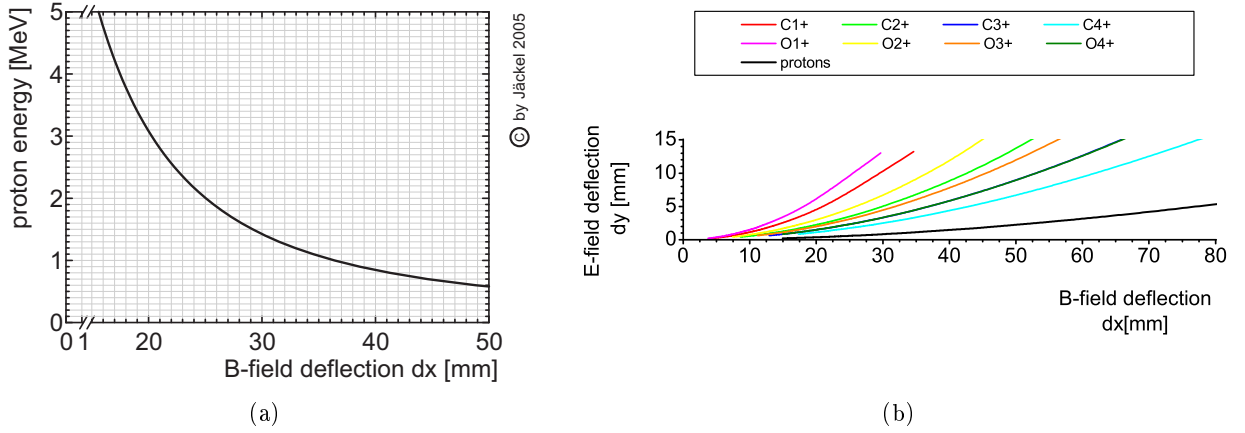


Figure 3.12: a) Energy-deflectionfunction. The initial kinetic energy can be determined by the numerical inversion of equation (3.12). b) Theoretical ion tracks. The expected parabola deflections can be calculated for different q/m ratios.

one has to put forward the respective deflection function $\Delta x(E_{\text{kin}})|_{E,B,q,m}$ for each given set of parameters (E, B, q, m) and invert it numerically. In practice, this has been done with a 3rd order exponential fit, which yields excellent agreement. In Fig. 3.12 both the obtained proton energy-deflection-function and a set of theoretically calculated ion parabolas are shown for the field parameters $B = 525 \text{ mT}$ and $E = 2.7 \text{ kV/cm}$.

3.1.7 Particle beam analysis II: detection

Summary: The experiment features two detection mechanisms, which can be used in support of each other. CR39 track detection plastics deliver absolute information about impact numbers, but require a time-consuming evaluation. A Multi Channel Plate allows for the online observation of the experiment, but has to be calibrated carefully in order to obtain absolute spectra.

Track detection plastics - CR39

The setup contains two detection mechanism, both bearing advantages and disadvantages. The first mechanism is given by so-called *CR39 track detection plastics* (Track Analysis Systems Ltd.), which are made of a transparent thermoset resin [76]. In the experiment, CR39 pieces of typically $90 \times 50 \text{ mm}^2$ size are attached to a frame behind the Thomson spectrometer (3.2). When the fast particles penetrate the CR39 plate, they will be stopped according to Bragg's absorption law (cf. section 4.2.1) and leave behind a trace of structural damage on their path. When etched in NaOH solution, the CR39 will expell the damaged material and form little craters so that the collected ion beams appear as visible traces on the plate, which can be

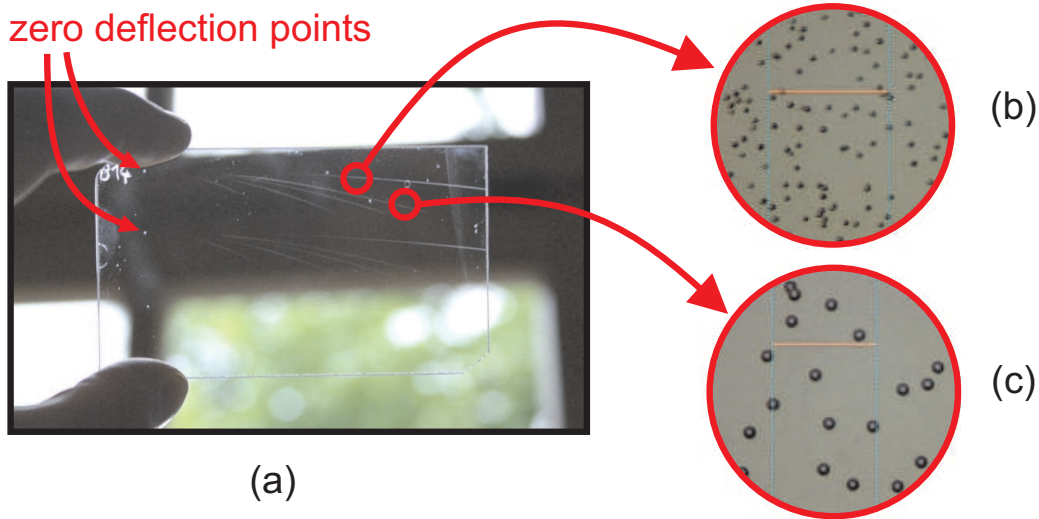


Figure 3.13: a) Irradiated and processed piece of CR39. a) Several ion traces are visible in addition to the strong proton track (long top trace). The obtained parabolas are in excellent agreement with the theoretical predictions (Fig. 3.12). Under a microscope with 50x magnification, the traces can be analyzed with single impact resolution, which is shown in (b) for the case of protons and in (c) for Carbon ions.

evaluated further under a microscope (Fig. 3.13). Both the concentration of the solution and the etching time affect the visible outcome substantially with respect to depth and extent of the corrosion. For our purpose, a two hour bath in 6M NaOH solution at 85°C yielded optimum results.

The CR39 technique can be used for energy resolution also in a different way. Since the passing of a metal foil with certain thickness requires a minimum kinetic energy, one can collect information about the spatial energy distribution of the beam by covering a piece of CR39 with metal foil layers in a suitable way. Fig. 3.14 shows such a “pie filter” piece, which was mounted directly behind the target, where it could be moved in and out the proton beam.

The clear advantage of CR39 over any other method is the 1:1 mapping between the recorded images and real ion flux - *each pit corresponds to a single ion!* The CR39 thus delivers unequivocal information about the particle number. On the other hand, the handling of CR39 is rather awkward and slow. A maximum of 6 spectra can be recorded with one plate before it has to be replaced, which includes an airing of the chamber. Together with the two hours processing time this slows down the experiment considerably. Therefore, a complementary method shall be introduced.

Online observation - MCP

The second detector consists of a *Multi Channel Plate (MCP)* (Colutron Research Corp.), which is located in the front port of the detection chamber (Fig. 3.2). Its detection sur-

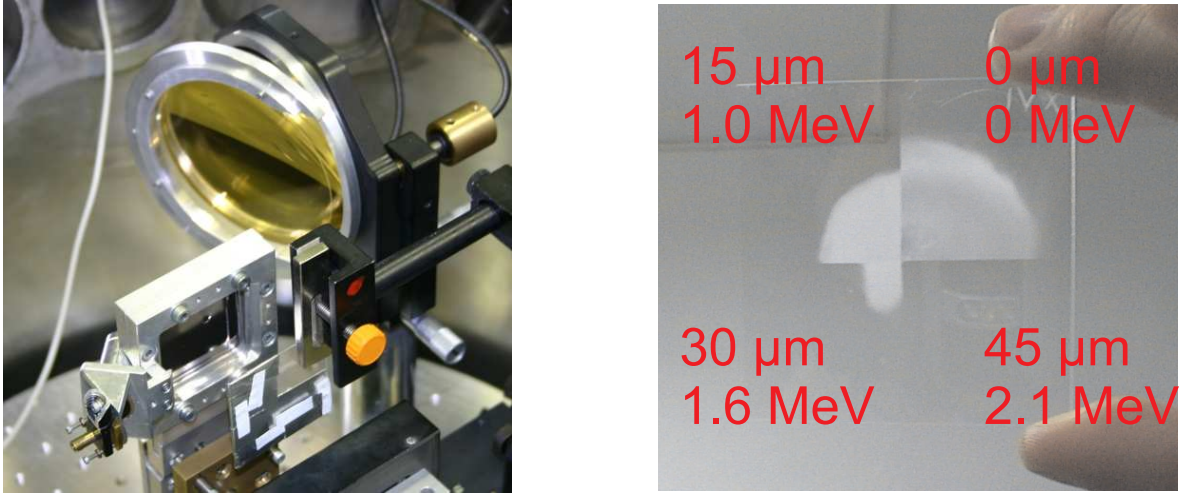


Figure 3.14: a) A CR39 piece covered with Aluminium of 3 different thicknesses is visible in at the bottom. Different foil thicknesses correspond to different minimum energies and deliver information about the angle of emission. The piece is mounted directly behind the target for spatial emission analysis. b) Picture of the irradiated plastic. The foil thickness and the required minimum energy are noted for every sector. The emission can be seen to happen within energy cones.

face carries an *array of small, oblique lead channels* in which the incident ions will beat out electrons. The electrons are accelerated along the channels by an external voltage of +2 kV, thereby initiating multiple secondary electrons processes, and (after a second acceleration to a maximum of +5kV), arrive at a phosphor screen. The resulting light is collected and guided out of the vacuum by a fiber taper, where it can be observed with a CCD camera. The spatial resolution of the MCP is limited to 300 μm . For a more detailed review, refer to [62].

The striking advantage of using an MCP is the possibility of *online observation* - the CCD images can be evaluated with a computer immediately (Fig. 3.16). The average processing time is thus reduced from several hours to a few seconds, which allows for very flexible experiments. Furthermore, with an MCP large amounts of data can be acquired, which enables for the first time a statistical interpretation of the acceleration experiments. Without the online detection, none of the presented results could have been achieved within the restricted timeframe.

Although the time argument makes the MCP highly preferable over CR39, a number of disadvantage have to be considered, too. The MCP is a very *sensitive* instrument that has be kept under a constant vacuum of the order of $10^{-6} - 10^{-7}$ mbar. This high vacuum is achieved by differential pumping with a separate set of pumps, which retains the quality of the vacuum against the target chamber (10^{-5} mbar). When exposed to air, the MCP system takes several hours to be reactivated due to the necessary gradual voltage application. Another disadvantage is the comparably small size of the detection area (Fig. 3.17), which restricts the detection to a lower energy of about 0.85 MeV. Furthermore, the MCP delivers only relative

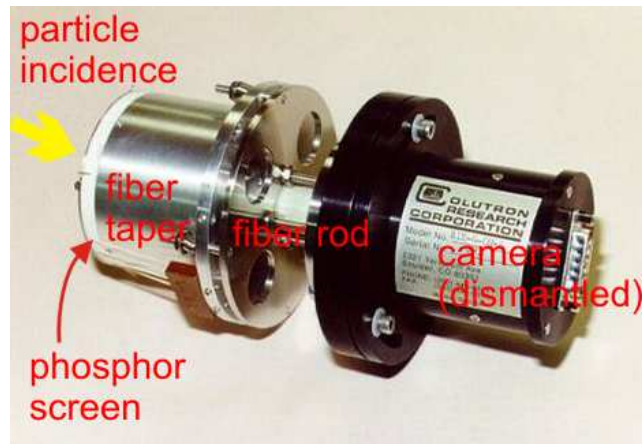


Figure 3.15: The unmounted Multi Channel Plate (MCP).



Figure 3.16: Typical parabolic tracks obtained from the MCP. Spectral information can be derived from camera counts vs. horizontal distance to the zero deflection point (bottom right corner).

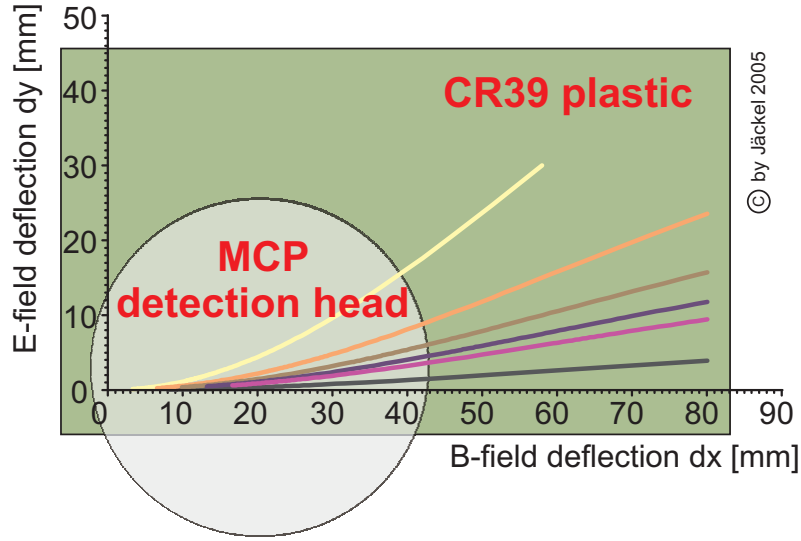


Figure 3.17: Comparison between the detection areas of the MCP and a CR39 plate.

spectra: each of the conversions from ions to electron, from electron to photons, and from photons to pixel charge is subject to a certain conversion efficiency and detection threshold, so that the obtained spectra have to be *carefully calibrated* against the corresponding, absolute CR39 spectra. (cf. section 3.2.2).

3.2 Analysis Techniques

3.2.1 Binning

Summary: The energy interval corresponding to the $100\ \mu\text{m}$ counting interval increases for higher energies. Therefore, the derived proton numbers are scaled to a constant energy width of $50\ \text{keV}$.

Both detection methods rely on the evaluation of impact densities. Therefore, the parabolic tracks are divided into intervals of constant width ($100\ \mu\text{m}$) and counted either with a computer routine (MCP) or by hand (CR39). However, due to the non-linearity of the deflection function (eq. 3.12), the corresponding energy intervals broaden with increasing energy, i.e. when approaching the zero deflection point. In order to obtain a spectrum "per constant energy width", one therefore has to define a fixed value for such a width beforehand and scale the counts at every x -position accordingly (Fig. 3.18).

A suitable energy width must cover the energy equivalent of $100\ \mu\text{m}$ up to the occurring maximum at E_{cutoff} , which in the present case is given by $\Delta E \approx 50\ \text{keV}$ for $E_{\text{cutoff}} \leq 4\ \text{MeV}$. The width should furthermore match the energy resolution given by the aperture in front of the Thomson spectrometer. If the energy resolution is worse than the separation of consecutive

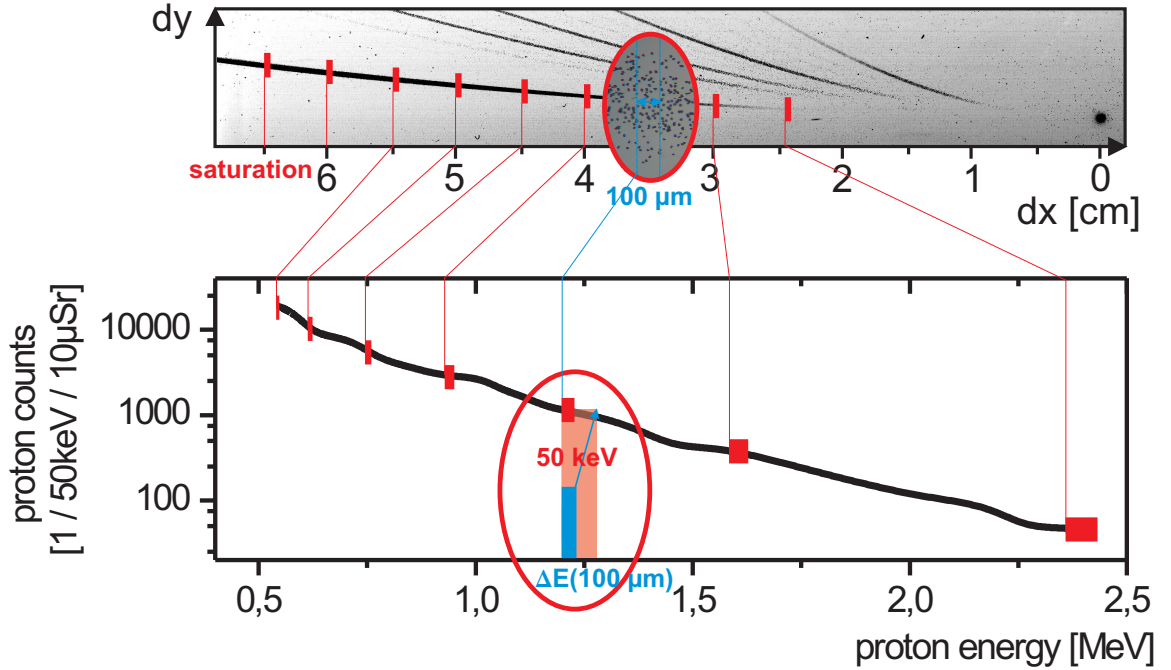


Figure 3.18: Conversion of parabola tracks into a spectrum and binning procedure. The upper graph shows a scanned CR39 track, the lower one the corresponding spectrum. For both CR39 and MCP pictures, intervals of constant spatial width ($100\ \mu\text{m}$) are counted with respect to impact densities. The B -field deflection Δx corresponds to the initial energy in a nonlinear way, which can be seen from the increasing spacing in the lower graph. Therefore, the spatial intervals correspond to energy intervals of different width, too. The derived impact densities thus have to be rescaled to a constant energy width ($50\ \text{keV}$), which resembles the occurring maximum at the cutoff energy. In the upper graph, the blue interval represents the $100\ \mu\text{m}$ counting width. This width can be seen to correspond to certain energy interval in the lower graph (blue bar), which is however smaller than the predefined value of $50\ \text{keV}$. Hence, it has been rescaled to $50\ \text{keV}$ (transparent red bar).

counting intervals, information about the height and width of monoenergetic spectral features can be blurred [62] which is, however, not the case for the current experiment. The projection of the 1 mm aperture onto the MCP surface amounts to 1.2 mm. Even at the minimum deflection, this interval remains comparable to the defined energy width of $\Delta E_{\text{res}} = 50 \text{ keV}$ and hence no information is being lost.

3.2.2 Calibration of the MCP against CR39

Summary: A comparison of MCP and CR39 spectra yields a scaling factor of 6 ± 1 between the two detection methods.

It has been mentioned in section 3.1.7 that the relative spectra from the MCP have to be calibrated against absolute CR39 numbers. The full calibration procedure is presented in Jäckel [62] and shall be outlined only briefly.

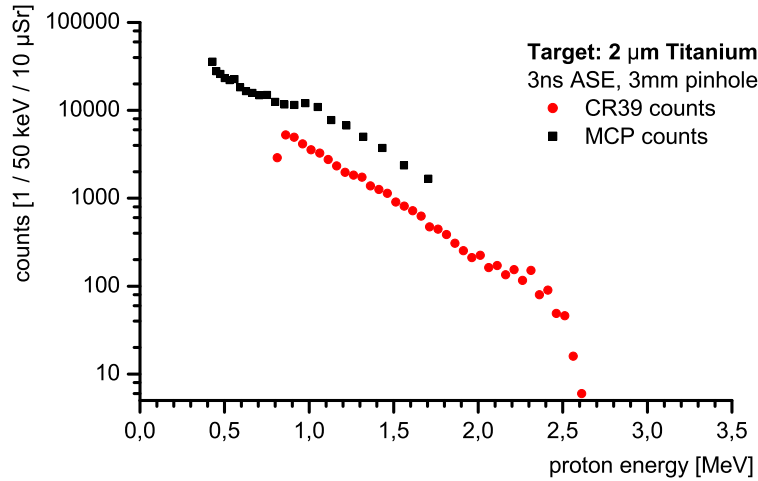


Figure 3.19: Calibration of the relative MCP spectra against absolute CR39 counts. The scaling factor between the CCD detected photons and the proton impacts on the CR39 assumes a constant value of 6 ± 1 .

Since one can change between both detection methods by simply moving the CR39 plates out of the beam (without breaking the vacuum), the calibration can be done in a straightforward way. A series of 10 consecutive shots is recorded with the MCP. If the resulting spectra are stable with respect to intensity, temperature, cutoff energy and ion distribution, the CR39 plate is moved in between the Thomson parabola and the MCP head and exposed to the proton beam.⁶ After that, another series of 5 comparative MCP shots is recorded in order to

⁶Typically, the CR39 were exposed to 10 consecutive shots, too. This averaging guarantees a certain robustness against statistical fluctuations.

affirm the unaltered beam conditions. Fig. 3.19 shows the comparison between an MCP and a CR39 spectrum. The two graphs are separated by a *constant factor of 6 ± 1* ; that is, one CCD count equals an average of 6 protons. With such a relation at hand, the application of the MCP is equally reliable as the track detection plates’.

3.3 Results

3.3.1 Overview over previous results from conventional targets & determination of the optimum experimental conditions

Summary: Ion beams (H^+ , C^{n+} , O^{n+}) with several hundred keV temperature and MeV cutoff energy can be readily produced at the JETI laser system. The optimum results were found for a $2\ \mu\text{m}$ Titanium foil and small prepulse. Double layer targets show a six times higher yield independently almost of the choice of the carrier foil.

A series of antecedent experiments has been carried out at the JETI system with both the MCP and CR39 [62]. The generated particle beams have been studied under a number of aspects, including the influence of the laser intensity, the prepulse and the incidence angle, as well as the target thickness and the material. All hitherto results are in *accordance with the TNSA explanation scheme* and comparable to those obtained by other groups (see for example [3, 28, 52, 59]). The current experiment can draw from this experience and determine the optimum conditions for the generation of monoenergetic proton beams.

At the JETI, the acceleration of various ion types has been observed. Besides protons, Carbon ($C^{1+} \dots C^{5+}$) and Oxygen ions (O^{n+}) were identified with the Thomson parabola. The particle beams consistently show a *Boltzmann-like energy distribution* with typical temperatures of $k_B T = 0.15 - 0.5\ \text{MeV}$ for protons. *Cutoff energies* of $2.5 - 3.0\ \text{MeV}$ were concluded from the deflection behaviour as well as from stopping experiments with Aluminium foils.⁷

Titanium ($_{22}\text{Ti}$) and Tantalum ($_{73}\text{Ta}$) foils were analyzed as representatives for low-Z and high-Z targets, respectively. Thereby, foil thicknesses of 20, 12, 5, 2, and in the case of Titanium also 1 micron(s) were compared. The obtained spectra increase in proton yield and cutoff energy with decreasing target thickness, which follows the predicted behaviour [28, 42]. For Titanium (Fig. 3.20), the existence of an optimum thickness at $2\ \mu\text{m}$ is observed (cf. section 2.2.3). It was also verified that a large prepulse has a negative impact on both proton yield and cutoff energy [62]. Therefore, a zero prepulse was chosen for the dot experiments.

Furthermore, the proton acceleration from *double layer targets* was analyzed. Both Titanium and Tantalum foils of $2\ \mu\text{m}$ and $5\ \mu\text{m}$ thickness were combined with PMMA layers of various extent, reaching from 0.15 to $1\ \mu\text{m}$. In agreement with the results from other groups, a substantial increase in the particle yield could be observed, which proves the feasibility of

⁷Occasionally, energies beyond $4.5\ \text{MeV}$ were observed, too.

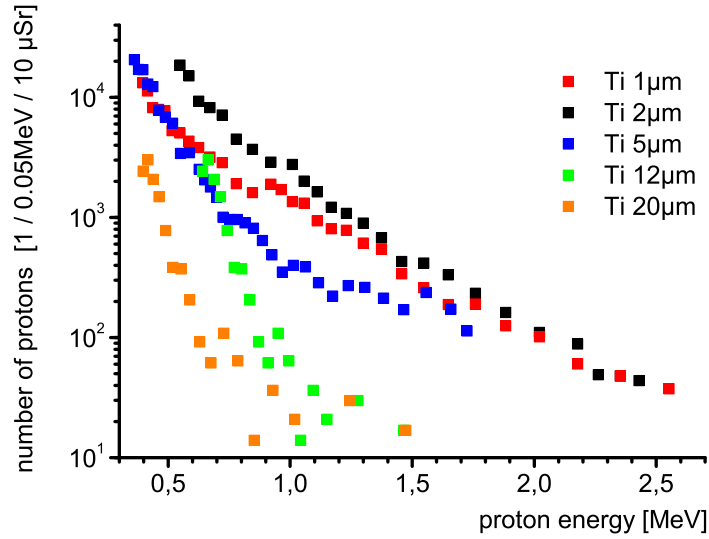


Figure 3.20: Proton spectra for Titanium foils of various thicknesses. All spectra show an exponential decay. For the current laser parameters, the optimum target thickness for Titanium is $2\ \mu\text{m}$, where a temperature of $k_{\text{B}}T = 0.17 \pm 0.01\ \text{MeV}$ and a cutoff energy of about $2.5\ \text{MeV}$ is obtained.

the double layer technique for the generation of monoenergetic beams. A comparison between uncoated and coated foils yields a *factor of* 6 ± 2 in the case of $5\ \mu\text{m}$ Titanium plus $0.5\ \mu\text{m}$ PMMA, and comparable values for other combinations. Fig. 3.21 shows the averaged spectra from single and double layer targets.

It shall be noted that no acceleration of heavy ions from the foil material was observed. In ref. [51] it was proposed that double layer and dot experiments should utilize targets with high- Z carrier foils as background material, so that protons are clearly preferred for acceleration due to their higher q/m -ratio and no energy is deposited on the heavy foil ions. However, since no energy is lost to the foil ions anyway, the argument does not hold true for the current situation: ^{22}Ti seems to be "heavy" enough. Since furthermore the results for Titanium were generally more stable and showed a higher proton yield, Titanium has been preferred for the production of microstructured targets.

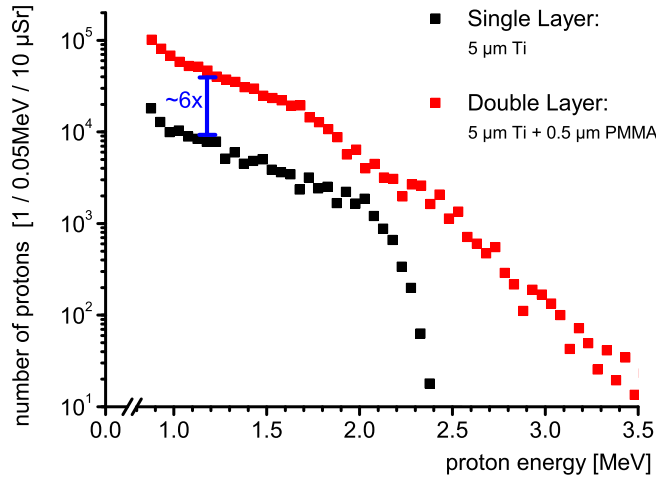


Figure 3.21: Comparison between conventional targets and double layer targets. A $5\ \mu\text{m}$ Titanium foil yields a 6 ± 2 times higher proton intensity when coated with a $0.5\ \mu\text{m}$ layer of PMMA. The displayed spectra are averaged over many shots at the same focus position and attain a temperature of $k_{\text{B}}T = 0.46\ \text{MeV}$ for the uncoated and $0.49\ \text{MeV}$ for coated foil, respectively.

3.3.2 Monoenergetic proton beams

Summary: Quasi-monoenergetic proton beams can be generated from laser-matter interactions with high reliability. More than 50 spectra with peaks around 1.3 MeV and 25-50% energy spread were observed. The peak position depends on the laser power. An increase in conversion efficiency from laser energy into proton energy by a factor of 2.5 was observed. The total number of monoenergetically accelerated protons is limited by the laser power, not by the dot size. Parasitic effects were reduced, but could not be eliminated. The full lateral extent of the TNSA field lies between 30 and 90 μm .

Throughout the thesis experiments, a large number of $20 \times 20 \times 0.5\ \mu\text{m}^3$ PMMA dots located on the back side of a thin Titanium foil ($5\ \mu\text{m}$) were irradiated following the aiming procedure as described above (cf. section 3.1.4). Now, if the recorded spectra are to acquire a monoenergetic form, the recorded ion tracks should display a visible change already. This is indeed observed: Fig. 3.22 (N) shows a typical proton track obtained from a conventional thin foil target with noticeably decreasing intensity from the left to the right, that is in direction of increasing energy towards the zero deflection point. The track leads to the well-known exponential spectrum with the typical cutoff behaviour. On the contrary, Fig. (D1-D3) show the results from the irradiation of dots. All three graphs *increase in intensity when approaching higher energies*; Fig. (D2) does barely yield any counts at the low-energy margin of the MCP at all. Accordingly, the spectra attain a new form: The Boltzmann-like decay is replaced by a clear peak (Fig. 3.23).

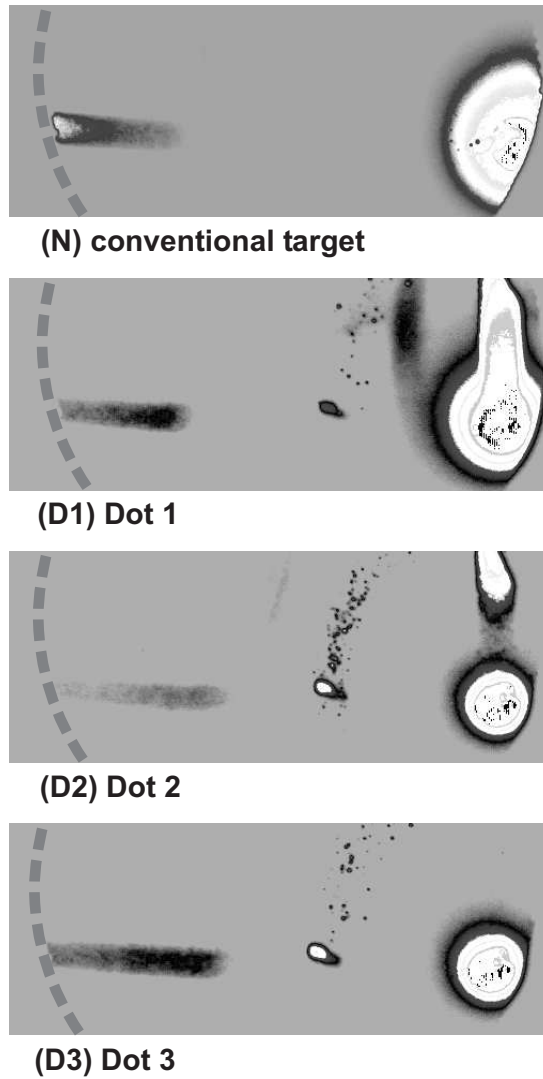


Figure 3.22: Peaked proton tracks recorded with the MCP. For a plain unstructured foil (N), the proton intensity continuously decreases from the left to the right (in direction of increasing energy), which yields the typical exponential spectra. Fig. (D1-D3) show the results of the dot irradiation: The intensity increases towards higher energies, which indicates the existence of non-thermal spectra. The spots close to the zero deflection point are artefacts. The dashed curve at the left end of the track represents the low-energy boundary of MCP of about 0.85 MeV.

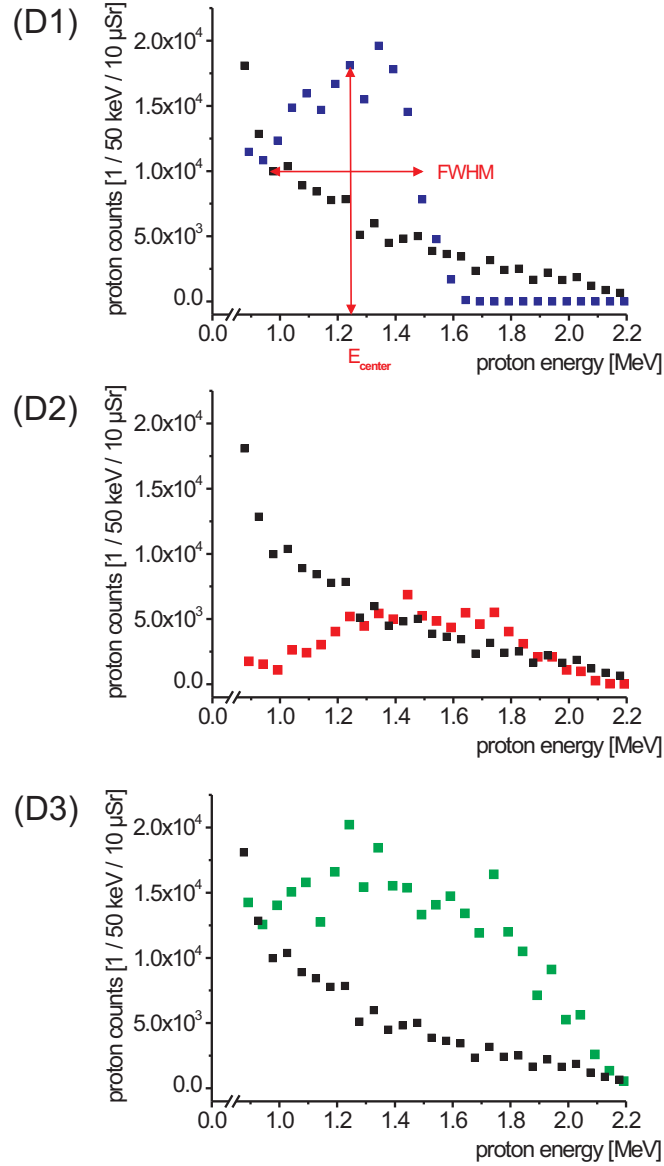


Figure 3.23: Monoenergetic proton spectra from dot irradiation. The three spectra correspond to Fig. 3.22 (D1-D3) and show a distinctly monoenergetic character. Peaks of variable height, width and position are observed. The averaged exponential background from conventional $5 \mu\text{m}$ Titanium targets as given in Fig. (3.21) has been inserted as reference (black squares). For Fig. (D1), the peak is located at $E_{\text{center}} = 1.25$ MeV, has a FWHM of $\Delta E_{\text{FWHM}} = 0.6$ MeV $\simeq 50\%$ and exceeds the background by a factor of 3.5, all of which are typical values.

The dot irradiation was carried at two different intensities. For $I_1 = (3.5 \pm 0.15) \times 10^{19} \frac{\text{W}}{\text{cm}^2}$, the average peak position can be found at $E_{\text{center}}(I_1) = 1.13 \pm 0.31 \text{ MeV}$, whereas $I_2 = (3.8 \pm 0.15) \times 10^{19} \frac{\text{W}}{\text{cm}^2}$ leads to $E_{\text{center}}(I_2) = 1.34 \pm 0.37 \text{ MeV}$. Peak functions for lower intensities might exist, but were not observed due to the limited size of the MCP ($E_{\text{min}} = 0.85 \text{ MeV}$). However, the difference of 0.21 MeV is considerable and proves the *dependence of the peak position on the laser power*. This dependence does approximately follow the theoretical predictions of section 2.2.2, where the TNSA field was found to be proportional to $\sqrt{I\lambda^2}$. The square root of the intensities gives a factor of

$$\sqrt{\frac{I_2}{I_1}} = 1.09 \pm 0.09, \quad (3.14)$$

whereas the observed energies are related as

$$\frac{E_{\text{center}}(I_2)}{E_{\text{center}}(I_1)} = 1.18 \pm 0.64. \quad (3.15)$$

It can be seen that the difference is well exceeded by the error and thus the square root scaling law holds true. However, the current intensities might still be below the threshold for a predictable acceleration behaviour (cf. scaling section 4.1) and the energy range where such a scaling becomes possible has not been achieved yet.

It is important to note that the peaks are generated in excess of the underlying background. As comparison, the averaged exponential spectra from conventional $5 \mu\text{m}$ Titanium targets have been inserted in each graph. From the ratio between peak maximum and background intensity it can be derived that the monoenergetic feature typically *exceeds the background* by a factor of 3.5. In Fig. 3.24 the exponential background was subtracted from Dot 1 (Fig. 3.23 D1), which gives the pure contribution from the dot.

The observed monoenergetic peaks vary considerably in their height. *Maximum proton numbers* from 1.5×10^3 to $2.1 \times 10^4 \frac{\text{protons}}{50 \text{ keV } 10 \mu\text{Sr}}$ were observed, which is a fluctuation of about one order of magnitude. Concerning peak width, the spectra display a full width at half maximum (FWHM) of 0.2 – 0.6 MeV, which corresponds to 25 – 50 % of E_{center} . This relatively large spread is due to the big dot size, which exceeds the laser focus by a factor of 40 in area.

The peak features typically contain a few 10^5 protons within $\Omega_{\text{obs}} = 10 \mu\text{Sr}$ solid angle of observation; for example 3.2×10^5 in the case Dot 3 (Fig. 3.23 D3). In section 3.3.4 it will be shown that the total angle of emission is at least $\Omega_{\text{em}} = 24 \text{ mSr} = 2.4 \times 10^3 \Omega_{\text{obs}}$, which allows to give an estimation about the *total proton number*. The number of monoenergetically accelerated protons from Dot 3 thus amounts to $\geq 8 \times 10^8$.

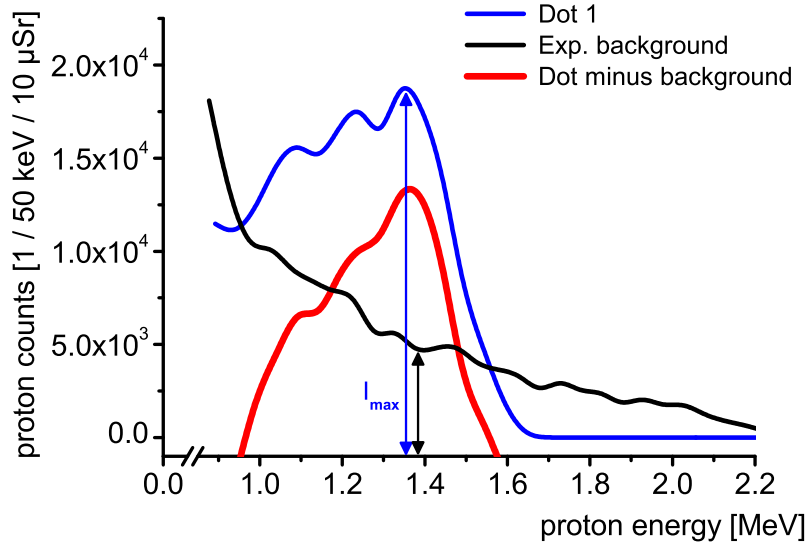


Figure 3.24: Difference between the dot spectrum (blue) and the exponential background (black) from Fig. 3.23 a). The remaining intensity peak (red) gives the pure contribution of the proton rich dot in the TNSA field.

In comparison, a PMMA dot of $20 \times 20 \times 0.5 \mu\text{m}^3$ size consists of

$$\begin{aligned} N_{\text{prot}} &= n_{\text{H, PMMA}} V_{\text{dot}} \\ &\approx 1.2 \times 10^{13} \end{aligned} \quad (3.16)$$

protons, which shows that only 0.01% of the available protons have been accelerated. Here, $n_{\text{H, PMMA}} = 6.02 \times 10^{10} \text{ 1}/\mu\text{m}^3$ is the Hydrogen particle density in PMMA, which can be derived from the density of PMMA ($\rho_{\text{PMMA}} = 1.19 \frac{\text{g}}{\text{cm}^3}$) and its chemical composition ($\text{C}_3\text{H}_5\text{COOCH}_3$). The height of the monoenergetic peak thus turns out to be limited by the accelerating potential, and not by the available number of protons. The large reservoir can not be exploited with the current laser power, but will be of interest when discussing future laser generations and applications subsequently.

The *conversion efficiency* from laser energy into proton energy can be determined from integrating over the obtained spectra. Since the MCP detection is limited at the low energy boundary to 0.85 MeV, one can thereby consider a certain energy interval only. The energy contained in Dot 3 (Fig. 3.23 D3) is about $6 \times 10^{-6} \text{ J}$, which yields a conversion efficiency of $\alpha_{\text{conv}}(\text{Dot1}) = 10^{-5}$ from laser energy into monoenergetic protons, i.e. those between 0.9 MeV and 2.0 MeV. For the same interval, the exponential background shows a conversion efficiency of 4×10^{-6} . The acceleration from a microdot has thus increased the conversion efficiency by

a factor of 2.5 within the relevant energy range.

In many spectra, the low energy edge of the peak drops below the background distribution. Thus, the *reduction of parasitic protons* via laser ablation was (at least partially) successful. Fig. 3.23 D2) shows such a spectrum. In other cases, the peak features merge with the exponential background again, which indicates a remaining parasitic contribution. Considering the ablation of the alignment laser on the back side (cf. section 3.1.5), the origin of these parasitic protons can not be ascribed to contamination layers, but rather to neighbouring dots with insufficient separation. From this fact, the lateral extent of the TNSA field can be concluded. The observation of monoenergetic spectra implies that the *whole* dot ($20 \times 20 \mu\text{m}^2$) must have been exposed to the accelerating field, which sets the lower limit for the dimension of the field to $\sqrt{2} \cdot 20 \mu\text{m}$. The upper limit is determined by the distance between two dots; if the neighbouring dot had reached significantly into the weak fringe of the accelerating field, no monoenergetic spectra would have occurred. The size of the TNSA field and hence the *emission source size* for conventional proton acceleration under the current laser and target conditions therewith amounts to $30 - 90 \mu\text{m}$.

The presented results are no singular occurrences, but represent a very stable phenomenon. Dozens of monoenergetic spectra have been recorded from the interaction of TW-laser pulses with microstructured targets. A peak feature consistently appears if a dot is irradiated. It shall be noted that the irradiation of areas *between* the dots never yielded any monoenergetic feature, which is a convincing argument for the accuracy of the alignment method. The overall aiming accuracy can be as high as 71 % per day (35 out of 52 shots). The misses can be sufficiently explained the pointing instability of the laser ($\sim 3 \mu\text{m}$) or an inhomogeneous distribution of the dye within the dot, which can prevent an exact localization. In the following, two methods of validation for the obtained results shall now be presented.

3.3.3 CR39 comparative shots

Summary: The use of CR39 fully support the previous results. Quasi-monoenergetic peak features appear on top of an underlying, exponential background.

Several shots on CR39 have been recorded in order to support the acquired results. Similar to the MCP detection, the evaluation yields both peaked and unpeaked spectra. Again, the peaks appear in excess of an exponential background. The background contribution can be seen to continue for low energies, which could not be observed with the MCP before due to its limited size. Fig. 3.25 shows such a CR39 spectrum. The graph displays a distinct, quasi-monoenergetic feature that matches the above results with all respects. The solid line is a fit of the exponential background.

Both detection methods thus prove to be in perfect agreement. However, it has to be re-emphasized that the availability of an online observation strongly contributed to the success of the experiment, since it pointed out the spectral region of interest immediately.

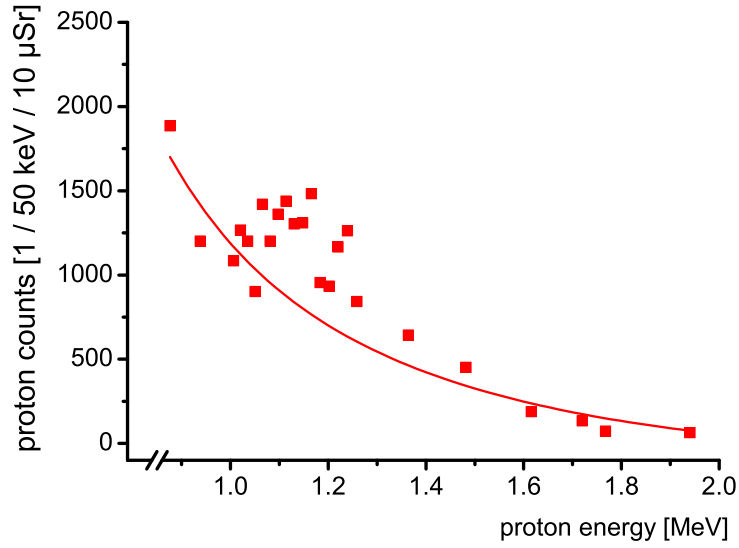


Figure 3.25: Peaked spectrum recorded from a single shot on CR39. In agreement with the MCP data, quasi-monoenergetic spectra were recorded also with track detector plastics. The solid line represents a fit of the exponential CR39 background.

3.3.4 2D Particle-In-Cell simulation

Summary: A 2D PIC simulation excellently reproduces the experimental results. The total number of quasi-monoenergetic protons can be estimated to 8×10^8 within 24 mSr solid angle.

The production of monoenergetic protons from microstructured targets was predicted by a theoretical work that correlated the spectrum to the initial proton distribution on the target [58]. The results were bound to a specific set of simulation parameters, which differ largely from the present experimental situation. Here, the target is given by Titanium foil with Hydrocarbon coating instead of Gold with purely protons. The layer thicknesses exceed the simulation values by a factor of 10. Furthermore, the laser does not operate at $a_0 = 30$, but at $a_0 = 4$, and the focus is not twice as large as the dot, but only a small fraction of its size. The question arises, whether under these conditions the theoretical model would still support a monoenergetic behaviour.

A numerical simulation of the present experimental situation was performed by T. Esirkepov [9]. The same model as used in ref. [58] was applied to the conditions of the current setup. The simulation is based on a 2D Particle-in-Cell (PIC) code called REMP ("relativistic electromagnetic particle-mesh"), which uses the hydrodynamic model of Matsukado et al. [59]. The fully vectorized motion of 8.2×10^8 particles was calculated at the NEC SX-5 computer at Osaka University, Japan. A screenshot of the simulation is shown in Fig. 3.26.

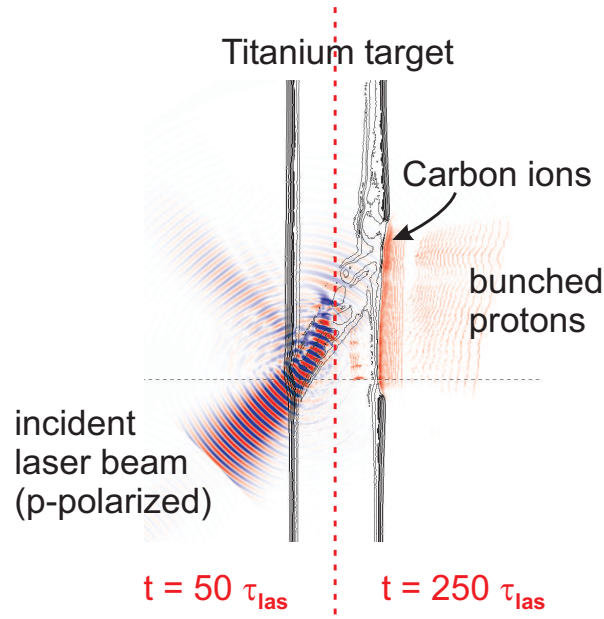


Figure 3.26: Screenshot of the 2D PIC simulation. The laser incidence at the front side and the acceleration of a bunch of quasi-monoenergetic protons from a confined source are shown for different times (50 and 250 laser cycles, respectively). The Carbon ions can be seen to remain comparably immobile.

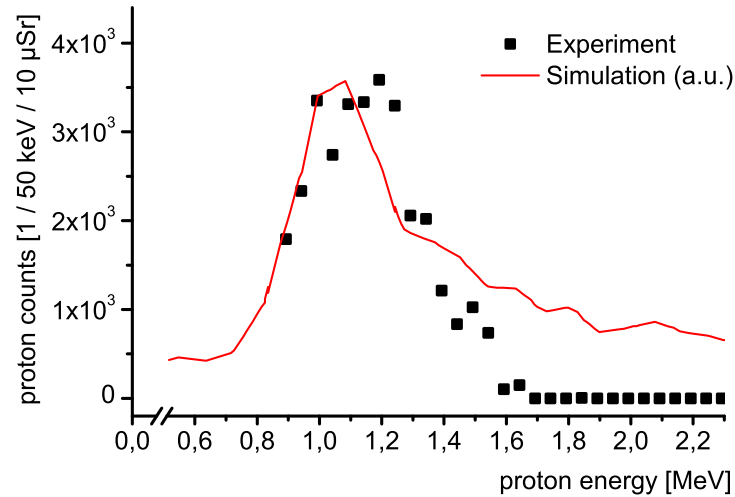


Figure 3.27: Results from the 2D PIC simulation carried out for the parameters of the experiment ($I = 4 \times 10^{19} \text{ W/cm}^2$, $A_{\text{foc}} = 5 \mu\text{m}^2$, $A_{\text{dot}} = 20 \times 20 \mu\text{m}^2$, $5 \mu\text{m Ti} + 0.5 \mu\text{m PMMA target}$). The calculation yields a distinct peak at 1.2 MeV (red line), which excellently fits the experimental data (black squares). The simulation curve has been normalized to fit the real spectrum.

The result of the simulation is shown in Fig. 3.27. A distinct monoenergetic peak appears in the spectrum at an energy of about 1.2 MeV. The peak possesses a FWHM of about 0.3 MeV (= 25%). The simulation is given in arbitrary units. As comparison, a real dot spectrum has been inserted in the graph. Simulation and experiment agree excellently with respect to the relative peak height, its width and position.

The simulation yields that the proton emission for a peaked spectrum at 1.2 MeV occupies a solid angle of 24 mSr. Earlier measurements at the JETI with conventional double layer targets ($2\ \mu\text{m Ti} + 1\ \mu\text{m PMMA}$) resulted in the much bigger value of 275 mSr, which indicates that the dot acceleration is indeed restricted to the central and less divergent part of the acceleration field. For the smaller value, the ratio between solid angle of emission and solid angle of detection amounts to

$$\begin{aligned}\alpha_{\text{scale}} &= \frac{d\Omega_{\text{em}}}{d\Omega_{\text{detect}}} \\ &= \frac{24\ \text{mSr}}{10\ \mu\text{Sr}} = 2.4 \times 10^3,\end{aligned}\tag{3.17}$$

which allows to give a lower limit estimation for the *total number of homogeneously accelerated protons* from the observed spectra. For the 3.2×10^5 protons in Fig. 3.23 D1), one obtains a total number of protons of 8×10^8 .

4 Outlook

4.1 Petawatt scaling: prospects of the POLARIS laser class

Summary: The POLARIS laser system will deliver pulses of $I \approx 10^{21} \text{ W/cm}^2$ by 2008. For such Petawatt lasers, the maximum proton energy scales with $P_{\text{laser}}^{1/2}$. A 2D PIC simulation carried out for the POLARIS parameters yields a monoenergetic peak at 173 MeV with 0.6% bandwidth.

The current results are mainly limited by two factors: the target quality and the laser power. The target quality, i.e. dot size and separation, determines the energy spread and the contrast ratio of the monoenergetic feature. The fabrication procedure is currently under improvement and will provide better targets for the next campaign (see Fig. 5.1). On the contrary, the laser power determines the peak position. An improvement with that respect can not be achieved on a short term basis, but depends on the development of new high intensity lasers.

An ambitious laser project is the POLARIS laser at the University of Jena [77]. The POLARIS will employ diode-pumped Yb^{3+} :Glass for the amplification of Ti:Sa pulses to about 1 PW ($1 \text{ PW} = 10^{15} \text{ W}$). At the present stage, four out of five amplification stages have been established and tested to achieve stable pulse energies up to 8 J. In an optimistic estimation, the fourth amplification stage including the compressor will be finished by the end of 2006 and deliver 15 – 20 J, whereas the final amplifier and thus the whole system is likely to be completed by 2008. The POLARIS operates at a central wavelength of 1042 nm and provides pulses of 16 nm bandwidth and 150 fs duration at a repetition rate of 0.1 Hz. The pulses can be expected to create intensities of $I \approx 10^{21} \text{ W/cm}^2$ on target within a focus of $10 \mu\text{m}$ diameter ($A_{\text{foc}} \approx 80 \mu\text{m}^2$), which outmatches the JETI by two orders of magnitude.

For such a rise, the conditions of laser driven ion acceleration will change. D’Humieres et al. pointed out that in the Petawatt regime the quasistatic field acceleration is supported by a shock wave from the target bulk, which may outmatch the conventional TNSA mechanism [42]. This conclusion is based on a study that distinguishes between three different regimes of proton acceleration: an opaque regime for thick targets and comparably low laser intensities (the well-known TNSA), a transparent regime that allows the laser to pass through the very thin foil almost undisturbedly, and a the laser shock regime as a kind of optimum between the transparent and opaque case.

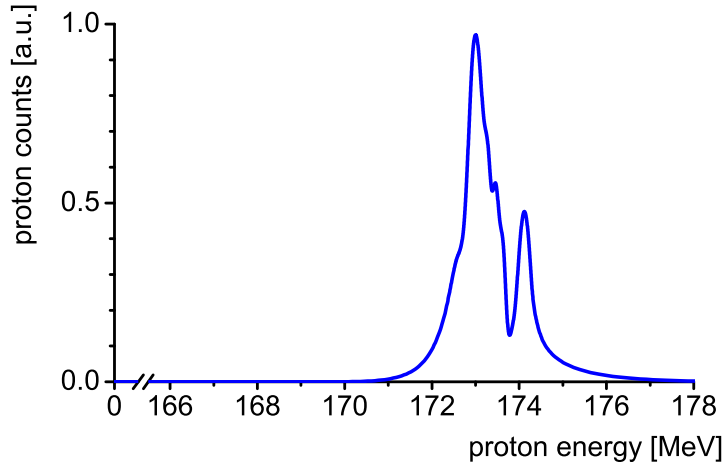


Figure 4.1: Scaling of the monoenergetic acceleration to the Petawatt regime. The irradiation of a dot with $2.5\ \mu\text{m}$ diameter and $0.1\ \mu\text{m}$ by a $150\ \text{J}$ & $150\ \text{fs}$ laser pulse focussed to a spot of $10\ \mu\text{m}$ diameter was simulated, which resembles the conditions for the Jena POLARIS laser system currently under construction. The resulting spectrum shows a distinct peak at $173\ \text{MeV}$ with about $0.6\ \%$ energy spread.

In agreement with this division, Esirkepov et al. identify the third regime as a "radiation pressure dominant" regime [78]. In a scalability study on ion acceleration they find that for the successful exploitation of this regime, the so-called *critical depth*¹ must attain a certain optimum value. For this optimum, they derive the *scaling law*

$$E_{\text{cutoff}} \approx 228\ \text{MeV} \times Z \sqrt{P_{\text{laser}}/1\ \text{PW}} \quad (4.1)$$

for laser accelerated ions, where Z is the ion charge. This result displays the same $P_{\text{laser}}^{\frac{1}{2}}$ -dependency as obtained for the conventional TNSA field in section 2.2.3.

Acknowledging these results, a second PIC simulation was performed following the POLARIS parameters: a laser pulse of $E_{\text{POL}} = 150\ \text{J}$ and $\tau_{\text{POL}} = 150\ \text{fs}$ is focussed to a spot of $d_{\text{foc}} = 10\ \mu\text{m}$ diameter, which leads to an intensity of $I_{\text{POL}} = 1.2 \times 10^{21}\ \text{W}/\text{cm}^2$. The target consists of a $5\ \mu\text{m}$ Titanium foil with PMMA dots of $d_{\text{dot}} = 2.5\ \mu\text{m}$ diameter and $\Delta z_{\text{dot}} = 0.1\ \mu\text{m}$ thickness. The simulation follows again the model described in section 3.3.4.

Fig. 4.1 shows the results of the simulation. The obtained spectrum yields a distinct peak at $E_{\text{center}} = 173\ \text{MeV}$ with an energy spread of about $\Delta E_{\text{FWHM}} = 1\ \text{MeV}$ or $0.6\ \%$. In comparison to the JETI results, this means a rise in energy by a factor of 130, and an improvement in relative peak width by a factor of 50. However, it can be seen that the result differs from equation (4.1), which predicts a maximum proton energy of $228\ \text{MeV}$. The deviation can be

¹The critical depth is the product of target thickness and electron density, $\sigma_c = n_e d_{\text{target}}$.

explained by the fact that Esirkepov's scaling law holds true only for the optimum critical depth, which is not given for simulated POLARIS conditions.

For the Petawatt regime, the simulation yields that the acceleration of protons from a dot source is no longer limited by the laser power. It can be seen that the protons are detached and accelerated in a bunched manner. The monoenergetic peak thus contains all of the 3×10^{10} protons abundant in a $0.5 \mu\text{m}^3$ dot.

It shall be noted that for Petawatt regime the proton motion becomes relativistic. The relativistic factor can be estimated via

$$\gamma = \frac{E_{\text{kin}}}{m_p c^2} + 1 \approx \frac{173 \text{ MeV}}{1 \text{ GeV}} + 1 = 1.173, \quad (4.2)$$

which proves to be no longer negligible and thus requires an advanced proton beam analysis. On the other hand, the directly laser-induced ion quiver motion still remains comparably small as can be seen from the relativistic parameter a_0 (equation 2.21).

4.2 A promising application

4.2.1 Stopping of fast ions in matter

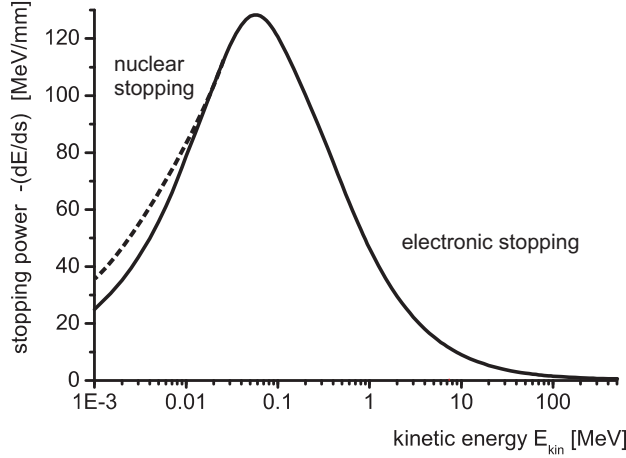
Summary: The stopping of ions in solids follows a Z^2/v^2 -dependence and shows distinctly peaked absorption cutoff. In the case of protons in biological tissue, this Bragg peak contains 3.3 MeV within $175 \mu\text{m}$.

The past chapters delivered an overview about a seminal technique for the production of energetic ion beams. In the following, the practical use of such ion beams shall now be expounded.

When ions penetrate a solid target², they are stopped in a characteristic manner due to the Coulomb interaction with the target atoms. The interaction can be basically divided into two contributions, an electronic and a nuclear one, which correspond to two different regimes of energy loss [79]. In the regime of *electronic interaction*, the incident ion still performs a relatively straight propagation, thereby displacing the hull electrons along its path. If the particle is already sufficiently slow, elastic scattering at the positive nuclei will gain importance and support the stopping process. At this regime of *nuclear interaction*, the incident particle will be deflected from its original path and come to rest very quickly.

The stopping of ions in matter is typically characterized by the differential loss of kinetic

²The discussion shall here be limited to "heavy" particles of at least proton mass.



(a)

Figure 4.2: Stopping power of Aluminium as given by the National Institute of Standards and Technology (NIST) charts [82]. The curve is based on equation (4.3) for energies above 0.5 MeV and experimental data for lower energies. The maximum is given at 0.06 MeV. A phenomenological correction for the contribution of nuclear interactions has been added to the falling edge at left hand side.

energy along the penetration path, the *stopping power* $-\frac{dE_{\text{kin}}}{ds}$, which is given by [80, 81]

$$-\frac{dE_{\text{kin}}}{ds} = \frac{Z^2 e^4 n_e}{4\pi \varepsilon_0^2 m_0 v^2} \left\{ \ln \frac{2 m_0 v^2}{\overline{E}_{\text{ion}}} - \ln\left(1 - \frac{v^2}{c^2}\right) - \frac{v^2}{c^2} \right\}, \quad (4.3)$$

$$\sim \frac{Z^2}{v^2},$$

where n_e and $\overline{E}_{\text{ion}}$ are the electron density and the average ionization energy of the stopping material and Z is the charge of the incident particle. Equation (4.3) shows a square dependency on the particle charge and initial velocity. The first term in parentheses is a semi-classical term that can be obtained by integrating the transfer of momentum between particle and target electrons within a cylindrical interaction volume. The latter terms represent a relativistic correction up to $E_{\text{kin}} \approx m_0 c^2$. The stopping power for protons in Aluminium is displayed in Fig. 4.2. The graph shows a characteristic maximum, which resembles a regime of most efficient stopping.

The peak behaviour leads to the effect that a fast particle can propagate relatively undisturbedly and with a constant energy loss for a long time, until it undergoes a certain threshold after which it is stopped very rapidly, thereby depositing almost its entire energy within a small volume [79, 80]. This behaviour is shown in Fig. 4.3, where the energy loss in Aluminium and biological tissue is given as a function of proton penetration depth. The strong peak (*Bragg peak*) defines the depth of predominant energy deposition and can exceed the quasi-constant energy loss by a factor of > 10 . The maximum penetration depth (*stopping range*) can be

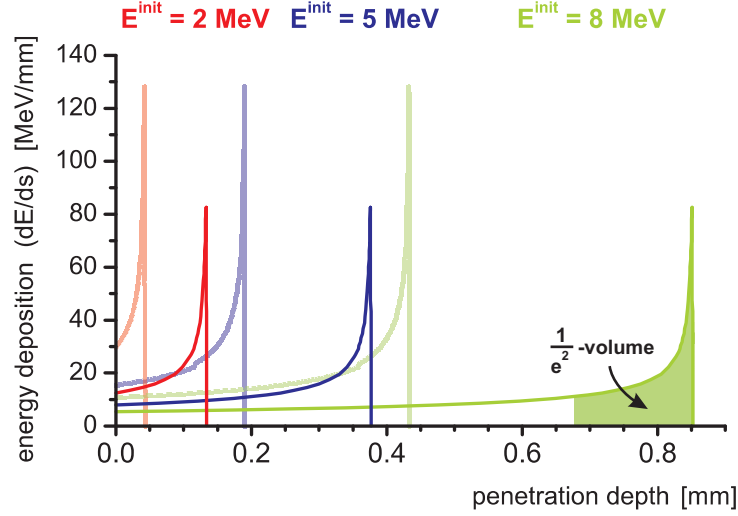


Figure 4.3: Stopping behaviour as a function penetration depth for Aluminium (transparent lines) and biological tissue (solid lines). The stopping range is comparable to the position of the Bragg peak. For each material, the peak width ($\frac{1}{e^2}$) and the therein deposited energy is constant, which in the case of tissue irradiation amounts to 3.3 MeV within 175 μm .

seen to be located very closely to the Bragg peak.

From equation (4.3) it follows, that the width of the Bragg peak is constant regardless of the initial energy, namely 150 μm for Aluminium and 175 μm for biological tissue (Fig. 4.3). Thus, the amount of kinetic energy deposited within the peak is constant, too, and attains

$$\Delta E_{\text{Bragg}}^{\text{Alu}} \left(\frac{1}{e^2} \right) \approx 4.4 \text{ MeV}, \quad (4.4)$$

$$\Delta E_{\text{Bragg}}^{\text{tissue}} \left(\frac{1}{e^2} \right) \approx 3.3 \text{ MeV}. \quad (4.5)$$

The stopping of the incident ion is accompanied by an excitation and ionization of the stopping medium along the penetration path. Hence, the Bragg peak corresponds to a region of maximum ionization density. The irradiation of biological tissues with energetic particle beams has thus been identified as a highly suitable mechanism for the treatment of cancer. In the final section, the perspective of laser produced proton beams for such a *proton therapy* shall be evaluated.

4.2.2 Medical proton therapy

Summary: Current laser accelerators allow for first biophysical experiments. Lasers of the POLARIS class will fulfill the requirements for proton therapy. If such lasers can be operated sufficiently stable, first clinical experiments are conceivable within a 10-years timescale.

Cancer treatment is closely connected to the application of high energy radiation. About two thirds of all cancer patients are treated with radiation therapy, or *radiotherapy* [83]. In this medical context, the term radiation refers to both electromagnetic and particle beams. The central purpose of all radiation therapy is to modify the rapidly growing cancer cells such that they will either be prevented from reproduction by an alteration of their DNA, or die from the irradiation directly.

Proton therapy is a very sophisticated technique, and treatment facilities are still rare around the world. In contrast to the exponentially absorbed X-rays, protons and ions follow the characteristic stopping law presented above. They also exceed electrons with respect to their ionization power (Fig. 4.4), which makes them the ideal candidates for a precise treatment of inoperable tumors in a sensitive vicinity. Table (4.1) gives the proton stopping range in different materials for various energies. The data was again taken from NIST charts [82].

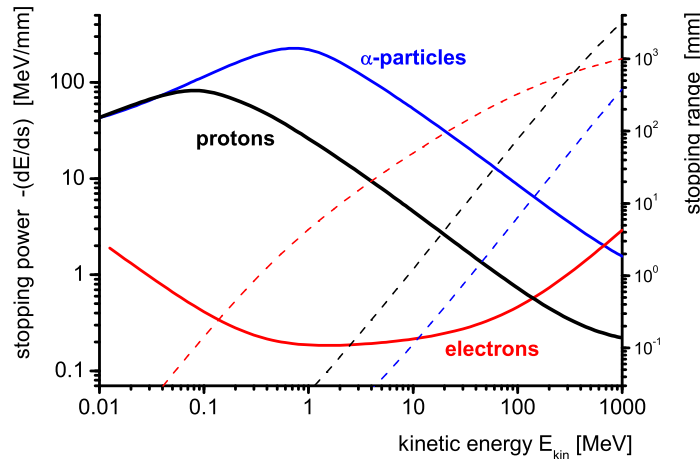


Figure 4.4: Comparison of the stopping power of electrons, protons and α -particles in biological tissue. The solid plots show the energy loss in MeV/mm peak. The ion beams are superior to the electrons with respect to the maximum deposited energy, which is due to the confined absorption in the Bragg peak. This leads to a higher ionization rate and minimizes the effect on surrounding healthy tissues. The stopping range is given by the dashed lines.

E_{kin} [MeV]	1	3	10	30	100	300
range in <i>air</i> [mm]	23	144	1E3	8E3	7E4	5E5
<i>Aluminium</i>	0.01	0.08	0.62	6.48	36.95	242.81
<i>Lead</i>	0.01	0.05	0.30	1.83	14.24	89.25
<i>water / tissue</i>	0.02	0.14	1.23	8.84	77.07	513.90
<i>muscle</i>	0.02	0.15	1.19	8.57	74.75	498.46
<i>bone</i>	0.01	0.09	0.72	5.18	44.89	298.22

Table 4.1: Proton ranges in mm for different stopping materials. The stopping range corresponds approximately to the position of the Bragg peak.

So how could laser-produced proton beams contribute to this treatment method? Current proton therapy centres are run with LINACs (Linear accelerators) or small cyclotrons, both of which are well-established, commercial devices.³ Thus, with respect to the acquisition and running costs as well as the required space, a high-intensity laser system of the POLARIS class does not seem advantageous, at least at the present stage of development. A mere application as a substitute proton source while keeping the conventional infrastructure as suggested by Bulanov et al. [51] therefore seems unreasonable.

However, Bulanov et al. also propose a second scheme, which locates the proton source, i.e. the comparably small thin foil target, as close as possible to the patient. In such a setup, the whole assembly of rotatable magneto-optics and large parts of gantry system become superfluous - the only thing to be guided is laser light. The the costs of a single treatment unit could thus be reduced significantly.

Now, is the physics of laser plasma acceleration really feasible for a routine medical application? Before answering this strong inquiry, consider a weaker one first: Are laser accelerated protons *in principle* suitable for a biological application? This question can be confidently answered with "yes" - the irradiation of cancerous tissues with laser accelerated proton beams is conceivable within the next years:

Medical proton therapy requires the application of monoenergetic proton beams with high energy. Proton beams with tens of MeV have been generated at the Lawrence Livermore Labs [36] and demonstrate the feasibility of the TNSA mechanism for high energies. Studies at the Laboratoire d'Optique Appliquée Palaiseau [8] and the IOQ Jena [62] show that protons can be produced from laser plasmas with high repetition rate. The first production of monoenergetic proton beams with the help of microstructured targets has been reported by Schwoerer et al. [9] and discussed in this work. Simulations allow to project the results to higher laser intensities, i.e. to the next laser generation. A high repetition rate PW-laser system will be available in Jena soon [77], which is capable of accelerating protons up to 173 MeV. This value

³It has to be emphasized that laser accelerators do not compete against the Stanford SLAC or the CERN SPS, but against comparably small accelerators, which deliver quasi-continuous particle beams and can be operated by small number of people.

$\Delta E_{\text{FWHM}}/E_{\text{center}}$	0.001	0.003	0.006	0.01	0.03	0.1	0.3
ΔE_{FWHM} at $E_{\text{center}} = 173 \text{ MeV}$	0.2 MeV	0.5 MeV	1.1 MeV	1.7 MeV	5.1 MeV	17.3 MeV	51.9 MeV
Δs_{Bragg}	0.4 mm	1.0 mm	2.2 mm	3.4 mm	10.3 mm.	53.6 mm	104.8 mm

Table 4.2: Bragg peak width for different degrees of monochromacy. The top row gives the relative spectral bandwidth of the applied proton beam, whereas in the second row the absolute values for a peak at $E_{\text{center}} = 173 \text{ MeV}$ are given. The bottom row states the resulting spatial width of the broadened Bragg peaks, where the intrinsic $\frac{1}{2}$ -width of a monoenergetic Bragg peak ($\approx 175 \mu\text{m}$, cf. section 4.2.1) has been neglected. For the POLARIS laser, the simulation yields an energy width of 1.1 MeV at 173 MeV (0.6 %), which corresponds to a 2.2 mm broad Bragg peak. All values stem from NIST charts [82].

corresponds to a penetration depth of 206 mm in biological tissue [82] and is thus suitable for the treatment of deep seated tumors.

The expected radioactive dose of such a proton beam can be calculated from the deposited energy per irradiated tissue mass

$$\Delta D = \frac{\Delta E_{\text{dep}}}{\Delta m_{\text{irrad}}} = \frac{N_{\text{prot}} \cdot \Delta E_{\text{Bragg}}^{\text{tissue}}}{\rho_{\text{tissue}} \cdot V_{\text{irrad}}}, \quad (4.6)$$

where N_{prot} is the number of incident protons, $\Delta E_{\text{Bragg}}^{\text{tissue}}$ is the constant amount of energy contained in the Bragg peak as given above, $\rho_{\text{tissue}} \approx \rho_{\text{H}_2\text{O}}$ is the density of the irradiated volume and V_{irrad} the irradiated volume. This minimum volume is determined by the beam diameter and the width of the broadened Bragg peak resulting from the finite energy spread of the protons. Assuming that all 3×10^{10} protons available in a $0.5 \mu\text{m}^3$ dot are accelerated and deposited within typical tumor size of 1 cm^3 (which should certainly be possible with the help of proton lenses [84, 85]), this results in an effective dose of $\Delta D = 7 \text{ Gy}$ per POLARIS shot (cf. Table 4.2). Throughout a typical therapeutical, session doses of only a few Gy are applied [86]. The required amount could thus be delivered by a single shot.

In the meantime, current proton beams can readily be used to carry out first biophysical proof-of-principle experiments. Since the penetration depth of 1.25 MeV protons in biological tissue is only $35 \mu\text{m}$ (Fig. 4.4), these experiments are restricted to surface irradiation, for example on skin cancer probes. Assuming that all available protons (8×10^8) are focussed to a beam of 1 cm diameter, one obtains a dose of $\Delta D_{\text{JETI}} = 58 \text{ Gy}$ due to the small penetration depth. Even if experimental conditions from the thesis experiments are kept unaltered ($10 \mu\text{Sr}$ solid angle of detection and 3 mm beam diameter), one can achieve a "surface dose" of 1 Gy by accumulating over 4 shots. All of this suggests that *biophysical experiments with laser-accelerated protons can be expected within the next couple of years.*

Regarding the question whether laser accelerators can enter a clinical routine application,

the author would answer with a qualified yes. This qualification does not refer to the fundamental physics involved but to the necessary engineering work.

The major challenge is clearly the laser technique itself. A medical proton source must deliver a most reliable beam. Only if this criterion is fulfilled, further arguments can be considered and the advantages of laser accelerators can eventually pay off. For cancer treatment, beam fluctuations are unacceptable with respect to all proton flux, energy and bandwidth. A energy uncertainty of $\Delta E_{\text{prot}}^{\text{max}} \approx 0.3 \text{ MeV}$ would shift/broaden the Bragg peak by 1 mm. The flux determines the applied dose and should thus be at least as constant as $\pm 5\%$.

However, these requirements seem surmountable. In our experiments, an aiming accuracy of up to 70% could be achieved, which can be expected to improve further with a better target and observation setup. The applied intensities of $3.8 \times 10^{19} \text{ W/cm}^2$ consistently produce peak features at $1.34 \pm 0.37 \text{ MeV}$ with energy spreads ranging from 0.2 – 0.6 MeV. The observed effect thus represents a very stable phenomenon feasible for an exploitation by medical physics.

High intensity laser systems are no turn-key devices, even if the current laser generation is already commercially available. Lasers of the POLARIS class will no longer be table-top either, but require extensive facilities and maintenance. Nonetheless it is realistic that - after their first launching in 2-3 years from now - such lasers will be brought from a prototype stage to a stage of experienced and quasi-commercial application within another 5 years. By then, biophysical experiments will have been carried out at high intensity laser facilities already so that laser accelerators might enter a clinical test phase in 7-10 years from now.

5 Conclusion

The presented thesis has discussed the generation of monoenergetic proton beams from laser plasmas under theoretical, experimental and speculative aspects. From this broadened perspective, the three assertions of the thesis claim shall be recollected:

Table-top laser systems can reliably produce quasi-monoenergetic proton beams. A concept for the generation of monoenergetic proton beams from relativistic laser-matter interactions has been presented. The concept applies the well-known Target Normal Sheath Acceleration to a confined proton source. The feasibility of this scheme was predicted by simulations, but can in itself be understood intuitively. Here, the first experimental evidence of quasi-monoenergetic proton beams from laser plasmas was reported. In agreement with the simulations, the application of a proton rich dot to the centre of the acceleration field results in a greatly reduced energy spectrum. In more than 50 shots peak features at about 1.3 MeV with 25 – 50% energy spread were generated, which impressively demonstrates the reliability of the effect. Supported by the reduction of the parasitic protons via laser ablation, an increase in conversion efficiency by a factor of 2.5 could be concluded for the peak region.

This resembles a very principle step towards application. The presented thesis must be understood as a proof-of-principle work: It has been shown for the first time that laser accelerators are in fact capable of producing monoenergetic ion beams. As has been mentioned in the introduction, most applications depend on the availability of such spectra with limited bandwidth. The results of this work indicate that custom-shaped proton spectra can be achieved with an according refinement of the target geometry. With this respect, future experiments will have to perform systematic studies on the impact of the dot parameters, i.e. their base area, thickness, material and separation (see picture below). Presupposing a sufficient flexibility in laser intensity, the dependence of the peak position on the laser power will also have to be analyzed more closely.

Promising technologies like laser-based proton therapy thus become conceivable on a 10-year timescale. It has been argued that first biophysical experiments, e.g. the irradiation of skin cancer tissues with proton beams, are offhand conceivable. However, the exploitation of monoenergetic beams will have to wait until the next laser generation. The peak position has been shown to depend on the laser power and scales with $\sim P^{1/2}$ for Petawatt intensities. A Petawatt laser system, the Jena POLARIS, will be available within the next couple of years. Scaling studies and simulations indicate that this system will provide proton pulses at around 173 MeV with 0.6% energy spread, which suffices to reach tumors at 20 cm depth. The energy

CONCLUSION

spread corresponds to a Bragg peak of 2.2 mm width, which approaches the requirements for proton therapy. All of this indicates that laser accelerators are in fact feasible for commercial medical use: all basic principles for such an application have been established throughout the last years, and hence laser driven proton therapy does not require fundamentally new physics, but another 7-10 years of determined engineering. Although Petawatt lasers will neither be table-top nor turn-key, they can contribute greatly to a reduction of the necessary infrastructure and hence the costs for treatment facilities, which will make medical proton therapy available to a wider audience.

In prospect of the POLARIS laser class, the results of the presented diploma thesis can be positioned on a larger timescale. It is foreseeable that laser particle physics will undergo a shift towards application. If one considers the 60 years of conventional accelerator research that lead to the establishment of proton therapy centres, the estimated decade for an equal development of laser accelerators is rather encouraging. Within this development, the generation of suitable monoenergetic proton beams will play a decisive role.

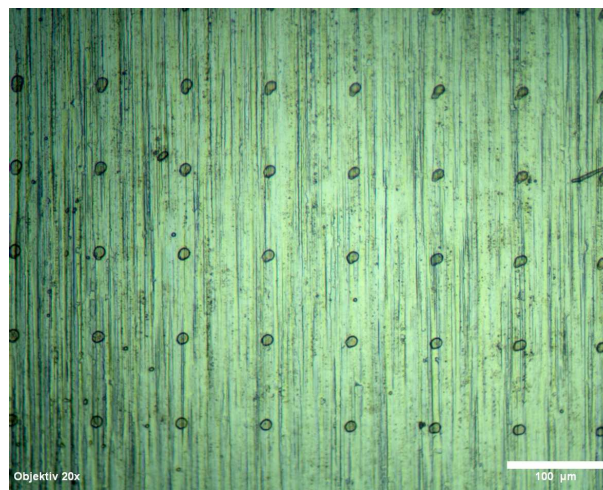


Figure 5.1: The next generation of dot targets (February 2006).

List of Figures

2.1	Laser pulse entering a given (pre-)plasma profile	12
2.2	Wake field acceleration	16
2.3	Target Normal Sheath Acceleration (TNSA)	19
2.4	Formation of the Debye Sheath	21
2.5	Proton emission within energy cones; real and virtual source size	23
2.6	Reduction of contamination layer via laser ablation	25
2.7	Double layer target	26
2.8	Confined acceleration within the homogeneous central field region	27
2.9	Simulation of the homogeneously accelerated proton bunch as presented in ref. [58]	28
2.10	Expected spectrum for the confined acceleration from a dot	30
3.1	The Jena 15 TW Ti:Sa Laser System (JETI) with 10 Hz repetition rate	34
3.2	Target and detection chamber	36
3.3	Microstructured thin foil target (I)	38
3.4	Microstructured thin foil target (II)	39
3.5	Correlation between the z -position of the target, the laser intensity and the detected radioactive dose	40
3.6	Focal overlap of Ti:Sa beam with Nd:YAG alignment laser	41
3.7	Principle of the fluorescence observation of the polymer dots	42
3.8	Picture of the fluorescence observation	42
3.9	Dots moving through the observation focus	43
3.10	Deflection scheme of the Thomson parabola	46
3.11	Inside view of the detection chamber from the detection plane	47
3.12	Energy-deflection function and theoretical ion tracks	49
3.13	Irradiated and processed piece of CR39; impact pits	50
3.14	CR39 covered with Aluminium foils	51
3.15	The unmounted Multi Channel Plate (MCP)	52
3.16	Parabolic tracks obtained from MCP	52
3.17	Comparison between the detection areas of the MCP and a CR39 plate	53
3.18	Conversion of parabolic tracks into a spectrum and binning procedure	54

3.19	Calibration of the relative MCP spectra against absolute CR39 counts	55
3.20	Proton spectra for Titanium foils of various thicknesses	57
3.21	Comparison between conventional targets and double layer targets	58
3.22	Peaked proton tracks recorded with the MCP	59
3.23	Monoenergetic proton spectra from dot irradiation	60
3.24	Difference between the dot spectrum and the exponential background	62
3.25	Peaked spectrum recorded on CR39	64
3.26	Screenshot of the 2D PIC simulation	65
3.27	Results from 2D PIC simulation	65
4.1	Scaling of the acceleration technique to the Petawatt regime	68
4.2	Stopping power of Aluminium	70
4.3	Penetration depth for Aluminium and biological tissue	71
4.4	Comparison of the stopping power of electrons, protons and α -particles in biological tissue . .	72
5.1	The next generation of dot targets	77

List of Tables

4.1	Proton ranges for different stopping materials	73
4.2	Bragg peak width for different degrees of monochromacy	74

6 Acknowledgements

I would like to express my foremost gratitude to Prof. Roland Sauerbrey, Dr. Heinrich Schwoerer and Prof. Ken Ledingham for the allocation and supervision of a very challenging, attractive and rewarding thesis topic, for their indispensable suggestions and for their critical review of the results and the thesis itself. It is not to be taken for granted that such unexperienced hands might be entrusted with such sophisticated work.

An vorderster Stelle möchte ich meinen Dank an Prof. Roland Sauerbrey, Dr. Heinrich Schwoerer und Prof. Ken Ledingham für die Vergabe und Betreuung eines sehr fordernden, reizvollen und bereichernden Diplomthemas richten - für ihre unverzichtbaren Anregungen und ihre kritische Begutachtung der Resultate und der Diplomarbeit. Es ist nicht selbstverständlich, ein so anspruchsvolles Thema in solch unerfahrene Hände zu legen.

Darüber hinaus möchte ich mich für die Unterstützung im letzten Jahr besonders bedanken bei:

- Oliver Jäckel; natürlich für die experimentelle Vorarbeit und sein Ingenieurstalent, vor allem aber dafür, dass er die Idealbesetzung meines Experimentierpartners war und dass mit und dank ihm eigentlich immer alles geklappt hat
- Kay-Uwe Amthor für seine fürsorgliche Einführung in die Thematik und seine Geduld, Geduld, Geduld...
- Dr. Heinrich Schwoerer für das freundschaftliche Arbeitsklima und die Fähigkeit, Abläufe im richtigen Moment zu beschleunigen oder abzubremsen
- Wolfgang Ziegler für die diffizile Anfertigung von Dot-Targets und die ingenieurstechnische Grundversorgung eines Diplomanden
- Burgard Beleites und Falk Ronneberger ebenfalls für viel Geduld und die treue Umsorgung des Lasers
- Prof. Timur Esirkepov für die Anregung und Unterfütterung der Experimente durch seine Simulationen
- Andreas Sachtleben für seine Hilfe beim Auswerten der Daten; Jens Poltz für die Verfeinerung der Targetherstellung

- Waltraud Gräf und Dr. Hans-Jörg Fuchs für das Beschichten der Targets
- Dr. Ben Liesfeld, Hans-Peter Schlenvoigt, Daniel Albach, Kerstin Haupt und Alexander Debus für die gute Zusammenarbeit
- den Werkstätten des Physikalischen Institutes für ihre meist kurzfristigen Einsätze
- dem Sekretariat des IOQ für die Bereitstellung von Kaffeenotreserven

Im Zuge des Studienabschlusses gilt mein Dank außerdem:

- mehr als allen anderen meiner Mutter, die mich zu jeder Zeit bedingungslos bei dem unterstützte, was ich gerade (lernen) wollte
- meiner Familie für ihre Fürsorge und das Gefühl, in Jena zu Hause zu sein
- Melissa Blackie für alles und auch ihr Englisch
- Anne Liebetrau, Oliver Jäckel, Thorsten Brüntjen und Gabor Matthäus für die andere Seite eines Physikstudiums
- meinen Musikern für die Kraft, die sie mir bedeuten - für die regelmäßige Entwirrung und ggf. Resensibilisierung meiner Gedanken; Prof. Georg Deutsch (Weimar) für die Geduld mit einem Ungeduldigen; Burga Schwoerer für gute Musik
- dem evangelischen Studienwerk Villigst für die jahrelange Förderung und viele Dinge jenseits des Tellerrandes
- Feli für ihr Verständnis und ihre Pflege in undankbaren Zeiten und für jede Minute, in der ich mich gefreut habe.

Bibliography

- [1] SCHWOERER, H. ; GIBBON, P. ; DUSTERER, S. ; BEHRENS, R. ; ZIENER, C. ; REICH, C. ; SAUERBREY, R.: MeV X rays and photoneutrons from femtosecond laser-produced plasmas. In: *Physical Review Letters* 86 (2001), Nr. 11, S. 2317–2320
- [2] UMSTADTER, D.: Review of physics and applications of relativistic plasmas driven by ultra-intense lasers. In: *Physics of Plasmas* 8 (2001), Nr. 5, S. 1774–1785
- [3] LEDINGHAM, K. W. D. ; MCKENNA, P. ; SINGHAL, R. P.: Applications for nuclear phenomena generated by ultra-intense lasers. In: *Science* 300 (2003), Nr. 5622, S. 1107–1111
- [4] ROTH, M. ; COWAN, T. E. ; KEY, M. H. ; HATCHETT, S. P. ; BROWN, C. ; FOUNTAIN, W. ; JOHNSON, J. ; PENNINGTON, D. M. ; SNAVELY, R. A. ; WILKS, S. C. ; YASUIKE, K. ; RUHL, H. ; PEGORARO, F. ; BULANOV, S. V. ; CAMPBELL, E. M. ; PERRY, M. D. ; POWELL, H.: Fast ignition by intense laser-accelerated proton beams. In: *Physical Review Letters* 86 (2001), Nr. 3, S. 436–439
- [5] KRUSHELNICK, K. ; CLARK, E. L. ; ALLOTT, R. ; BEG, F. N. ; DANSON, C. N. ; MACHACEK, A. ; MALKA, V. ; NAJMUDIN, Z. ; NEELY, D. ; NORREYS, P. A. ; SALVATI, M. R. ; SANTALA, M. I. K. ; TATARAKIS, M. ; WATTS, I. ; ZEPF, M. ; DANGOR, A. E.: Ultrahigh-intensity laser-produced plasmas as a compact heavy ion injection source. In: *IEEE Transactions on Plasma Science* 28 (2000), Nr. 4, S. 1184–1189
- [6] SPENCER, I. ; LEDINGHAM, K. W. D. ; SINGHAL, R. P. ; MCCANNY, T. ; MCKENNA, P. ; CLARK, E. L. ; KRUSHELNICK, K. ; ZEPF, M. ; BEG, F. N. ; TATARAKIS, M. ; DANGOR, A. E. ; NORREYS, P. A. ; CLARKE, R. J. ; ALLOTT, R. M. ; ROSS, I. N.: Laser generation of proton beams for the production of short-lived positron emitting radioisotopes. In: *Nuclear Instruments & Methods in Physics Research Section B - Beam Interactions with Materials and Atoms* 183 (2001), Nr. 3-4, S. 449–458

- [7] BULANOV, S. V. ; KHOROSHKOV, V. S.: Feasibility of using laser ion accelerators in proton therapy. In: *Plasma Physics Reports* 28 (2002), Nr. 5, S. 453–456
- [8] FRITZLER, S. ; MALKA, V. ; GRILLON, G. ; ROUSSEAU, J. P. ; BURG, F. ; LEFEBVRE, E. ; D'HUMIERES, E. ; MCKENNA, P. ; LEDINGHAM, K. W. D.: Proton beams generated with high-intensity lasers: Applications to medical isotope production. In: *Applied Physics Letters* 83 (2003), Nr. 15, S. 3039–3041
- [9] SCHWOERER, H. ; PFOTENHAUER, S. ; JACKEL, O. ; AMTHOR, K. U. ; LIESFELD, B. ; ZIEGLER, W. ; SAUERBREY, R. ; LEDINGHAM, K. W. D. ; ESIRKEPOV, T.: Laser-plasma acceleration of quasi-monoenergetic protons from microstructured targets. In: *Nature* 439 (2006), Nr. 7075, S. 445–448
- [10] FAURE, J. ; GLINEC, Y. ; PUKHOV, A. ; KISELEV, S. ; GORDIENKO, S. ; LEFEBVRE, E. ; ROUSSEAU, J. P. ; BURG, F. ; MALKA, V.: A laser-plasma accelerator producing monoenergetic electron beams. In: *Nature* 431 (2004), Nr. 7008, S. 541–544
- [11] GEDDES, C. G. R. ; TOTH, C. ; TILBORG, J. van ; ESAREY, E. ; SCHROEDER, C. B. ; BRUHWILER, D. ; NIETER, C. ; CARY, J. ; LEEMANS, W. P.: High-quality electron beams from a laser wakefield accelerator using plasma-channel guiding. In: *Nature* 431 (2004), Nr. 7008, S. 538–541
- [12] MANGLES, S. P. D. ; MURPHY, C. D. ; NAJMUDIN, Z. ; THOMAS, A. G. R. ; COLLIER, J. L. ; DANGOR, A. E. ; DIVALL, E. J. ; FOSTER, P. S. ; GALLACHER, J. G. ; HOOKER, C. J. ; JAROSZYNSKI, D. A. ; LANGLEY, A. J. ; MORI, W. B. ; NORREYS, P. A. ; TSUNG, F. S. ; VISKUP, R. ; WALTON, B. R. ; KRUSHELNICK, K.: Monoenergetic beams of relativistic electrons from intense laser-plasma interactions. In: *Nature* 431 (2004), Nr. 7008, S. 535–538
- [13] HEGELICH, B. M. ; ALBRIGHT, B. J. ; COBBLE, J. ; FLIPPO, K. ; LETZRING, S. ; PAFFETT, M. ; RUHL, H. ; SCHREIBER, J. ; SCHULZE, R. K. ; FERNANDEZ, J. C.: Laser acceleration of quasi-monoenergetic MeV ion beams. In: *NATURE* 439 (2006), Nr. 7075, S. 441–444
- [14] SCHWOERER, Heinrich: *Eine Einführung in die relativistische Plasmaphysik (Lecture Notes)*. Friedrich-Schiller-University Jena, 2002
- [15] ASHCROFT, Neil W. ; MERMIN, N. D. ; CRANE, D. G. (Hrsg.): *Solid state physics*. Saunders College Publishing, Philadelphia, 1976
- [16] KRUEER, William L.: *The physics of laser plasma interactions*. Addison-Wesley, 1988

- [17] BULANOV, S. V. ; KIRSANOV, V. I. ; SAKHAROV, A. S.: Excitation of Ultrarelativistic Plasma-Waves by Pulse of Electromagnetic Radiation. In: *JETP Letters* 50 (1989), Nr. 4, S. 198–201
- [18] SPRANGLE, P. ; ESARLY, E. ; TING, A.: Nonlinear-Interaction of Intense Laser-Pulses in Plasmas. In: *Physical Review A* 41 (1990), Nr. 8, S. 4463–4467
- [19] MILONNI, Peter W. ; EBERLY, Joseph H.: *Lasers*. Wiley, New York, 1988
- [20] FLIESSBACH, Thorsten: *Elektrodynamik*. Spektrum akademischer Verlag, Heidelberg, 1997
- [21] ALLEN, Matthew M.: *Laser ion acceleration from the interaction of ultra-intense laser pulses with thin foils*, Lawrence Livermore National Laboratory, University of California, Diss., 2004
- [22] BERNHARD, Jens: *Aufbau eines Experimentes zur Überlagerung zweier gegenläufiger intensiver Laserpulse*, Department of Physics and Astronomy, Friedrich-Schiller-University Jena, Diplomarbeit, 2005
- [23] AMIRANOFF, F.: Fast electron production in ultra-short high-intensity laser-plasma interaction and its consequences. In: *Measurement Science and Technology* 12 (2001), Nr. 11, S. 1795–1800
- [24] KALUZA, Malte C.: *Characterisation of Laser-Accelerated Proton Beams*, MPI für Quantenoptik, Garching, Diss., 2004
- [25] HARTEMANN, F. V. ; FOCHS, S. N. ; LESAGE, G. P. ; LUHMANN, N.C. ; WOODSWORTH, J. G. ; PERRY, M. D. ; CHEN, Y. J. ; KERMAN, A. K.: Non-linear Ponderomotive Scattering of Relativistic Electrons by an Intense Laser Field at Focus. In: *Physical Review E* 51 (1995), Nr. 5, S. 4833–4843
- [26] YU, W. ; BYCHENKOV, V. ; SENTOKU, Y. ; YU, M. Y. ; SHENG, Z. M. ; MIMA, K.: Electron acceleration by a short relativistic laser pulse at the front of solid targets. In: *Physical Review Letters* 85 (2000), Nr. 3, S. 570–573
- [27] QUESNEL, B. ; MORA, P.: Theory and simulation of the interaction of ultraintense laser pulses with electrons in vacuum. In: *Physical Review E* 58 (1998), Nr. 3, S. 3719–3732
- [28] KALUZA, M. ; SCHREIBER, J. ; SANTALA, M. I. K. ; TSAKIRIS, G. D. ; EIDMANN, K. ; VEHN, J. Meyer-ter ; WITTE, K. J.: Influence of the laser prepulse on proton acceleration in thin-foil experiments. In: *Physical Review Letters* 93 (2004), Nr. 4, S. 045003

- [29] BRUNEL, F.: Not-so-resonant, Resonant Absorption. In: *Physical Review Letters* 59 (1987), S. 52
- [30] TAJIMA, T. ; DAWSON, J. M.: Laser Electron-Accelerator. In: *Physical Review Letters* 43 (1979), Nr. 4, S. 267–270
- [31] MALKA, V. ; FRITZLER, S. ; LEFEBVRE, E. ; ALEONARD, M. M. ; BURGY, F. ; CHAMBARET, J. P. ; CHEMIN, J. F. ; KRUSHELNICK, K. ; MALKA, G. ; MANGLES, S. P. D. ; NAJMUDIN, Z. ; PITTMAN, M. ; ROUSSEAU, J. P. ; SCHEURER, J. N. ; WALTON, B. ; DANGOR, A. E.: Electron acceleration by a wake field forced by an intense ultrashort laser pulse. In: *Science* 298 (2002), Nr. 5598, S. 1596–1600
- [32] LIESFELD, Ben: *A Photon Collider at Relativistic Intensity*, Friedrich-Schiller-Universität Jena, Diss., 2005
- [33] SCHLENVOIGT, Hans-Peter: *Thomson-Rückstreuung von Laser-erzeugten relativistischen Elektronen - Ein Mittel zur Analyse der Prozesse in Laser-Plasma-Beschleunigern*, Department of Physics and Astronomy, Friedrich-Schiller-University Jena, Diplomarbeit, 2005
- [34] CLARK, E. L. ; KRUSHELNICK, K. ; DAVIES, J. R. ; ZEPF, M. ; TATARAKIS, M. ; BEG, F. N. ; MACHACEK, A. ; NORREYS, P. A. ; SANTALA, M. I. K. ; WATTS, I. ; DANGOR, A. E.: Measurements of energetic proton transport through magnetized plasma from intense laser interactions with solids. In: *Physical Review Letters* 84 (2000), Nr. 4, S. 670–673
- [35] SENTOKU, Y. ; COWAN, T. E. ; KEMP, A. ; RUHL, H.: High energy proton acceleration in interaction of short laser pulse with dense plasma target. In: *Physics of Plasmas* 10 (2003), Nr. 5, S. 2009–2015
- [36] SNAVELY, R. A. ; KEY, M. H. ; HATCHETT, S. P. ; COWAN, T. E. ; ROTH, M. ; PHILLIPS, T. W. ; STOYER, M. A. ; HENRY, E. A. ; SANGSTER, T. C. ; SINGH, M. S. ; WILKS, S. C. ; MACKINNON, A. ; OFFENBERGER, A. ; PENNINGTON, D. M. ; YASUIKE, K. ; LANGDON, A. B. ; LASINSKI, B. F. ; JOHNSON, J. ; PERRY, M. D. ; CAMPBELL, E. M.: Intense high-energy proton beams from petawatt-laser irradiation of solids. In: *Physical Review Letters* 85 (2000), Nr. 14, S. 2945–2948
- [37] HATCHETT, S. P. ; BROWN, C. G. ; COWAN, T. E. ; HENRY, E. A. ; JOHNSON, J. S. ; KEY, M. H. ; KOCH, J. A. ; LANGDON, A. B. ; LASINSKI, B. F. ; LEE, R. W. ; MACKINNON, A. J. ; PENNINGTON, D. M. ; PERRY, M. D. ; PHILLIPS, T. W. ; ROTH, M. ; SANGSTER, T. C. ; SINGH, M. S. ; SNAVELY, R. A. ; STOYER, M. A. ; WILKS, S. C. ; YASUIKE, K.: Electron, photon, and ion beams from the relativistic

- interaction of Petawatt laser pulses with solid targets. In: *Physics of Plasmas* 7 (2000), Nr. 5, S. 2076–2082
- [38] WILKS, S. C. ; LANGDON, A. B. ; COWAN, T. E. ; ROTH, M. ; SINGH, M. ; HATCHETT, S. ; KEY, M. H. ; PENNINGTON, D. ; MACKINNON, A. ; SNAVELY, R. A.: Energetic proton generation in ultra-intense laser-solid interactions. In: *Physics of Plasmas* 8 (2001), Nr. 2, S. 542–549
- [39] ALLEN, M. ; PATEL, P. K. ; MACKINNON, A. ; PRICE, D. ; WILKS, S. ; MORSE, E.: Direct experimental evidence of back-surface ion acceleration from laser-irradiated gold foils. In: *Physical Review Letters* 93 (2004), Nr. 26, S. 265004
- [40] FUCHS, J. ; SENTOKU, Y. ; KARSCH, S. ; COBBLE, J. ; AUDEBERT, P. ; KEMP, A. ; NIKROO, A. ; ANTICI, P. ; BRAMBRINK, E. ; BLAZEVIC, A. ; CAMPBELL, E. M. ; FERNANDEZ, J. C. ; GAUTHIER, J. C. ; GEISSEL, M. ; HEGELICH, M. ; PEPIN, H. ; POPESCU, H. ; RENARD-LEGALLOUDEC, N. ; ROTH, M. ; SCHREIBER, J. ; STEPHENS, R. ; COWAN, T. E.: Comparison of laser ion acceleration from the front and rear surfaces of thin foils. In: *Physical Review Letters* 94 (2005), Nr. 4, S. 045004
- [41] GIBBON, Paul: Resistively enhanced proton acceleration in high intensity laser-foil interactions. In: *private copy* (2004)
- [42] D'HUMIERES, E. ; LEFEBVRE, E. ; GREMILLET, L. ; MALKA, V.: Proton acceleration mechanisms in high-intensity laser interaction with thin foils. In: *Physics of Plasmas* 12 (2005), Nr. 6, S. 062704
- [43] CLARK, E. L. ; KRUSHELNICK, K. ; ZEPF, M. ; BEG, F. N. ; TATARAKIS, M. ; MACHACEK, A. ; SANTALA, M. I. K. ; WATTS, I. ; NORREYS, P. A. ; DANGOR, A. E.: Energetic heavy-ion and proton generation from ultraintense laser-plasma interactions with solids. In: *Physical Review Letters* 85 (2000), Nr. 8, S. 1654–1657
- [44] DENAVIT, J.: Absorption of High-Intensity Subpicosecond Lasers on Solid Density Targets. In: *Physical Review Letters* 69 (1992), Nr. 21, S. 3052–3055
- [45] WILKS, S. C. ; KRUER, W. L. ; TABAK, M. ; LANGDON, A. B.: ABSORPTION OF ULTRA-INTENSE LASER-PULSES. In: *Physical Review Letters* 69 (1992), Nr. 9, S. 1383–1386
- [46] WILKS, S. C.: SIMULATIONS OF ULTRAINTENSE LASER-PLASMA INTERACTIONS. In: *Physics of Fluids B - Plasma Physics* 5 (1993), Nr. 7, S. 2603–2608

- [47] SILVA, L. O. ; MARTI, M. ; DAVIES, J. R. ; FONSECA, R. A. ; REN, C. ; TSUNG, F. S. ; MORI, W. B.: Proton shock acceleration in laser-plasma interactions. In: *Physical Review Letters* 92 (2004), Nr. 1, S. 015002
- [48] FORSLUND, D. W. ; SHONK, C. R.: Formation and Structure of Electrostatic Collisionless Shocks. In: *Physical Review Letters* 25 (1970), S. 1699
- [49] GITOMER, S. J. ; JONES, R. D. ; BEGAY, F. ; EHLER, A. W. ; KEPHART, J. F. ; KRISTAL, R.: Fast ions and hot electrons in the laser-plasma interaction. In: *Physics of Fluids* 29 (1986), Nr. 8, S. 2679–2688
- [50] EWALD, F.: *Harte Röntgenstrahlung aus relativistischen Laserplasmen und laserinduzierte Kernreaktionen*, Friedrich-Schiller-Universität Jena, Diss., 2004
- [51] BULANOV, S. V. ; ESIRKEPOV, T. Z. ; KAMENETS, F. F. ; KATO, Y. ; KUZNETSOV, A. V. ; NISHIHARA, K. ; PEGORARO, F. ; TAJIMA, T. ; KHOROSHKOV, V. S.: Generation of high-quality charged particle beams during the acceleration of ions by high-power laser radiation. In: *Plasma Physics Reports* 28 (2002), Nr. 12, S. 975–991
- [52] MCKENNA, P. ; LEDINGHAM, K. W. D. ; SPENCER, I. ; MCCANY, T. ; SINGHAL, R. P. ; ZIENER, C. ; FOSTER, P. S. ; DIVALL, E. J. ; HOOKER, C. J. ; NEELY, D. ; LANGLEY, A. J. ; CLARKE, R. J. ; NORREYS, P. A. ; KRUSHELNICK, K. ; CLARK, E. L.: Characterization of multiterawatt laser-solid interactions for proton acceleration. In: *Review of Scientific Instruments* 73 (2002), Nr. 12, S. 4176–4184
- [53] ALLEN, M. ; SENTOKU, Y. ; AUDEBERT, P. ; BLAZEVIC, A. ; COWAN, T. ; FUCHS, J. ; GAUTHIER, J. C. ; GEISSEL, M. ; HEGELICH, M. ; KARSCH, S. ; MORSE, E. ; PATEL, P. K. ; ROTH, M.: Proton spectra from ultraintense laser-plasma interaction with thin foils: Experiments, theory, and simulation. In: *Physics of Plasmas* 10 (2003), Nr. 8, S. 3283–3289
- [54] ROTH, M. ; BLAZEVIC, A. ; GEISSEL, M. ; SCHLEGEL, T. ; COWAN, T. E. ; ALLEN, M. ; GAUTHIER, J. C. ; AUDEBERT, P. ; FUCHS, J. ; VEHN, J. Meyer-ter ; HEGELICH, M. ; KARSCH, S. ; PUKHOV, A.: Energetic ions generated by laser pulses: A detailed study on target properties. In: *Physical Review Special Topics - Accelerators and Beams* 5 (2002), Nr. 6, S. 061301
- [55] BORGHESI, M. ; MACKINNON, A. J. ; CAMPBELL, D. H. ; HICKS, D. G. ; KAR, S. ; PATEL, P. K. ; PRICE, D. ; ROMAGNANI, L. ; SCHIAVI, A. ; WILLI, O.: Multi-MeV proton source investigations in ultraintense laser-foil interactions. In: *Physical Review Letters* 92 (2004), Nr. 5, S. 055003

- [56] KISHIMURA, H. ; MORISHITA, H. ; OKANO, Y. H. ; OKANO, Y. ; HIRONAKA, Y. ; KONDO, K. ; NAKAMURA, K. G. ; OISHI, Y. ; NEMOTO, K.: Enhanced generation of fast protons from a polymer-coated metal foil by a femtosecond intense laser field. In: *Applied Physics Letters* 85 (2004), Nr. 14, S. 2736–2738
- [57] PUKHOV, A.: Three-dimensional simulations of ion acceleration from a foil irradiated by a short-pulse laser. In: *Physical Review Letters* 86 (2001), Nr. 16, S. 3562–3565
- [58] ESIRKEPOV, T. Z. ; BULANOV, S. V. ; NISHIHARA, K. ; TAJIMA, T. ; PEGORARO, F. ; KHOROSHKOV, V. S. ; MIMA, K. ; DAIDO, H. ; KATO, Y. ; KITAGAWA, Y. ; NAGAI, K. ; SAKABE, S.: Proposed double-layer target for the generation of high-quality laser-accelerated ion beams. In: *Physical Review Letters* 89 (2002), Nr. 17, S. 175003
- [59] MATSUKADO, K. ; ESIRKEPOV, T. ; KINOSHITA, K. ; DAIDO, H. ; UTSUMI, T. ; LI, Z. ; FUKUMI, A. ; HAYASHI, Y. ; ORIMO, S. ; NISHIUCHI, M. ; BULANOV, S. V. ; TAJIMA, T. ; NODA, A. ; IWASHITA, Y. ; SHIRAI, T. ; TAKEUCHI, T. ; NAKAMURA, S. ; YAMAZAKI, A. ; IKEGAMI, M. ; MIHARA, T. ; MORITA, A. ; UESAKA, M. ; YOSHII, K. ; WATANABE, T. ; HOSOKAI, T. ; ZHIDKOV, A. ; OGATA, A. ; WADA, Y. ; KUBOTA, T.: Energetic protons from a few-micron metallic foil evaporated by an intense laser pulse. In: *Physical Review Letters* 91 (2003), Nr. 21, S. 215001
- [60] COWAN, T. E. ; FUCHS, J. ; RUHL, H. ; KEMP, A. ; AUDEBERT, P. ; ROTH, M. ; STEPHENS, R. ; BARTON, I. ; BLAZEVIC, A. ; BRAMBRINK, E. ; COBBLE, J. ; FERNANDEZ, J. ; GAUTHIER, J. C. ; GEISSEL, M. ; HEGELICH, M. ; KAAE, J. ; KARSCH, S. ; LE SAGE, G. P. ; LETZRING, S. ; MANCLOSSI, M. ; MEYRONEINC, S. ; NEWKIRK, A. ; PEPIN, H. ; RENARD-LEGALLOUDEC, N.: Ultralow emittance, multi-MeV proton beams from a laser virtual-cathode plasma accelerator. In: *Physical Review Letters* 92 (2004), Nr. 20, S. 204801
- [61] KEMP, A. J. ; PFUND, R. E. W. ; VEHN, J. Meyer-ter: Modeling ultrafast laser-driven ionization dynamics with Monte Carlo collisional particle-in-cell simulations. In: *Physics of Plasmas* 11 (2004), Nr. 12, S. 5648–5657
- [62] JÄCKEL, Oliver: *Vermessung von Ionenspektren aus relativistischen laserproduzierten Plasmen*, Department of Physics and Astronomy, Friedrich-Schiller-University Jena, Diplomarbeit, 2005
- [63] PATEL, P. K. ; MACKINNON, A. J. ; KEY, M. H. ; COWAN, T. E. ; FOORD, M. E. ; ALLEN, M. ; PRICE, D. F. ; RUHL, H. ; SPRINGER, P. T. ; STEPHENS, R.: Isochoric

- heating of solid-density matter with an ultrafast proton beam. In: *Physical Review Letters* 91 (2003), Nr. 12, S. 125004
- [64] SCHREIBER, J. ; KALUZA, M. ; GRUNER, F. ; SCHRAMM, U. ; HEGELICH, B. M. ; COBBLE, J. ; GEISSLER, M. ; BRAMBRINK, E. ; FUCHS, J. ; AUDEBERT, P. ; HABS, D. ; WITTE, K.: Source-size measurements and charge distributions of ions accelerated from thin foils irradiated by high-intensity laser pulses. In: *Applied Physics B - Lasers and Optics* 79 (2004), Nr. 8, S. 1041–1045
- [65] HEGELICH, M. ; KARSCH, S. ; PRETZLER, G. ; HABS, D. ; WITTE, K. ; GUENTHER, W. ; ALLEN, M. ; BLAZEVIC, A. ; FUCHS, J. ; GAUTHIER, J. C. ; GEISEL, M. ; AUDEBERT, P. ; COWAN, T. ; ROTH, M.: MeV ion jets from short-pulse-laser interaction with thin foils. In: *Physical Review Letters* 89 (2002), Nr. 8, S. 085002
- [66] MCKENNA, P. ; LEDINGHAM, K. W. D. ; YANG, J. M. ; ROBSON, L. ; MCCANNY, T. ; SHIMIZU, S. ; CLARKE, R. J. ; NEELY, D. ; SPOHR, K. ; CHAPMAN, R. ; SINGHAL, R. P. ; KRUSHELNICK, K. ; WEI, M. S. ; NORREYS, P. A.: Characterization of proton and heavier ion acceleration in ultrahigh-intensity laser interactions with heated target foils. In: *Physical Review E* 70 (2004), Nr. 3, S. 036405
- [67] MACKINNON, A. J. ; BORGHESI, M. ; HATCHETT, S. ; KEY, M. H. ; PATEL, P. K. ; CAMPBELL, H. ; SCHIAVI, A. ; SNAVELY, R. ; WILKS, S. C. ; WILLI, O.: Effect of plasma scale length on multi-MeV proton production by intense laser pulses. In: *Physical Review Letters* 86 (2001), Nr. 9, S. 1769–1772
- [68] BADZIAK, J. ; WORYNA, E. ; PARYS, R. ; PLATONOV, K. Y. ; JABLONSKI, S. ; RYE, L. ; VANKOV, A. B. ; WOLOWSKI, J.: Fast proton generation from ultrashort laser pulse interaction with double-layer foil targets. In: *Physical Review Letters* 8721 (2001), Nr. 21, S. 215001
- [69] MAKSIMCHUK, A. ; GU, S. ; FLIPPO, K. ; UMSTADTER, D. ; BYCHENKOV, V. Y.: Forward ion acceleration in thin films driven by a high-intensity laser. In: *Physical Review Letters* 84 (2000), Nr. 18, S. 4108–4111
- [70] ALBACH, Daniel: *Aufbau einer Apparatur zur Vorpulsunterdrückung eines 15 Terawatt- Titan:Saphir-Lasers*, Department of Physics and Astronomy, Friedrich-Schiller-University Jena, Diplomarbeit, 2005
- [71] LANDAU, L. D. ; LIFSCHITZ, E. M. ; HEBER, Gerhard (Hrsg.): *Elektrodynamik der Kontinua*. Akademie-Verlag Berlin, 1971
- [72] STRICKLAND, D. ; MOUROU, G.: Compression of Amplified Chirped Optical Pulses. In: *Optics Communications* 56 (1985), Nr. 3, S. 219–221

- [73] ARNOLD, N. ; BITYURIN, N.: Model for laser-induced thermal degradation and ablation of polymers. In: *Applied Physics A - Materials Science & Processing* 68 (1999), Nr. 6, S. 615–625
- [74] ARNOLD, N. ; SCHREMS, G. ; BAUERLE, D.: Ablative thresholds in laser cleaning of substrates from particulates. In: *Applied Physics A - Materials Science & Processing* 79 (2004), Nr. 4-6, S. 729–734
- [75] ZANGWILL, Andrew: *Physics at Surfaces*. Cambridge University Press, 1988
- [76] CASSOU, R. M. ; BENTON, E. V.: Properties and Applications of CR-39 Polymeric Nuclear Track Detector. In: *Nuclear Track Detection 2* (1978), S. 173–170
- [77] HEIN, J. ; PODLESKA, S. ; SIEBOLD, M. ; HELLWING, M. ; BODEFELD, R. ; SAUERBREY, R. ; EHRT, D. ; WINTZER, W.: Diode-pumped chirped pulse amplification to the joule level. In: *Applied Physics B - Lasers and Optics* 79 (2004), Nr. 4, S. 419–422
- [78] ESIRKEPOV, T. Z. ; YAMAGIWA, M. ; TAJIMA, T.: Laser Ion Acceleration Scaling Laws seen in Multi-Parametric PIC Simulations. In: *Physical Review Letters* 96 (2006), S. 105001
- [79] BETHGE, Klaus ; WALTER, Gertrud ; WIEDEMANN, Bernhard: *Kernphysik*. Springer, 2001
- [80] GREEN, A. E. S. ; SCHIFF, L. I. (Hrsg.): *Nuclear Physics*. McGraw-Hill Books Company, 1955 (International Series in Pure and Applied Physics)
- [81] RIEZLER, W. ; WALCHER, W.: *Kerntechnik*. B. G. Teubner Verlagsgesellschaft, 1958
- [82] STANDARDS, National I. ; TECHNOLOGY: *Stopping-Power and Range Tables for Protons*. <http://physics.nist.gov/PhysRefData/Star/Text/PSTAR.html>
- [83] RNSA: *Radiation Society of North America - RadiologyInfo*. <http://www.radiologyinfo.org>
- [84] SZILAGYI, Miklos: *Electron and Ion Optics*. Plenum Press, 1988
- [85] TONCIAN, T. ; BORGHESI, M. ; FUCHS, J. ; D'HUMIÈRES, E. ; ANTICI, P. ; AUDEBERT, P. ; BRAMBRINK, E. ; CECCHETTI, C. A. ; PIPAHL, A. ; ROMAGNANI, L. ; WILLI, O.: Ultrafast Laser-Driven Microlens to Focus and Energy-Select Mega-Electron Volt Protons. In: *ScienceExpress* 10.1126 (2006), S. science.1124412

- [86] WILSON, Vasthi Christensen M. ; MCDONOUGH, James P. ; TOCHNER, Zelig M.:
Proton Beam Irradiation in Pediatric Oncology: An Overview. In: *Journal of
Pediatric Hematology/Oncology* 27(8) (2005), S. 444-448

Erklärung

Hiermit erkläre ich, dass ich die vorliegende Arbeit selbstständig verfasst und keine anderen als die angegebenen Quellen und Hilfsmittel genutzt habe.

Seitens des Verfassers bestehen keine Einwände, die vorliegende Diplomarbeit für die öffentliche Nutzung in der Thüringer Universitäts- und Landesbibliothek zur Verfügung zu stellen.

Jena, den 28.2. 2006